UNIVERSITEIT GENT

FACULTEIT WETENSCHAPPEN

# REGGE-PLUS-RESONANCE APPROACH TO KAON PRODUCTION FROM THE PROTON

Tamara Corthals

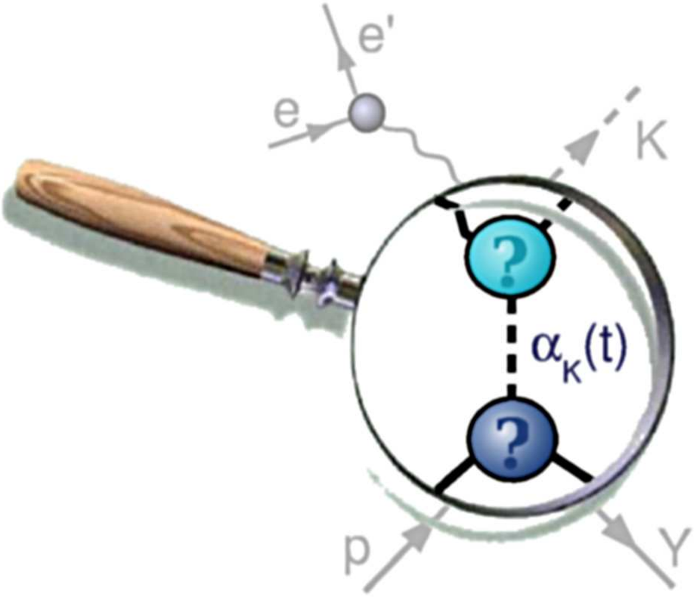

Promotor: Prof. dr. JAN RYCKEBUSCH

Proefschrift ingediend tot het behalen van de academische graad van
Doctor in de Wetenschappen: Natuurkunde

Universiteit Gent
Faculteit Wetenschappen
Vakgroep Subatomaire en Stralingsfysica
Academiejaar 2006-2007

They are ill discoverers that think there is no land
when they can see nothing but sea.

*Francis Bacon,*
*philosopher and statesman*

There ain’t no rules around here! We’re trying to accomplish something!

*Thomas Edison, inventor*

# Preface

Misschien vindt u, beste lezer, het citaat op de vorige pagina (niet dat van Edison, het andere) enigszins verrassend, of zelfs ongepast lyrisch in een context als deze. Dat zou ik u niet kwalijk nemen; het gaat hier tenslotte om een fysica-thesis, en fysica behoort logisch te zijn, beredeneerd, zakelijk - toch? Ik geef dan ook toe dat een vergelijking trekken tussen de wetenschap en de weidse oceaan, met onderzoekers in de rol van dappere avonturiers, een ietwat geromantiseerd beeld is van mijn bezigheden de voorbije vier jaar. Al zou ik de vergelijking ook niet helemaal van tafel willen vegen want, in tegenstelling tot wat u misschien denkt, is de fysica geen netjes aangelegd vijvertje waarin je maar te vissen hebt naar theorieën. Integendeel, het is een woelig water waarin je makkelijk verdrinkt, en af en toe zijn er kapers op de kust. Het was dan ook goed dat ik al die “gevaren” niet alleen heb moeten trotseren.

Jan, u hebt me indertijd uit de licentiaatsvijver opgevist, en me de kans gegeven mijn tanden in de wereld van de “vreemde” deeltjes te zetten; bedankt voor het vertrouwen en -hoe kan het ook anders- de interactie. Thank you, Dave, for your help and useful insights, and for the nice collaboration. Stijn, blij dat ik je code mocht erven, het is een “schoontje”. Tim, mocht ik mijn dankbaarheid uitdrukken in Twixen, kon je meteen gaan Weightwatchen; bedankt voor je antwoorden op al mijn vragen en je (lastige!) vragen bij al mijn antwoorden. Dankjewel, Annelies, voor het delen van al die kleine en grote frustraties én overwinningen. Bart en Pieter, de bureauconversaties met jullie waren een inspiratie in moeilijke tijden - het zal wennen worden zonder. Klaas, je hebt mijn computer meermaals van de dood gered; merci dat je deur (bijna) altijd openstond. Dank ook aan alle andere collega’s en ex-collega’s, die “het leven zoals het is: INW” zo uniek en plezant maakten: Stijn, Veerle, Kris, Wim, Simon, Arne, Natalie, Peter, Pascal, Cris, ... de lijst gaat door. Ook een dikke merci aan alle vrienden buiten de werkomgeving, die me steeds met beide voeten op de grond hielden.

Een ontdekkingsreiziger - ook één die in de wetenschap werkt - heeft een haven nodig, en die heb ik steeds gehad. Mama en papa, merci voor de steun, en omdat ik het allemaal op mijn manier heb mogen doen. Ook de kritische blik (die soms nodig was) heeft geholpen, al had ik dat op het ogenblik zelf niet altijd even goed door.

Aan mijn jongen Christophe: in die vier jaar onderzoek was jij veruit mijn grootste ontdekking. Dank je om me te vinden en te houden, en al mijn orkanen te doorstaan.

# Contents

CHAPTER

# 1

# Introduction

A strong catalyst of scientific progress has always been the desire to see beyond the confines of our everyday experience of time and space. Paradoxically, this fascination with the vastness of the universe is paralleled by a mounting interest in processes at ever smaller distance scales. In the cores of stars and the depths of interstellar space, phenomena are observed which, on earth, only occur under artificial circumstances such as those created in particle accelerators. As a rule, the larger the available energies in a reaction, the smaller the resolution at which the participating particles can be probed. A firm grasp of the fundamental building blocks is therefore essential to understand the multitude of exotic processes occurring in our universe.

## The standard model and QCD

A landmark in our understanding of the microscopic world has been the development of the "standard model" [1], as summarized in Fig. 1.1. This model classifies all elementary particles into two categories of fermions: leptons, with the electron and electron-neutrino as best-known examples, and quarks, which form the constituents of hadrons such as the proton and neutron. It turns out that the seemingly infinite variety of processes occurring in nature can be understood on the basis of four fundamental forces. The standard model unites three of these: the weak, electromagnetic and strong interactions, which are understood to be mediated by the exchange of bosons.

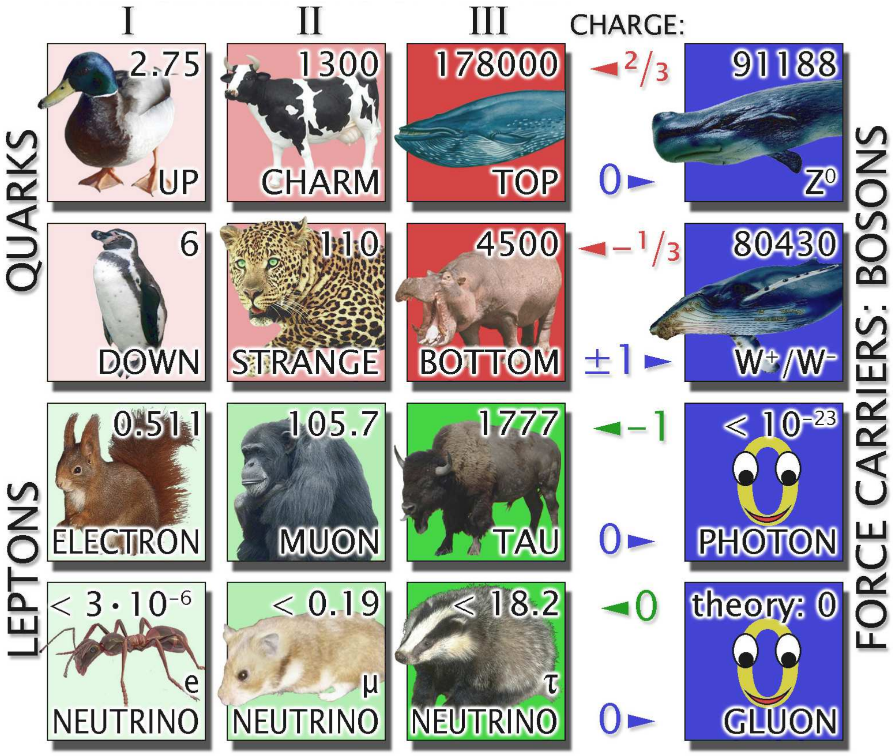

**Figure 1.1** *Schematic overview of the fundamental particles according to the standard model: six* quarks *(up, down, charm, strange, top, bottom - of which only* u, d *and to a minor degree* s *are found in non-exotic matter); six* leptons *(electron, muon and tau, plus the corresponding neutrinos); and three types of force-carrying* bosons *(photons, gluons, and the Z/W bosons, responsible for the electromagnetic, strong and weak interactions, respectively). Particle masses are given in MeV.*

The fourth and weakest force, gravity, is the subject of heated debates, centered around the validity of string theory as a possible candidate for a unified theory of matter.

The three standard-model forces are well understood. For each, a field-theoretical framework is available which describes how the force-carrying bosons couple to the elementary fermions. Knowledge of the behavior of the *fundamental* constituents of matter does not guarantee an understanding of larger-scale processes, however, just like knowledge of the laws of mechanics does not enable one to predict the weather. In this respect the strong interaction, described by the theory of quantum chromodynamics (QCD), is by far the most challenging. This is due to a unique characteristic of the strong coupling constant $\alpha_s$, which measures the strength of the inter-quark force. In contrast to the weak and electromagnetic couplings, $\alpha_s$ does not decrease but *increases* when the interacting particles move further apart [2–5].

An interesting side effect of this behavior is the phenomenon called "confinement". This entails that quarks cannot be observed as free objects, but only in bound states of several quarks and/or antiquarks. On the other hand, quarks contained in a very limited space behave as quasi-free particles, a property known as “asymptotic freedom”. Unfortunately, the region in which quarks may be considered asymptotically free is not relevant to the energy scales typical for “common” matter. By QCD standards, distances of the order of the nucleon size imply values of $\alpha_s$ that are too large for the usual perturbative approaches. While a numerical approach to QCD in the medium-energy region, called “lattice QCD” [6], does exist, at this point only static hadron properties have been obtained with any level of confidence. As a consequence, the interpretation of dynamical hadronic processes still hinges in significant degree on models containing some phenomenological ingredients.

## Probing the nucleon spectrum

The main objective of the study of hadronic physics is to gain insight into the transition between quark-gluon and hadronic degrees of freedom. Over the years, considerable effort has been invested into improving the existing picture of the nucleon spectrum [7]. Like the excited states of atoms have taught about the governing interactions, knowledge of the nucleon excitations or “resonances” (abbreviated as $N^*$s) is expected to provide essential information concerning the behavior of quarks at hadronic scales.

One of the central question marks in the field of $N^*$ physics is the so-called “missing-resonance problem”. It turns out that many of the resonances predicted by constituent-quark models (CQMs) [8–12] are yet to receive experimental confirmation. By definition, a CQM describes the nucleon as a bound state of three effective or *constituent* quarks. These can be visualized as “naked” quarks enveloped by an ever-changing sea of gluons and quark-antiquark pairs. Two possible explanations for the missing-resonance issue have been put forward, the first and most drastic one being that constituent quarks may not represent the proper degrees of freedom. Quark-diquark models, which contain fewer degrees of freedom, may be more appropriate [13, 14]. Alternatively, Koniuk and Isgur [15] indicated the possibility that these resonances do exist, but manifest themselves in different reaction channels than those traditionally measured.

A great deal of experimental and theoretical interest has been directed to exploring the latter hypothesis. Most of the available information concerning the $N^*$ spectrum was gathered through experiments involving pion-nucleon final states. As several of the “missing” resonances are predicted to couple weakly to the $\pi N$ channel, it should come as no surprise that they have so far remained unobserved. There are, however, indications that some missing states have a larger probability of decaying into alternative reaction channels, like $\omega N$, $\eta N$, $\pi\pi N$, $K\Lambda$ and $K\Sigma$ [16,17].

Although the largest count rates are obtained in hadronic processes, use of an electromagnetic (EM) probe has a distinct advantage. Indeed, all EM ingredients in the reaction amplitude can be straightforwardly expressed in the context of quantum electrodynamics or QED, the well-established theory of EM interactions. The scattering of photons and electrons from nucleons and nuclei constitutes the backbone of the physics program at facilities such as JLab, MIT-Bates, MAMI, ELSA, SPring-8, and GRAAL.

## Strangeness production and effective fields

Electromagnetic reactions with either "open" or "closed" strangeness in the final state are particularly interesting because of the involvement of a strange quark-antiquark pair from the sea. In this work, we focus on the open-strangeness case, particularly the production of a ground-state kaon and hyperon (i.e. a baryon with nonzero strangeness, commonly abbreviated as Y) from a free nucleon.

Theoretical approaches to EM strangeness production generally fall into two categories. In parton-based models, the quark-gluon structure of the interacting hadrons is explicitly tied in with the reaction dynamics. A successful example of such a strategy is the work of Li and Saghai *et al.*, in which the interaction vertices are constructed directly from a chiral constituent-quark model [18–22]. Alternatively, hadrodynamic approaches consider the interacting hadrons themselves as the basic degrees of freedom of the effective field theory. Thereby, the inter-particle interactions are modeled in terms of effective Lagrangians. Because the mathematical structure of these Lagrangians is not *a priori* known, their construction relies for the most part on symmetry arguments. The various strong and electromagnetic coupling strengths can be determined either from experiment or by resorting to more fundamental models. In this respect, effective-field approaches provide a direct link between quark-model predictions for mesonic/baryonic properties and experimentally accessible quantities, such as scattering cross sections.

Starting from the late eighties, various groups have developed a particular type of effective-Lagrangian model, commonly referred to as the "isobar" approach [23–30]. In these models, the reaction amplitude is constructed from a number of lowest-order (or "tree-level") Feynman diagrams. For $\gamma^{(*)}p \to KY$ (with $\gamma^{(*)}$ a real (virtual) photon), this implies two vertices connected by one intermediate $N^*$, $K^*$ or $Y^*$ particle. Diagrams containing intermediate $N^*$s are denoted as "resonant", since they can produce peaks (resonances) in the cross section. Intermediate kaons and hyperons cause no such peaking behavior, and are called "background" contributions.

While shown to provide a satisfactory description of photo- and electroproduction observables for energies up to 2-3 GeV, such an approximation has its limitations. To account for the $N^*$ resonances' finite lifetimes, decay widths must be introduced, resulting in a breaking of unitarity. Further, higher-order mechanisms like final-state interactions and channel couplings are not included in a tree-level framework. The tree-level coupling constants obtained from fits to experiment should therefore be regarded as *effective* values. These cannot be directly compared to quark-model predictions, because the latter are meant to be plugged into the untruncated amplitudes instead. It has been demonstrated by Chiang *et al.* [31] that the contribution of the intermediate $\pi N$ channel to the $p(\gamma, K^+)\Lambda$ cross sections is of the order of 20%.

In order to resolve some of these problems, several groups have focused on the development of "coupled-channels" strategies [31–35]. These aim at providing a unified description of a set of channels (including $\gamma N$, $\pi N$, $\eta N$, $KY$, ...) by simultaneously modeling all electromagnetic and hadronic reactions which couple them. However, coupled-channels approaches also face unresolved challenges, such as accounting for the $\pi\pi N$ channels, which are responsible for about half of the $\gamma N$ total cross section in the higher-mass $N^*$ region. Furthermore, the large number of parameters involved poses a serious complication. In our opinion, the challenge of clearing up the various ambiguities can be tackled efficiently at the level of the individual reaction channels, where the number of parameters and uncertainties can be kept at a manageable level. In addition, the extension from photo- to electroproduction is relatively straightforward in a tree-level model, whereas, to our knowledge, no coupled-channels approach to kaon electroproduction has as yet been proposed.

## Regge phenomenology and the RPR approach

While adopting hadronic degrees of freedom is justifiable near the $KY$ production threshold, the quark-gluon structure of the interacting particles is bound to manifest itself as higher energies are reached. Not surprisingly, all hadrodynamic approaches, both isobar and coupled-channels, are deficient in their high-energy behavior. While the cross-section data gradually decrease as the energy of the incoming photon increases, the computed cross sections exhibit an unrealistic rise with energy.

This pathology can be remedied without explicitly invoking partonic degrees of freedom. The key is provided by *Regge phenomenology*, a high-energy framework developed in the late fifties as an alternative approach to quantum-mechanical potential scattering [36]. In its simplest form, the Regge model can be formulated as a modified version of the isobar approach. It is distinguished by the property that each intermediate state in the Regge amplitude comprises an entire *family* of hadrons, rather than a single meson or baryon. The members of such a family are characterized by a linear relation between their spin and squared mass, and are said to lie on a "Regge trajectory". The exchange of these trajectories is formally described through the introduction of Regge propagators.

The Regge amplitude is considerably simpler than its isobar-model counterpart, as it does not contain any intermediate $N^*$ states but consists solely of *background* diagrams. This reflects the observation that an ever larger fraction of the nucleon spectrum can be accessed as the photon energy increases. Since most of the contributing $N^*$s have decay widths of several hundreds of MeVs, the resonant structures in the cross section are gradually washed out as the number of overlapping states grows. By the time the photon energy has increased beyond a few GeV, all visible traces of individual $N^*$s have vanished. Under those circumstances, the amplitude can be described by a pure background model. The latter can be explained through the *duality hypothesis* which roughly states that, on average, the sum of all contributing $N^*$ resonances equals the sum of all possible $K^*$- or $Y^*$-trajectory exchanges. Figure 1.2 illustrates the above situation.

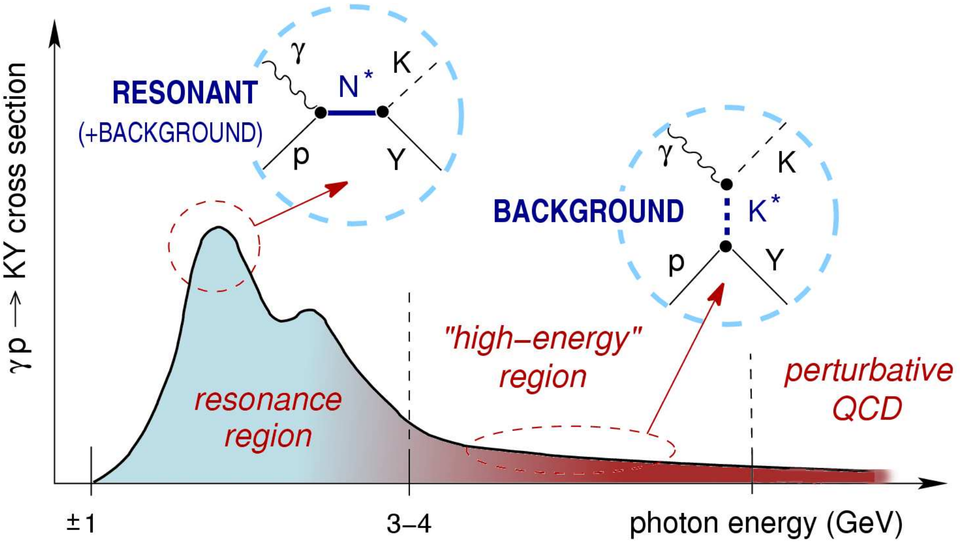

**Figure 1.2** *Schematic representation of the total* KY *photoproduction cross section as a function of the incoming photon energy (in the lab frame). In the resonance region, up to a few GeV, the measured observables exhibit specific structures. This indicates that both background (*$K^*$ *and/or* $Y^*$*) and resonant (*$N^*$*) contributions take part in the reaction dynamics. At higher energies, the presence of a large number of overlapping* $N^*$*s results in a smooth falloff with energy. The corresponding amplitude may be modeled assuming only background diagrams.*

Although Regge phenomenology is a high-energy tool by construction, it has been observed to reproduce the trends of the experimental meson production cross sections down to photon energies of a few GeV. This is not only the case for the pseudoscalar $K$ and $\pi$ mesons [37–40], but also for vector particles like the $\omega$ [41]. It can therefore be assumed that, even in the low-energy domain, the background part of the various meson production amplitudes can be adequately described in the Regge framework. On the other hand, the low-energy cross sections exhibit structures which cannot be reproduced in a pure background model. This obstacle can be surmounted by adding to the Regge amplitude a number of Feynman diagrams containing intermediate $N^*$s or $\Delta^*$s. These resonant contributions should vanish at high energies, where the pure Regge model is valid. This strategy has been applied successfully to high-energy double-pion production in [42], and to the production of $\eta$ and $\eta'$ mesons in [43]. In this thesis, a "Regge-plus-resonance" (or, RPR) model for the $\gamma p \rightarrow KY$ and $ep \rightarrow e'KY$ processes ($Y = \Lambda, \Sigma$) will be developed.

The proposed RPR approach has a number of assets. Firstly, an appropriate high-energy behavior for the observables is automatically ensured. In addition, the fact that the high-energy amplitude only contains background diagrams allows one to determine the background coupling constants from the high-energy data. This leaves the resonance couplings as the sole parameters to be determined in the resonance region. Where traditional effective-Lagrangian models require hadronic form factors, i.e. scalar functions of the exchanged four-momentum, to constrain the high-energy behaviour of the background terms, the use of Regge propagators eliminates the need for such an intervention. In this way, the Regge model allows to circumvent a number of issues, such as how to determine these form factors, and how to remedy the breaking of gauge invariance entailed by their introduction [44].

## Outline

In this work, we will construct a Regge-plus-resonance framework for the electromagnetic production of kaons from the proton.

Chapter 2 describes the effective-field formalism used to model the $p(\gamma, K)Y$ and $p(e, e'K)Y$ reaction amplitudes. We start by defining the various photo- and electroproduction observables and the relevant kinematical variables. Next, we sketch the ingredients of the traditional approach to KY production in the resonance region, known as the isobar model. We then present a strategy to correct the erroneous high-energy behavior of the cross sections obtained in the isobar approach. This involves expressing the high-energy part of the amplitudes in terms of Regge-trajectory exchanges in the t channel. The t-channel Regge propagator, describing the exchange of kaonic trajectories, is discussed in some detail. By supplementing the reggeized background amplitude with a number of s-channel resonances, we extend the Regge model towards the resonance region.

In Chapter 3, we derive the Regge amplitudes for the $K^+\Lambda$, $K^+\Sigma^0$ and $K^0\Sigma^+$ photoproduction reactions. It is shown that the charged-kaon channels are dominated by the exchange of the $K(494)$ and $K^*(892)$ trajectories, whereas the $K^0\Sigma^+$ channel requires the inclusion of an additional $K^*(1410)$ trajectory. The sensitivity of the calculated observables to the various model ingredients, including the Regge-trajectory phases, is investigated in detail.

An RPR description of the $p(\gamma, K)Y$ processes in the resonance region is presented in Chapter 4. Apart from the usual $S_{11}(1650)$, $P_{11}(1710)$ and $P_{13}(1720)$ nucleon resonances, we consider contributions from the two-star $P_{13}(1900)$, as well as the $\Delta^*$ states $S_{31}(1900)$, $P_{31}(1910)$, $D_{33}(1700)$ and $P_{33}(1920)$. We also explore the possibility of a missing $D_{13}(1900)$ or $P_{11}(1900)$. The various resonance parameters are fitted to the resonance-region observables. We compare the results of our RPR calculations with the available photoproduction data.

In Chapter 5, we discuss predictions for the $K^+\Lambda$ and $K^+\Sigma^0$ electroproduction observables. Thereby, we use the RPR amplitudes derived from the photoproduction study, modified by appropriate electromagnetic form factors. We explain how the form factors of the resonant contributions are obtained using the covariant constituent-quark model developed by the Bonn group [45].

Chapter 6 states our conclusions and presents a brief outlook for the future. In Appendix A, we list the various interaction Lagrangians assumed for our calculations. Appendix B sketches the fitting procedure followed in this work. A list of the extracted background and resonance parameters can be found there as well. The main steps in deriving the Regge amplitude for spinless external particles are summarized in Appendix C.

CHAPTER

2

# Models for the $p(\gamma, K)Y$ and $p(e, e'K)Y$ reactions

Since its initial formulation, quantum chromodynamics (QCD) has been thoroughly tested in reactions at very high energies. From the outset, however, efforts to apply it to hadronic processes have been thwarted by several complicating factors. Arguably the most fundamental of these is the non-perturbative nature of the strong interaction at the energy scales typical to "everyday" matter. Although significant progress has been made in *ab initio* computations of QCD on the lattice [6], at this point only static hadron properties have been computed with a reasonable level of confidence. While steps have recently been taken to tackle the $\Delta(1232) \rightarrow \gamma + p$ transition using lattice QCD [46], reliable results for other reactions, particularly strong decays, are not expected in the near future. The interpretation of dynamical hadronic processes thus continues to hinge on models containing some phenomenological ingredients.

A topic which has attracted considerable interest over the years is the transition between the high- and intermediate-energy regimes, where the behavior of hadronic matter is governed by partonic and hadronic degrees of freedom, respectively. Long-standing questions concerning the nature of this transition include the emergence of constituent quarks as effective degrees of freedom, and the origin of spontaneously broken chiral symmetry. We will introduce two complementary theoretical frameworks, either of which allows to tackle a variety of hadronic processes in a specific energy region. The isobar model (Sec. 2.3) is commonly applied to the near-threshold kinematical region, involving center-of-mass energies up to a few GeV. Higher-energy processes, on the other hand, can be efficiently treated with the aid of Regge phenomenology (Secs. 2.4.1 and 2.4.2). The main objective of this work is to construct a hybrid "Regge-plus-resonance" (RPR) framework, valid over the entire energy region covered by the isobar and Regge descriptions (Sec. 2.4.3). We start out by putting the $p(\gamma^{(*)}, K)Y$ reaction into the more general context of hadronic physics (Sec. 2.1).

## 2.1 Studying the strangeness channels

### 2.1.1 Motivation and challenges

Among all known manifestations of strongly interacting matter, a main protagonist in the field of hadronic physics is still the most common hadron in existence: the nucleon. Attaining a full picture of its internal structure, as reflected for example by its excitation spectrum, is envisaged as a stepping-stone to unlocking some of the more subtle aspects of QCD. The excitation of nucleon resonances (abbreviated $N^*$s) can be accomplished through the transfer of energy to a free or bound proton by means of an external probe.

Since hadronic probes, primarily pions, boast the largest interaction cross sections, results from pion-induced experiments have long made up the bulk of $N^*$ data. While experimentally more challenging to use, leptonic probes have the theoretical advantage of interacting with the struck proton through the electroweak interaction, which is better understood than the strong one. Ever since the advent of sufficiently sensitive detectors, an impressive amount of effort has been devoted to unraveling the $N^*$ spectrum through the study of photo- and electroinduced meson production from the nucleon. A strong motivation for studying this type of reaction involves finding a solution to the so-called "missing-resonance" problem. It turns out that a considerable fraction of the resonances predicted by constituent-quark (CQ) models [8–12] have so far remained unobserved. Proof of the existence of these missing states would constitute a strong confirmation of the validity of the CQ concept. On the other hand, if no solid evidence emerges, the concept of CQs as appropriate degrees of freedom could be at stake. A quark-diquark picture represents a possible alternative.

Most of the available $N^*$ information stems from experiments involving $\pi N$ final states. It cannot be excluded, though, that a study of alternative reaction channels, such as $\gamma^{(*)}N \to \omega N$, $\eta N$, $\pi\pi N$ and $KY$, may reveal the existence of missing $N^*$s. This suspicion is backed up by claims from CQ-model calculations that several of the as yet unobserved resonances couple more strongly to other final states than to the traditional $\pi N$ one [16]. Associated open-strangeness production reactions are particularly

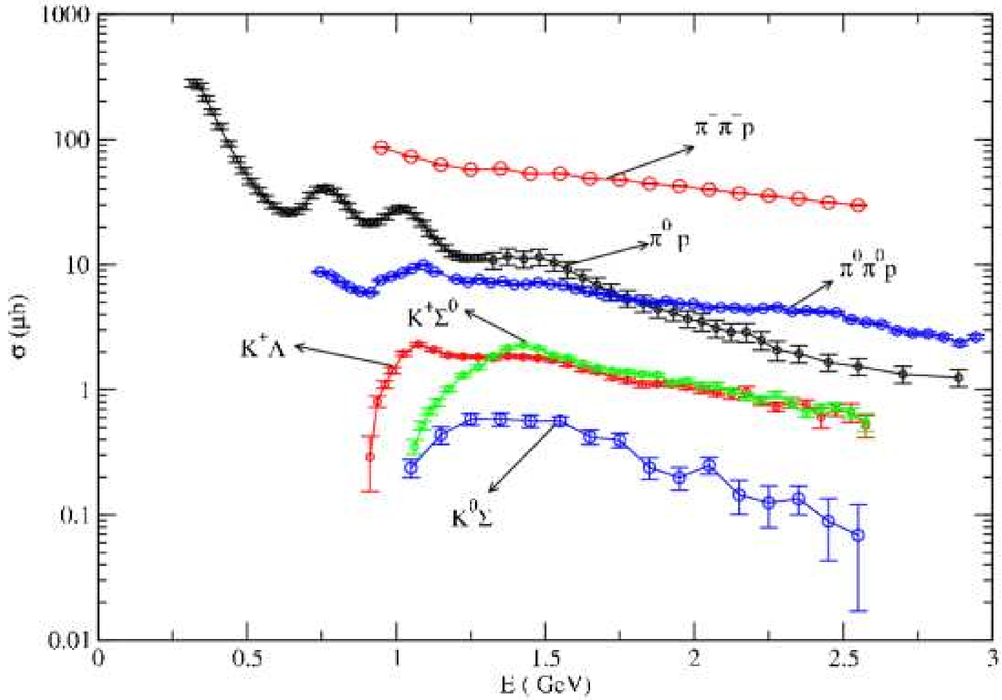

**Figure 2.1** Dominant contributions making up the total cross section for photoproduction from a free proton [47]. Data for one- and two-meson final states are displayed.

interesting due to the creation of a strange quark-antiquark pair. A thorough grasp of the $p(\gamma, K)Y$ and $p(e, e'K)Y$ dynamics is also required for the description of photo- and electroinduced hypernuclear production, a field which has been rapidly gaining momentum over the past few years.

A detailed study of electromagnetic KY production is considerably more challenging than $\pi N$ production. This is illustrated by Fig. 2.1, which compares the total cross sections for photoproduction of various meson-baryon states. The curves for the $p(\gamma, K^+)\Lambda, \Sigma^{0,+}$ processes are one to two orders of magnitude below those for $p(\gamma, \pi^0)p$, implying much smaller count rates. Secondly, because the thresholds are significantly higher, already at the lowest possible energies several overlapping resonances can contribute to the KY production dynamics. This severely complicates the theoretical description.

### 2.1.2 Historical context

The starting shot for the experimental study of kaon photoproduction was officially given in 1957, when both Caltech [48] and Cornell [49] released $p(\gamma, K^+)\Lambda$ cross-section data obtained at their electron synchrotrons. The few datapoints reported in these pioneering publications were of a limited accuracy, and only the kinematical region very close to threshold could be probed due to the limited electron energies available at that time. It was not until the next decade that the first attempts were made to formulate a theoretical model for the measured observables, first by Kuo [50] and later by Thom [51].

Further experiments were performed in the 1970s and 1980s, not solely in the US but also at facilities in Bonn [52] and Tokyo [53]. This prompted Adelseck *et al.* [54] to re-evaluate the kaon-production operator originally proposed by Thom. Adelseck's model laid the foundations of the most wide-spread theoretical treatment of electromagnetic (EM) strangeness production: the isobar approach.

At the end of the nineties the SAPHIR collaboration, operating at the Bonn ELSA facility, released the first high precision data for all three reaction channels $\gamma p \rightarrow K^+\Lambda$, $\gamma p \rightarrow K^+\Sigma^0$ and $\gamma p \rightarrow K^0\Sigma^+$ over the photon energy range from threshold up to 2 GeV [55, 56]. These data triggered a flood of initiatives in the theoretical community, while also sparking renewed interest in the search for missing resonances.

Over the past years, the $p(\gamma, K)Y$ database has been supplemented with high-precision $\gamma p \rightarrow K^+\Lambda$ and $\gamma p \rightarrow K^+\Sigma^0$ data from the CLAS [57–59], SAPHIR [60], LEPS [61, 62] and GRAAL [63] collaborations. SAPHIR has also provided a new analysis of the $\gamma p \rightarrow K^0\Sigma^+$ channel [64]. In addition, the CLAS collaboration has analyzed the $p(e, e'K^+)\Lambda, \Sigma^0$ processes [65–67]. Previous measurements of the electroproduction reactions date back from the late seventies [68–70]. In the light of these developments, a reassessment of the theoretical descriptions of the $\gamma p \rightarrow KY$ processes appears to be in order.

## 2.2 Kinematics and observables

Due to the small QED coupling constant ($\alpha_e \approx 1/137$), electromagnetic processes can be successfully described by perturbation theory. It has long been taken for granted that a lowest-order approximation suffices for reactions involving a combination of leptonic and hadronic interactions. Nearly all theoretical approaches to $p(e, e'K)Y$ are built upon the supposition that the electron beam and the target proton communicate through the exchange of a single photon. Figure 2.2 shows a schematic representation of the $p(e, e'K)Y$ process in the one-photon exchange approximation (OPEA). The exchanged (virtual) photon $\gamma^*(k)$ connects the leptonic and hadronic reaction planes, which are arranged under an angle $\varphi_K$. In the photoproduction case, the photon is on-shell so $Q^2 = -k^2 = 0$, and there is only a hadronic plane.

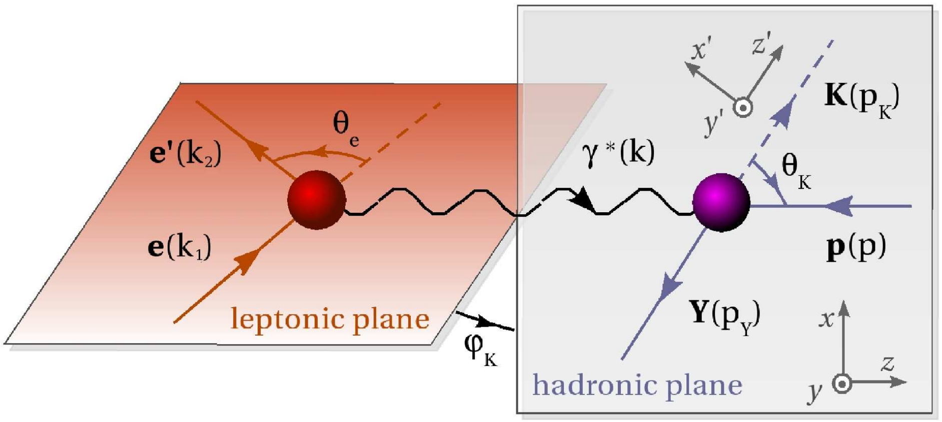

**Figure 2.2** Definition of the reference frames and kinematic variables for the $p(e, e'K)Y$ process. In photoproduction reactions, there is no leptonic plane.

### 2.2.1 KY photoproduction

The kinematical quantities involved in the photoproduction reaction

$$p\,(p) + \gamma\,(k) \to K\,(p_K) + Y\,(p_Y)\ , \tag{2.1}$$

with $\gamma$ a real photon, are indicated in Fig. 2.2. It is convenient to express the different four-momenta in the center-of-mass (COM) frame:

$$\begin{aligned} k &= (\omega^*, \vec{k}^*)\ , \qquad & p_K &= (E_K^*, \vec{p}_K^*)\ , \\ p &= (E_p^*, -\vec{k}^*)\ , \qquad & p_Y &= (E_Y^*, -\vec{p}_K^*)\ , \end{aligned} \tag{2.2}$$

with $E_h^* = \sqrt{m_h^2 + |\vec{p}_h^*|^2}$ ($h = p, k, Y$), and $|\vec{k}^*| = \omega^*$. As the energy-conservation relation

$$\omega^* + \sqrt{m_p^2 + \omega^{*2}} = \sqrt{m_K^2 + |\vec{p}_K^*|^2} + \sqrt{m_Y^2 + |\vec{p}_K^*|^2} \tag{2.3}$$

determines $|\vec{p}_K^*|$ as a function of $\omega^*$, the reaction dynamics depend solely on the COM kaon scattering angle $\theta_K^*$ (defined in Fig. 2.2) and the incoming photon energy. Because the latter is measured in the laboratory frame, experimental results are usually presented as a function of $\omega_{lab}$ rather than $\omega^*$. The two are linked through a Lorentz transformation [71]:

$$\omega_{lab} = \frac{\omega^*}{m_p}\left[\omega^* + \sqrt{m_p^2 + \omega^{*2}}\right] = \omega^* \frac{W}{m_p}\ , \text{ or} \tag{2.4}$$

$$\omega^* = \omega_{lab} \frac{m_p}{\sqrt{(\omega_{lab} + m_p)^2 - \omega_{lab}^2}} \tag{2.5}$$

where $W(=\omega^* + E_p^*)$ is the total COM energy of the reaction. It is often more useful to express the observables in terms of the Lorentz invariant Mandelstam variables

$$s = (k+p)^2 \equiv W^2\,, \qquad t = (k - p_K)^2\,, \qquad u = (k - p_Y)^2\,, \tag{2.6}$$

which are related by $s + t + u = m_p^2 + m_Y^2 + m_K^2$.

### Transition amplitude

The basic expression for the differential $p(\gamma, K)Y$ cross section is given by [72]

$$\frac{d\sigma}{d\Omega_K^*} \equiv \frac{1}{2\pi}\frac{d\sigma}{d\cos\theta_K^*} = \frac{1}{64\,\pi^2}\,\frac{|\vec{p}_K^{\,*}|}{\omega^*}\,\frac{1}{(\omega^* + E_p^*)^2}\,\overline{\sum}_{\lambda,\lambda_i,\lambda_f}|\mathcal{M}_\lambda^{\lambda_i,\lambda_f}|^2 \tag{2.7}$$

with $\lambda$, $\lambda_i$ and $\lambda_f$ the photon, proton and hyperon polarizations. $\overline{\sum}_{\lambda,\lambda_i,\lambda_f}$ represents the averaging and/or summing over the initial and/or final polarizations which remain unobserved experimentally. The squared amplitude assumes the form

$$\left|\mathcal{M}_\lambda^{\lambda_i\lambda_f}\right|^2 \;=\; \left(\overline{u}_Y^{\lambda_f}(p_Y)\,T^\mu\varepsilon_\mu^\lambda\; u_p^{\lambda_i}(p)\right)\left(\overline{u}_p^{\lambda_i}(p)\,\overline{T}^\nu\varepsilon_\nu^{\lambda *}\; u_Y^{\lambda_f}(p_Y)\right)\,, \tag{2.8}$$

introducing $T^\mu$ as the "truncated" current, from which the spinors of the external proton and hyperon fields have been removed. Further, $\overline{T}^\mu$ is defined as $\gamma^0\,(T^\mu)^\dagger\,\gamma^0$ and $\varepsilon_\mu^\lambda$ is the photon field polarization four-vector.

### Polarized and unpolarized cross sections

It can be demonstrated that, irrespective of the nature of the observed polarizations, Eq. (2.8) can be re-written as the trace of a product of Dirac matrices. For an unpolarized photon beam, the summation over $\lambda$ can be carried out using the replacement

$$\sum_{\lambda=\pm 1}\varepsilon_\mu^\lambda\varepsilon_\nu^{\lambda *} \to -\,g_{\mu\nu} \tag{2.9}$$

under the condition that the amplitude is gauge invariant [73]. If the polarization of the participating hadrons also remains unknown, averaging and summing over $\lambda_i$ and $\lambda_f$ reduces the Feynman amplitude to:

$$\overline{\sum_{\lambda_i\lambda_f\lambda}}\left|M_\lambda^{\lambda_i\lambda_f}\right|^2 \;=\; -\frac{1}{4}\mathrm{Tr}\left\{(\not{p}_Y + m_Y)\,T^\mu\,(\not{p} + m_p)\,\overline{T}_\mu\right\}\,, \tag{2.10}$$

where we have applied the spin sum rule $\sum_\lambda u_a^\lambda(q)\,\overline{u}_b^\lambda(q) = (\not{q} + m)_{ab}$, with $a$ and $b$ Dirac indices.

When the photon beam is polarized, the four-vectors $\varepsilon^{\lambda}$ have to be substituted by their explicit expressions. For photons that are linearly polarized, for example along $\vec{x}$ and $\vec{y}$, these read

$$\varepsilon^{\lambda=x} = (0,1,0,0) \ , \qquad \varepsilon^{\lambda=y} = (0,0,1,0) \ , \tag{2.11}$$

whereas for circularly polarized photons

$$\varepsilon^{\lambda=+1} = -\frac{1}{\sqrt{2}}\,(0,1,i,0) \ , \qquad \varepsilon^{\lambda=-1} = \frac{1}{\sqrt{2}}\,(0,1,-i,0) \ . \tag{2.12}$$

When the polarization $\lambda_{p,Y}$ of the proton or hyperon is specified, a spin projection operator [73]

$$\Pi^{\pm}(n_{p,Y}) = \frac{1}{2}\,(1 \pm \gamma_5 \ \not{n}_{p,Y}) \ , \tag{2.13}$$

can be inserted in front of the appropriate spinor, after which the spin summation can be carried out. Again, this allows one to write the polarized cross section in the form of a trace. In the rest frame of the polarized particle, the spin-projection four vector is defined as $n = (0, \vec{n})$, with $\vec{n}$ the unit vector along the spin quantization axis. If $q$ is the four-momentum in an arbitrary frame, it is therefore guaranteed that $n^2$ = -1 and $(n \cdot q)$ = 0. The expressions for $n_p$ and $n_Y$ in the $(x, y, z)$ and $(x', y', z')$ frames from Fig. 2.2 are given for example in [74].

### Polarization asymmetries

When one or more of the external particles are polarized, the relevant observable is generally expressed in the form of an *asymmetry*. Single-polarization asymmetries are defined as

$$\frac{d\sigma^{+} - d\sigma^{-}}{d\sigma^{+} + d\sigma^{-}} \ , \tag{2.14}$$

where + (−) refers to a polarization parallel (anti-parallel) with the respective quantization axis or helicity state. Analogously, one defines double polarization asymmetries as

$$\frac{d\sigma^{(++)} + d\sigma^{(--)} - d\sigma^{(+-)} - d\sigma^{(-+)}}{d\sigma^{(++)} + d\sigma^{(--)} + d\sigma^{(+-)} + d\sigma^{(-+)}} \ . \tag{2.15}$$

All nonzero asymmetry observables are summarized in Table 2.1 along with the usual choice of quantization axes. It should be noted that the fifteen quantities listed in this

| Observable | Required polarization | | |
|---|---|---|---|
| | Beam | Target | Recoil |
| *Single polarization* | | | |
| $\Sigma$ | linear | - | - |
| $T$ | - | along $y$ | - |
| $P$ | - | - | along $y'$ |
| *Beam-target polarization* | | | |
| $E$ | circular | along $z$ | - |
| $F$ | circular | along $x$ | - |
| $G$ | linear | along $z$ | - |
| $H$ | linear | along $x$ | - |
| *Beam-recoil polarization* | | | |
| $C_{x'}$ | circular | - | along $x'$ |
| $C_{z'}$ | circular | - | along $z'$ |
| $O_{x'}$ | linear | - | along $x'$ |
| $O_{z'}$ | linear | - | along $z'$ |
| *Target-recoil polarization* | | | |
| $T_{x'}$ | - | along $x$ | along $x'$ |
| $T_{z'}$ | - | along $x$ | along $z'$ |
| $L_{x'}$ | - | along $z$ | along $x'$ |
| $L_{z'}$ | - | along $z$ | along $z'$ |

**Table 2.1** Definition of the polarized photoproduction observables. The quantization axes for the polarization asymmetries are defined as follows: $\vec{z} \sim \vec{k}$, $\vec{y} \sim (\vec{k} \times \vec{p}_K)$, $\vec{x} = \vec{y} \times \vec{z}$, $\vec{z}' \sim \vec{p}_K$, $\vec{y} = \vec{y}'$, $\vec{x}' = \vec{y}' \times \vec{z}'$. The two reference frames are also shown in Fig. 2.2. Note that, in computing the double-polarization observables $G$, $H$, $O_{x'}$ and $O_{z'}$, the photon polarization directions are generally taken under angles of $\pm\pi/4$ with respect to the scattering plane. To obtain the beam asymmetry $\Sigma$, the photons are assumed to be polarized along $x$ and $y$.

table are not independent. They are connected by six non-linear relations [75,76]:

$$
\begin{aligned}
&E^2 + F^2 + G^2 + H^2 = 1 + P^2 - \Sigma^2 - T^2 \ , \\
&FG - EH = P - \Sigma T \ , \\
&C_x^2 + C_z^2 + O_x^2 + O_z^2 = 1 + T^2 - P^2 - \Sigma^2 \ , \\
&C_z O_x - C_x O_z = T - P\Sigma \ , \\
&T_x^2 + T_z^2 + L_x^2 + L_z^2 = 1 + \Sigma^2 - P^2 - T^2 \ , \\
&T_x L_z - T_z L_x = \Sigma - PT \ ,
\end{aligned}
\tag{2.16}
$$

For practical reasons, an asymmetry is sometimes expressed in a different reference frame than the one indicated in Table 2.1. For example, the beam-recoil asymmetries presented in Ref. [59] are defined with respect to the $(xyz)$ axes instead of the usual $(x'y'z')$ ones. In that case, a passive rotation of the coordinate frame allows to convert

$C_{x',z'}$ into $C_{x,z}$:

$$C_x = C_{x'} \cos\theta^*_K + C_{z'} \sin\theta^*_K \,, \tag{2.17}$$

$$C_z = -C_{x'} \sin\theta^*_K + C_{z'} \cos\theta^*_K \,. \tag{2.18}$$

### 2.2.2 KY electroproduction

In describing the electroproduction reaction

$$p\,(p) + e\,(k_1) \to e'\,(k_2) + K\,(p_K) + Y\,(p_Y) \;, \tag{2.19}$$

it is convenient to consider the leptonic and hadronic parts of the amplitude in different reference frames. When expressing the electron kinematics in the laboratory frame and the hadron kinematics in the virtual photon-proton COM frame, the relevant four-momenta are given by

$$\begin{array}{lllllllll} k_1 & = & (\varepsilon_1, \vec{k}_1) \;, & p & = & (E^*_p, -\vec{k}^*) \;, & p^\mu_K & = & (E^*_K, \vec{p}_K^{\,*}) \;, \\ k_2 & = & (\varepsilon_2, \vec{k}_2) \;, & k & = & k_1 - k_2 = (\omega, \vec{k}) \;, & p^\mu_Y & = & (E^*_Y, -\vec{p}_K^{\,*}) \;. \end{array} \tag{2.20}$$

The virtual photon is responsible for the transfer of information from the leptonic to the hadronic frame. Its four-momentum components in the lab and COM frames are connected through the relations

$$\vec{k}^* = \vec{k}\left(\frac{m_p}{W}\right) \;, \tag{2.21}$$

$$\begin{aligned} \omega^* &= W - (\omega + m_p)\,\frac{m_p}{W} \;, \\ &= \frac{s - m_p^2 - Q^2}{2W} \;, \end{aligned} \tag{2.22}$$

with $Q^2 = -k^2$.

#### Transition amplitude

The $p(e, e'K)Y$ differential cross section assumes the form [73]

$$\frac{d\sigma}{d\varepsilon_2 d\Omega_2 d\Omega^*_K} = \frac{1}{32\,(2\pi)^5}\frac{1}{m_p}\frac{|\vec{p}_K^{\,*}|}{W}\frac{\varepsilon_2}{\varepsilon_1}\overline{\sum}_{\lambda_i} |\mathcal{T}_{\lambda_i}|^2 \;, \tag{2.23}$$

where

$$\overline{\sum}_{\lambda_i} |\mathcal{T}_{\lambda_i}|^2 \equiv \overline{\sum}_{\lambda_1\lambda_2\lambda'_1\lambda'_2} \left|\mathcal{T}^{\lambda'_1\lambda'_2}_{\lambda_1\lambda_2}\right|^2 \;, \tag{2.24}$$

with $\lambda_1$, $\lambda_2$, $\lambda'_1$ and $\lambda'_2$ the nucleon, hyperon, and initial and final electron polarizations. The transition amplitude $\mathcal{T}$ is the product of a leptonic current $l^{\lambda'_1\lambda'_2}_\mu$, a photon propagator, and a hadronic current $J^{\lambda_1\lambda_2}_\nu$:

$$\mathcal{T}^{\lambda'_1\lambda'_2}_{\lambda_1\lambda_2} = e\, l^{\lambda'_1\lambda'_2}_\mu \,\frac{-g^{\mu\nu}}{k^2}\, J^{\lambda_1\lambda_2}_\nu \;. \tag{2.25}$$

The relation [73]

$$\sum_{\lambda=0,\pm1} (-1)^{\lambda}\, \varepsilon_{\lambda}^{\mu *} \varepsilon_{\lambda}^{\nu} = g^{\mu\nu} + \frac{k^{\mu}k^{\nu}}{Q^2} \tag{2.26}$$

may be used to re-write this as

$$\mathcal{T}_{\lambda_1\lambda_2}^{\lambda_1'\lambda_2'} = \frac{e}{Q^2} \sum_{\lambda=0,\pm1} (-1)^{\lambda}\, L_{\lambda}^{\lambda_1'\lambda_2' *} \mathcal{M}_{\lambda}^{\lambda_1\lambda_2} \;, \tag{2.27}$$

under the condition that either the leptonic or the hadronic current (or both) are gauge invariant. Eq. (2.27) contains the so-called leptonic and hadronic tensors, given by

$$L_{\lambda}^{\lambda_1'\lambda_2' *} = l_{\mu}^{\lambda_1'\lambda_2'} \varepsilon_{\lambda}^{\mu *} \;, \qquad \mathcal{M}_{\lambda}^{\lambda_1\lambda_2} = J_{\mu}^{\lambda_1\lambda_2} \varepsilon_{\lambda}^{\mu} \,. \tag{2.28}$$

As a result, the unpolarized squared amplitude can be written as:

$$\sum_{\lambda_i} |\mathcal{T}_{\lambda_i}|^2 = \frac{1}{4}\frac{e^2}{Q^4} \sum_{\lambda\lambda'=0,\pm1} \mathcal{L}_{\lambda\lambda'} \mathcal{H}_{\lambda\lambda'} \;, \tag{2.29}$$

with the leptonic and hadronic contributions

$$\mathcal{L}_{\lambda\lambda'} = \sum_{\lambda_1\lambda_2} (-1)^{\lambda+\lambda'}\, L_{\lambda}^{\lambda_1\lambda_2} \left(L_{\lambda'}^{\lambda_1\lambda_2}\right)^{\dagger} \;, \tag{2.30}$$

$$\mathcal{H}_{\lambda\lambda'} = \sum_{\lambda_1\lambda_2} \mathcal{M}_{\lambda}^{\lambda_1\lambda_2} \left(\mathcal{M}_{\lambda'}^{\lambda_1\lambda_2}\right)^{\dagger} \,. \tag{2.31}$$

Since the leptonic tensor $\mathcal{L}_{\lambda\lambda'}$ can be calculated from the QED Feynman rules, the right-hand side of Eq. (2.23) can be interpreted as a linear combination of cross sections for the $p(\gamma^*, K)Y$ process, involving virtual photon parameterizations $\lambda$ and $\lambda'$, multiplied by factors corresponding to the electron kinematics. Depending on which polarizations are measured in the reaction, Eq. (2.29) can be cast into a number of more practical forms.

### Unpolarized cross section

It can be demonstrated that the cross section for unpolarized electroproduction may be expressed as [77,78]

$$\begin{aligned}\frac{d\sigma}{d\varepsilon_2 d\Omega_2 d\Omega_K^*} = \Gamma \Bigg[ & \frac{d\sigma_T}{d\Omega_K^*} + \varepsilon \frac{d\sigma_L}{d\Omega_K^*} \\ & + \varepsilon \frac{d\sigma_{TT}}{d\Omega_K^*} \cos(2\varphi_K^*) + \sqrt{\varepsilon(1+\varepsilon)} \frac{d\sigma_{LT}}{d\Omega_K^*} \cos(\varphi_K^*) \Bigg] \,. \end{aligned} \tag{2.32}$$

with the virtual photon flux factor given by

$$\Gamma = \frac{\alpha}{2\pi^2} \frac{\varepsilon_2}{\varepsilon_1} \frac{K_H}{Q^2} \frac{1}{1-\varepsilon} \;, \tag{2.33}$$

and

$$K_H = \omega_{lab} - \frac{Q^2}{2m_p}$$

the equivalent real photon lab energy. Further, $\varepsilon$ is defined as

$$\varepsilon = \left(1 + \frac{2|\vec{k}|^2}{Q^2} \tan^2 \frac{\theta_e}{2}\right)^{-1} . \tag{2.34}$$

We should mention that many different conventions for Eq. (2.32) exist in literature. For example, instead of $\varepsilon$, one can use the quantity $\varepsilon_L$, for which multiple definitions exist:

$$\varepsilon_L = \frac{Q^2}{|\vec{k}|^2}\,\varepsilon \quad \text{or} \quad \frac{Q^2}{\omega^2}\,\varepsilon \quad \text{or} \quad \frac{Q^2}{\omega^{*2}}\,\varepsilon\,. \tag{2.35}$$

Alternatively, an extra factor of $\sqrt{2}$ may be included in some of the terms [65]. With the conventions from Eq. (2.32), the virtual photon cross sections can be calculated as:

$$\frac{d\sigma_T}{d\Omega_K^*} = \chi \frac{1}{(4\pi)^2} \left(\mathcal{H}_{1,1} + \mathcal{H}_{-1,-1}\right) , \tag{2.36}$$

$$\frac{d\sigma_L}{d\Omega_K^*} = 2\,\chi \frac{1}{(4\pi)^2} \mathcal{H}_{0,0} , \tag{2.37}$$

$$\frac{d\sigma_{TT}}{d\Omega_K^*} = -\chi \frac{1}{(4\pi)^2} \left(\mathcal{H}_{1,-1} + \mathcal{H}_{-1,1}\right) , \tag{2.38}$$

$$\frac{d\sigma_{LT}}{d\Omega_K^*} = -\chi \frac{1}{(4\pi)^2} \left(\mathcal{H}_{0,1} + \mathcal{H}_{1,0} - \mathcal{H}_{-1,0} - \mathcal{H}_{0,-1}\right) . \tag{2.39}$$

with $\chi$ a kinematical factor given by:

$$\chi \equiv \frac{1}{16} \frac{1}{W m_p} \frac{|\vec{p}_K^{\,*}|}{K_H} . \tag{2.40}$$

As the $\varphi_K^*$-dependence has been isolated from the structure functions (Eq. (2.32)), they solely depend on the variable set $(\omega^*, |\vec{k}^*|, \theta_K^*)$.

As in the photoproduction case, the hadronic tensor components $\mathcal{H}_{\lambda\lambda'}$ can be rewritten as traces of Dirac matrices. The virtual photon polarization four-vectors are given by

$$\varepsilon^{\lambda=0} = \frac{1}{\sqrt{Q^2}} (|\vec{k}^*|, 0, 0, \omega^*) , \qquad \varepsilon^{\lambda=\pm 1} = \mp \frac{1}{\sqrt{2}} (0, 1, \pm i, 0) . \tag{2.41}$$

where a longitudinal polarization ($\lambda = 0$) is now possible as well.

### Polarized electrons

With a polarized electron beam, two additional terms enter the expression for the cross section:

$$\frac{d\sigma}{d\varepsilon_2 d\Omega_2 d\Omega_K^*} = \left.\frac{d\sigma}{d\varepsilon_2 d\Omega_2 d\Omega_K^*}\right|_{\text{unpol}} + h\,\Gamma\left[\sqrt{1-\varepsilon^2}\,\frac{d\sigma_{TT'}}{d\Omega_K^*} + \sqrt{\varepsilon\,(1-\varepsilon)}\,\frac{d\sigma_{LT'}}{d\Omega_K^*}\sin\left(\varphi_K^*\right)\right] . \tag{2.42}$$

Herein, $h = \pm 1$ is the helicity of the incident electron, and

$$\frac{d\sigma_{TT'}}{d\Omega_K^*} = \chi\,\frac{1}{(4\pi)^2}\left(\mathcal{H}_{1,1} - \mathcal{H}_{-1,-1}\right) , \tag{2.43}$$

$$\frac{d\sigma_{LT'}}{d\Omega_K} = -\chi\,\frac{1}{(4\pi)^2}\left(\mathcal{H}_{1,0} - \mathcal{H}_{0,1} - \mathcal{H}_{-1,0} + \mathcal{H}_{0,-1}\right) . \tag{2.44}$$

Because of the structure of the hadron current, the $TT'$ term is identical to zero if no baryon polarizations are involved in the process.

### Polarized baryons

When the polarization $\lambda_{p,Y}$ of the target proton and/or recoil hyperon is measured, a similar technique as in the real-photon case can be applied. By inserting the relevant spin-projection operator(s) $\Pi^{\pm}\left(n_{p,Y}^{\beta,\alpha}\right) = \frac{1}{2}\left(1 \pm \gamma_5 \not{n}_{p,Y}^{\beta,\alpha}\right)$ into the amplitude, the polarized cross section can be expressed in terms of a set of response functions $R^{\alpha\beta}$. Herein, $\alpha$ and $\beta$ correspond to the hyperon and proton polarization directions, respectively: $\alpha = x', y', z'$ and $\beta = x, y, z$. The notation $\alpha$ or $\beta = 0$ is used to refer to an unpolarized hyperon or proton.

In this work, we only consider the situation of a polarized electron beam and polarized recoil hyperons. The observables for such an $\vec{e}p \rightarrow e'K\vec{\Lambda}$ reaction are usually formulated as *transferred polarization* components. While these components depend on the angle $\varphi_K$, the data are usually summed over all $\varphi_K$ to improve statistical precision. Using the conventions from Ref. [65], the nonzero $\varphi_K$-integrated polarization components in the $(x, y, z)$ and $(x', y', z')$ reference frames are given by:

$$P'_{x'} = c_1\,R_{TT'}^{x'0} , \tag{2.45}$$

$$P'_{x'} = c_1\,R_{TT'}^{z'0} , \tag{2.46}$$

$$P'_{x} = c_2\left(R_{LT'}^{x'0}\cos\theta_K^* - R_{LT'}^{y'0} + R_{LT'}^{z'0}\sin\theta_K^*\right) , \tag{2.47}$$

$$P'_{z} = c_1\left(-R_{LT'}^{x'0}\sin\theta_K^* R_{LT'}^{z'0}\cos\theta_K^*\right) , \tag{2.48}$$

with $c_1 = \sqrt{1-\varepsilon^2}/K_0$ and $c_2 = \sqrt{2\varepsilon_L(1-\varepsilon)}/2K_0$, where $K_0 = R_T^{00} + \varepsilon_L R_L^{00}$ and $\varepsilon_L = \varepsilon Q^2/\omega^{*2}$. The response functions in the $(x', y', z')$ frame, i.e. the natural frame in which to express the hyperon polarization four-vector $n_Y$, are given by

$$\begin{aligned} R_{TT'}^{\alpha 0} &= \rho^{-1} \chi \frac{1}{(4\pi)^2} \left(\mathcal{H}_{1,1} - \mathcal{H}_{-1,-1}\right) \\ {}^cR_{LT'}^{\alpha 0} &= -\rho^{-1} \chi \frac{1}{(4\pi)^2} \left(\mathcal{H}_{1,0} + \mathcal{H}_{0,1} + \mathcal{H}_{-1,0} + \mathcal{H}_{0,-1}\right) \\ {}^sR_{LT'}^{\alpha 0} &= -\rho^{-1} \chi \frac{i}{(4\pi)^2} \left(\mathcal{H}_{1,0} - \mathcal{H}_{0,1} - \mathcal{H}_{-1,0} + \mathcal{H}_{0,-1}\right) \end{aligned} \tag{2.49}$$

where the $\alpha, \beta$ indices of the hadronic tensor have been suppressed. Further, $\rho = |\vec{p}_K^*|/|\vec{k}^*|$, and all hadron tensors should be calculated at $\varphi_K^* = 0$. More details can be found for example in Refs. [65,74,79].

## 2.3 Resonance dynamics and the isobar model

Except at very high energies, where QCD can be solved perturbatively, quarks and gluons do not represent the optimum building blocks in hadronic reaction models. More appropriate degrees of freedom in the nonperturbative regime are constituent quarks (CQs), to be imagined as elementary quarks "dressed" by a cloud of gluons and quark-antiquark pairs, and the bound conglomerates of CQs, i.e. mesons and baryons. Because the properties of these objects are not fully determined by the fundamental field theories, they are referred to as *effective* degrees of freedom. Which effective building blocks to use depends on the energies one aims to describe. Near the $p(\gamma, K)Y$ threshold there are obvious structures in the cross sections, reflecting the production of individual $N^*$ and/or $\Delta^*$ states. A logical strategy to model these is to employ hadrons in their entirety as effective degrees of freedom.

### 2.3.1 Tree-level amplitude

The theoretical description of the $p(\gamma, K)Y$ and $p(e, e'K)Y$ processes can be efficiently realized in an effective-field framework, where the interactions are modelled by means of effective Lagrangians. Thereby, every hadron is treated as a robust entity, characterized by intrinsic properties such as mass, charge, form factors, and coupling constants. This work adopts the so-called *tree-level* approximation, implying that only the Feynman diagrams with the smallest possible number of interaction vertices are considered. Tree-level effective-field approaches are commonly known under the name of *isobar* models.

The different elements of the lowest-order $p(\gamma^{(*)}, K)Y$ amplitude are shown in Fig. 2.3. In the OPEA, the $p(e, e'K)Y$ diagram is obtained by adding a $(\gamma^* ee')$ vertex at the end of the photon line. As indicated in Fig. 2.3, the various types of tree-level diagrams can be classified in several ways. The left column collects the *Born terms*, which have a ground-state hadron in the intermediate state. Depending on whether the exchanged particle is a nonstrange hadron ($N^*$ or $\Delta^*$), a kaon, or a hyperon, one further distinguishes between $s$-, $t$- and $u$-channel contributions. The pole structure of a tree-level diagram is determined by its intermediate-particle propagator $\mathcal{P} \sim \frac{1}{q^2 - m^2}$, with $m$ and $q$ the mass and four-momentum of the exchanged hadron. Only for the $s$-channel terms involving an excited state (red diagram) can these propagators actually go through their poles and produce resonant structures in the observables. The $t$- and $u$-channel diagrams and the $s$-channel Born term are *background* contributions, as energy-momentum conservation prevents their poles from being reached.

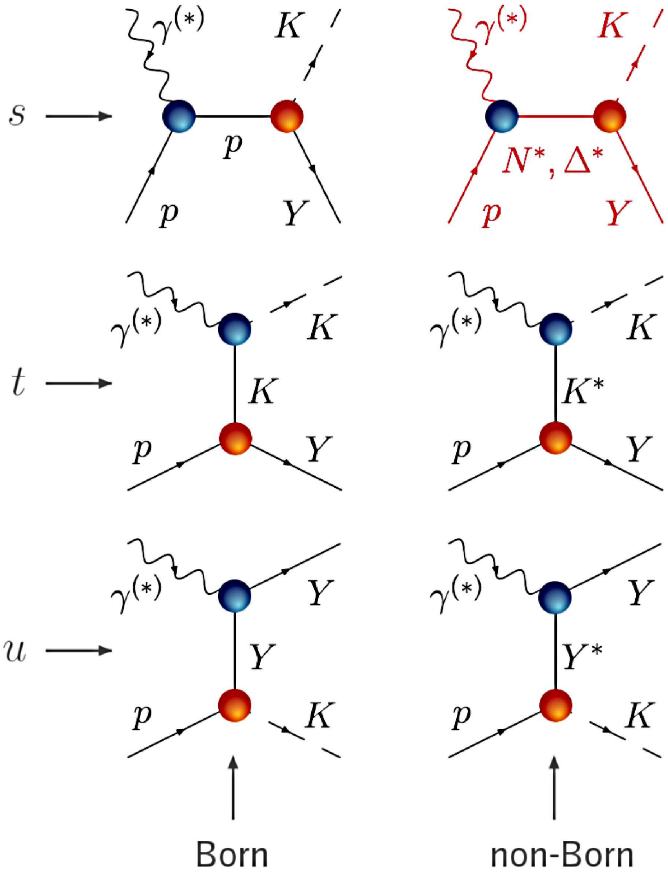

**Figure 2.3** Tree-level contributions to the $p(\gamma^{(*)}, K)Y$ amplitude ($Y = \Lambda, \Sigma^{0,+}$). Note that $\Delta^*$ states can only be produced in the $K\Sigma$ channels for reasons of isospin conservation.

A summary of the strong and electromagnetic Lagrangians used in our calculations is given in Appendix A.1. The various intermediate-particle propagators are listed there as well. We have used effective interactions defined as in the work of Janssen [71].

### Effective fields and interactions

Although built upon the same set of formal principles, effective-Lagrangian models face a number of challenges unknown to the fundamental field theories.

**Model parameters.** Not all ingredients of an effective-field framework can be determined from first principles. In constructing the various interaction Lagrangians, one is forced to rely on symmetry arguments and conservation laws. In some situations, such as for the strong and EM couplings to spin-0 and spin-1/2 hadrons at $Q^2 = 0$, a unique "standardized" form for the vertex factor is available. Lagrangians for higher-spin states, however, can seldom be formulated unambiguously. A prime example is the spin-3/2 field [80–82]. In electroproduction reactions, the situation is even more complicated due to the off-shellness of the incoming photon. As a consequence, the EM vertex involves not merely one, but two off-shell particles. Ref. [83] discusses the impact of off-shell effects on a variety of interaction Lagrangians.

Even when an appropriate form for the Lagrangians has been found, the values of the interaction parameters remain unknown. Contrary to the nonstrange sector, where the coupling constants can be determined from $NN/\pi N$ scattering and photoproduction, the photon-hyperon and hyperon-nucleon couplings are more difficult to access. They can either be calculated from quark models or determined through a fit to experiment. The fitting procedure followed in this work is sketched in Appendix B.1.

**Form factors.** Hadrons are not pointlike, but have an internal structure. As a consequence, they manifest themselves differently according to the resolution at which they are probed. This can be formally expressed by modifying the effective coupling constants with appropriate *form factors*, i.e. scalar functions of a certain off-shell four-momentum which play the role of "running" coupling constants for the effective theory.

The *strong* or *hadronic* form factors are the running coupling constants at the hadronic vertices. The form most commonly assumed in literature is a dipole [84]

$$F_x = \frac{\Lambda_h^4}{\Lambda_h^4 + (x - m_h^2)^2}, \tag{2.50}$$

with $x$ the squared four-momentum of the intermediate hadron $h$, and $m_h$ its mass. The cutoff mass $\Lambda_h$ determines the high-energy (short-range) behavior of the interaction, which can either be hard ($\Lambda_h$ small) or soft ($\Lambda_h$ large). It can be used as a free parameter when optimizing the model parameters against the data. One usually assumes a single cutoff value $\Lambda_{res}$ for all resonant diagrams, and another $\Lambda_{bg}$ for all background contributions.

The *electromagnetic* form factors depend on $Q^2 = -k^2$, with $k$ the incoming photon momentum. They are normalized so that they reduce to either 0 or 1 in the real-photon point. Their $Q^2$ evolution can be calculated in a quark model or, in some cases, be determined experimentally. For the sake of simplicity, many calculations assume a monopole form factor for mesons and a dipole for baryons. While this is generally considered to be a good approximation, recent quark-model calculations [83] predict considerable deviations from the dipole shape for a number of baryon resonances.

**Unitarity and the isobar model.** Since the unitarity requirement is linked to the conservation of probability, it is automatically fulfilled for the fundamental interactions. In the fundamental field theories, the decay widths of propagating particles are generated dynamically through a process known as the "dressing " of propagators. Effective field theories, on the other hand, are not necessarily unitary by construction. When restricting oneself to the tree-level diagrams, one is forced to plug the decay widths of the various resonances in by hand. This is accomplished through the substitution

$$s - m_R^2 \longrightarrow s - m_R^2 + i m_R \Gamma_R \tag{2.51}$$

in the propagator denominators, with $m_R$ and $\Gamma_R$ the mass and width of the propagating state ($R = N^*, \Delta^*$). This procedure is applied solely to the resonant diagrams, where the exchanged particle can be on shell in the physical region of the process.

### Higher-order corrections

It is obvious that the isobar approach has its limitations. Firstly, introducing decay widths to account for the resonances' finite lifetimes breaks unitarity for the total scattering amplitude. Secondly, by truncating the amplitude at tree level, higher-order mechanisms like channel couplings and final-state interactions are excluded from the reaction mechanism. The importance of this issue becomes clear when realizing that the $\pi N \rightarrow \pi N$ and $\gamma N \rightarrow \pi N$ cross sections are many times larger than the $\gamma p \rightarrow KY$ ones. In other words, contributions from higher-order processes such as the one shown in Fig. 2.4, are not necessarily less important than the tree-level diagrams.

Calculations by Chiang *et al.* [31] have shown that the contribution of the intermediate $\pi N$ channel to the $p(\gamma, K^+)\Lambda$ cross sections is of the order of 20%. This does not imply, though, that tree-level models are unsuitable to describe the KY production channels. The success of the isobar approach in describing even the most recent data (see for example Ref. [85]) demonstrates that lowest-order diagrams are well able to "mimic" certain higher-order effects. Caution is advised, however, when comparing the coupling constants found in the context of a tree-level model to calculated or measured values. The tree-level values should be regarded as "dressed" results, which effectively include higher-order effects like the one shown in the left-hand diagram of Fig. 2.4.

In recent years, steps have been taken to include higher-order corrections in the context of a "coupled-channels" (CC) framework. CC approaches aim at simultaneously describing a number of reaction channels, such as $\pi N$, $\gamma N$, $\pi\pi N$ and KY, in a consistent way [32–34, 44, 86]. Couplings between different channels and rescattering effects within each separate channel are explicitly taken into account. In addition, it is possible to impose the unitarity constraint, for example through the K-matrix formalism. If the scattering matrix T is assumed to have the form

$$T = \frac{K}{1 - iK}, \tag{2.52}$$

$S = 1 + 2iT$ is unitary provided that the kernel K is Hermitian. It should be noted that, while unitarity can be -artificially- ensured in such a model, no CC calculation can include *all* relevant reaction channels. Decay widths accounting for the missing channels are commonly introduced in the CC frameworks [32, 44].

In this work, channel-coupling effects are neglected. Admittedly, it is debatable whether the extraction of resonance information can be reliably performed at tree level. It should be stressed, however, that the current description of some channels, including

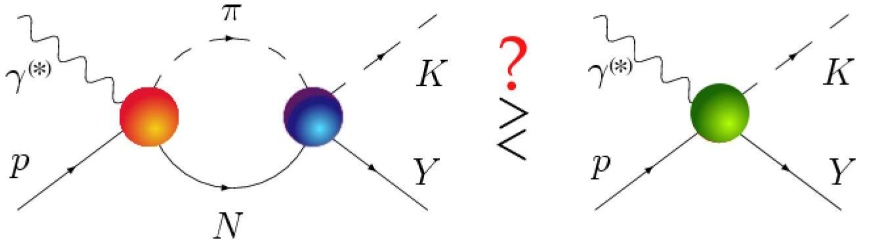

**Figure 2.4** A typical higher-order contribution to $p(\gamma^{(*)}, K)Y$ (left), as compared to the direct process (right).

the $p(\gamma^{(*)}K)Y$ ones, is plagued by severe uncertainties. The choice of gauge-restoration procedure [87–89] (see Sec. 2.3.3), for example, has recently been demonstrated to have a large impact on the computed observables [44]. Also, a fundamental understanding of the functional form of the hadronic form factors and the magnitude of the cutoff values is still lacking. Settling such issues in the context of a coupled-channels framework constitutes a gigantic task. We deem that these uncertainties can better be addressed at the level of the individual reaction channels, where the number of parameters and uncertainties can be kept at a manageable level. In addition, CC analyses face unresolved challenges, such as accounting for the $\pi\pi N$ channels, which are responsible for about half of the total $\gamma N$ cross section in the higher-mass $N^*$ region. Finally, while the extension from photo- to electroproduction is relatively straightforward in a tree-level model, to our knowledge no CC approach to kaon electroproduction has as yet been proposed.

### 2.3.2 Background contributions

The obvious challenge for effective-Lagrangian approaches lies in selecting those diagrams which dominate in the energy region under study. A central question is how to model the background part of the amplitude. The $p(\gamma^{(*)}, K)Y$ processes receive large background contributions, in contrast to $\pi N$ photoproduction for example, which is strongly $s$-channel dominated in the near-threshold regime. Because the background diagrams are not restricted to a particular partial wave, their parameterization affects the extracted properties of all contributing resonances. Thus, constructing an appropriate background model is a vital step in extracting reliable resonance information from the data.

In the absence of strong or EM form factors, the strong $g_{KYp}$ couplings constitute the sole unknown ingredients of the Born-term part of the amplitude. As demonstrated in Refs. [90,91], SU(3)-flavor symmetry allows to relate the various $g_{KYp}$ couplings to their nonstrange counterparts $g_{\pi NN}$, which are well-known from NN and $\pi N$ scattering. When assuming a maximum deviation of 20% from the exact $SU(3)_f$ value, the following ranges emerge:

$$-4.5 \leq \frac{g_{K\Lambda p}}{\sqrt{4\pi}} \leq -3.0\,, \tag{2.53}$$

$$0.9 \leq \frac{g_{K^+\Sigma^0 p}}{\sqrt{4\pi}} \leq 1.3\,, \tag{2.54}$$

and $g_{K^0\Sigma^+p} = \sqrt{2}g_{K^+\Sigma^0 p}$ as explained in Appendix A.3. Figure 2.5 shows that, when no hadronic form factors are present, imposing the limits of Eqs. (2.53) and (2.54) results

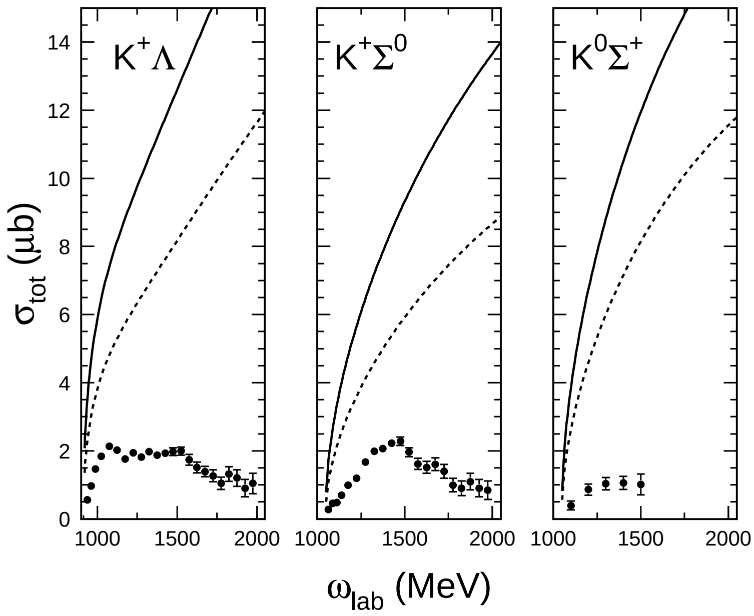

**Figure 2.5** Total cross section for the three $p(\gamma, K)Y$ channels, as computed in an isobar model consisting solely of Born-term contributions, unmodified by hadronic form factors. The solid curves represent the result obtained with the exact $SU(3)_f$ prediction for $g_{KYp}$, whereas the dashed curves correspond to the lower limits of Eqs. (2.53)-(2.54). The figure was taken from Ref. [71]. The data are from [55,56].

in a Born contribution which spectacularly overshoots the measured cross sections. Any reasonable background parameterization should therefore contain an appropriate mechanism to reduce the Born-term strength. Roughly speaking, three different strategies may be followed in realizing such a reduction. We refer to them as background models A, B and C, in accordance with Ref. [71]:

- Model A assumes hadronic form factors with a very small cutoff $\Lambda_{bg}$. When respecting the $SU(3)_f$ constraints for $g_{KYp}$, values of $\Lambda_{bg}$ as small as 0.4 GeV are required in Eq. (2.50) in order to make the calculations reproduce the data.

- Model B introduces hyperon resonances in the $u$ channel. It has been shown that these can strongly reduce the cross sections through destructive interference with the Born terms. Eqs. (2.53)-(2.54) can then be fulfilled, while still assuming realistic values for the strong form-factor cutoff ($\Lambda_{bg} \gtrsim 1.5$ GeV).

- Model C consists of simply discarding the $SU(3)_f$ constraints for the strong Born couplings. With $\Lambda_{bg}$ of the order of 1.1 GeV, a proper fit of the data requires values for $g_{KYp}$ which are about 25% of the $SU(3)_f$ predictions.

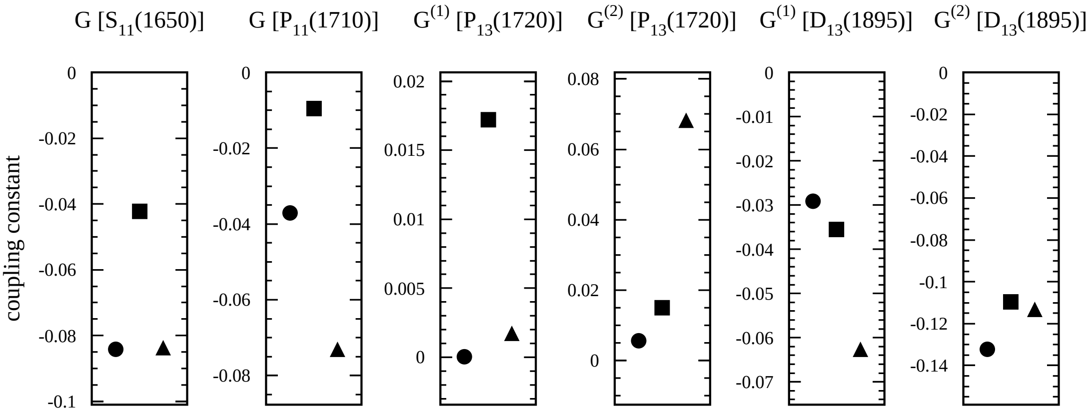

**Figure 2.6** Sensitivity of extracted $N^*$ coupling constants, derived from a fit to the data of Ref. [55], to the chosen background parameterization A (•), B (■) or C (▲). The figure was taken from Ref. [23].

Though all of these strategies allow for a reasonable description of the data, the extracted resonance couplings depend heavily on the employed parameterization [23,92, 93]. This is shown explicitly in Fig. 2.6, which compares the $N^*$ coupling constants extracted from the $p(\gamma, K^+)\Lambda$ data of Ref. [55] using background models A, B and C. It is clear that this issue needs to be resolved before a reliable extraction of resonance information can be attempted.

### 2.3.3 Gauge-invariance restoration

An essential property of any theory dealing with electromagnetic interactions is *gauge invariance*, related by the Noether theorem [94] to the principle of charge conservation. In a Lagrangian framework, the gauge-invariance requirement can be cast into a useful mathematical form. For any process involving a real or virtual photon, characterized by a four-momentum $k$ and polarization four-vector $\varepsilon$, the total reaction amplitude can be written as $\mathcal{M} = \varepsilon_\mu \mathcal{M}^\mu$. Gauge invariance is then ensured when the *Lorentz condition* is fulfilled:

$$k_\mu M^\mu = 0\,, \tag{2.55}$$

representing the conservation of the electromagnetic current $M^\mu$.

### $KY$ photoproduction

The $p(\gamma,K)Y$ interaction Lagrangians are constructed in such a manner that the total amplitude is gauge invariant in the absence of hadronic form factors. With the Lagrangians from Appendix A.1, it can easily be proven that each individual diagram with an inelastic EM transition vertex respects gauge invariance. For the Born diagrams, however, the EM current contains a so-called *electric* term, proportional to $\gamma^{\mu}\varepsilon_{\mu}$. This prevents the Lorentz condition from being obeyed for each diagram separately. In $K^+$ photoproduction, both the $s$- and $t$-channel Born amplitudes involve an electric coupling:

$$\varepsilon_{\mu}M^{\mu}_{s-\text{electric}} = \varepsilon_{\mu}\, e g_{K^+Yp}\, \overline{u}_Y \gamma_5 \frac{\not{p} + \not{k} + m_p}{s - m_p^2} \gamma^{\mu} u_p \,, \tag{2.56}$$

$$\varepsilon_{\mu}M^{\mu}_{t} = \varepsilon_{\mu}\, e g_{K^+Yp}\, \overline{u}_Y \frac{2p_K^{\mu} - k^{\mu}}{t - m_K^2} \gamma_5 u_p \,. \tag{2.57}$$

Here, $p$, $k$ and $p_K$ represent the four-momenta of the proton, photon and kaon, whereas $u_p$ and $u_Y$ are the proton and hyperon spinors. The $s$- and $u$-channel Born terms also contain a *magnetic* contribution, proportional to $\sigma_{\mu\nu}F^{\mu\nu}$, which is gauge invariant by construction. Depending on the isospin channels, the electric contributions can occur in different Born amplitudes. In the $n(\gamma,K^+)\Sigma^-$ case, for example, electric couplings emerge in the $t$ and $u$ channels. While the currents in Eqs. (2.56) and (2.57) are not individually gauge invariant, it is straightforward to show that their *sum* $M^{\mu}_{s-\text{electric}} + M^{\mu}_{t}$ vanishes in contraction with $k_{\mu}$. Clearly, this condition is no longer met when the amplitudes are modified by different hadronic form factors.

As suggested by Haberzettl [88], gauge invariance for the Born diagrams can be restored by adding a number of well-chosen *contact terms*, i.e. diagrams which do not contain any poles. It turns out that adding a contribution of the form

$$\begin{aligned}\varepsilon_{\mu}M^{\mu}_{\text{contact}} = {} & \varepsilon_{\mu}\, e g_{K^+\Lambda p}\, \overline{u}_{\Lambda} \gamma_5 \left[ \frac{2p^{\mu} + \not{k}\gamma^{\mu}}{s - m_p^2} \left(\widehat{F} - F_s\right) \right. \\ & \left. + \frac{2p_K^{\mu}}{t - m_K^2} \left(\widehat{F} - F_t\right) \right] u_p \end{aligned} \tag{2.58}$$

results in an exact cancellation of the gauge-violating terms. It can be seen that the recipe of Eq. (2.58) amounts to replacing the strong form factors of all electric terms with an identical, new form factor $\widehat{F}$.

With regard to the functional form of $\widehat{F}$, many suggestions have been made. Haberzettl proposed a linear combination [88]

$$\widehat{F} = \widehat{F}_H \equiv a_s F_s(\Lambda) + a_t F_t(\Lambda) + a_u F_u(\Lambda) \,, \tag{2.59}$$

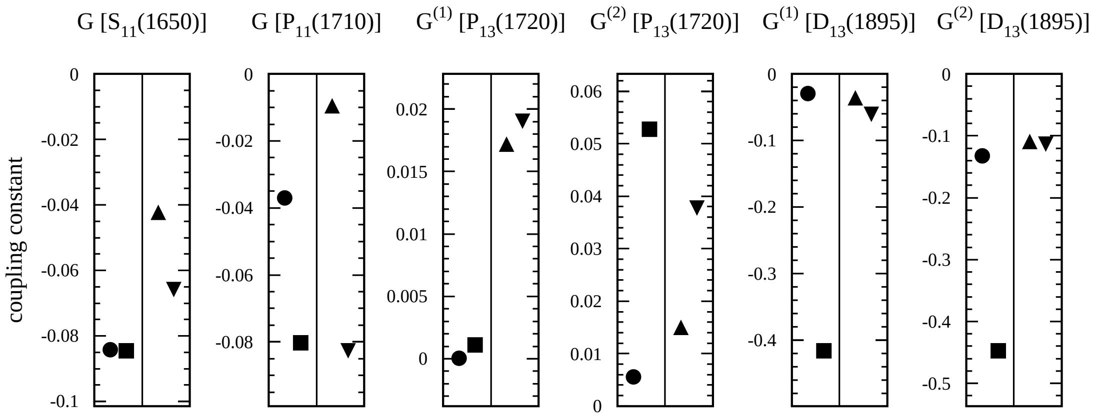

**Figure 2.7** Sensitivity of extracted $N^*$ coupling constants to the functional form of the hadronic form factor $\widehat{F}$. The left-hand (right-hand) side of the panels corresponds to a fit using background model A (B) to the data of Ref. [55]. The circles • and triangles ▲ represent a calculation with the Davidson-Workman recipe $\widehat{F}_{DW}$, whereas the squares ■ and triangles ▼ were obtained using the Haberzettl form $\widehat{F}_H$. The figure was taken from [23].

with the coefficients satisfying the relation $a_s + a_t + a_u = 1$. This prescription was criticized by Davidson and Workman [89] who pointed out that, with the $\widehat{F}_H$ of Eq. (2.59), Eq. (2.58) contains singularities and can therefore not be considered as a contact term. They argue that $\widehat{F}$ has to obey the following minimal set of conditions:

$$\widehat{F}(s = m_p^2) \quad = F_s \ , \tag{2.60}$$

$$\widehat{F}(t = m_K^2) \quad = F_t \ . \tag{2.61}$$

A solution is provided by the following recipe for $\widehat{F}$:

$$\widehat{F} = \widehat{F}_{DW} \equiv F_s\,(\Lambda) + F_t\,(\Lambda) - F_s\,(\Lambda)\,F_t\,(\Lambda) \ . \tag{2.62}$$

Figure 2.7 shows the sensitivity of a number of $N^*$ coupling constants to the adopted functional form for $\widehat{F}$. The different values were obtained through a series of fits to the $p(\gamma, K^+)\Lambda$ SAPHIR data of Ref. [55], using background models A and B (see Sec. 2.3.2 and Ref. [23]) in combination with the Haberzettl ($\widehat{F}_H$, Eq. (2.59)) and Davidson-Workman ($\widehat{F}_{DW}$, Eq. (2.62)) prescriptions for $\widehat{F}$. It is clear that the extracted resonance information is strongly affected by the choice of gauge-restoration recipe [23,26,44].

### $KY$ electroproduction: the Gross-Riska procedure

While the Haberzettl and Davidson-Workman prescriptions successfully restore gauge invariance at the real-photon point, the emergence of EM form factors at finite $Q^2$ spoils this situation. In the $p(e, e'K^+)Y$ case, the EM Lagrangians for the $s$- and $t$-channel Born amplitudes are given by:

$$
\begin{aligned}
\mathcal{L}_{\gamma^* pp} &= -e\, F_1^p\left(Q^2\right) \overline{N} \gamma_\mu N\, A^\mu + \frac{e\kappa_p}{4m_p}\, F_2^p\left(Q^2\right)\, \overline{N}\, \sigma_{\mu\nu} N\, F^{\mu\nu}\,, && (2.63)\\
\mathcal{L}_{\gamma^* KK} &= -ie\, F_K\left(Q^2\right) \left(K^\dagger \partial_\mu K - K \partial_\mu K^\dagger\right) A^\mu\,, && (2.64)
\end{aligned}
$$

whereas the $\gamma^* YY$ interaction acquires an electric coupling

$$
\mathcal{L}_{\gamma^* YY} = -e\, F_1^Y\left(Q^2\right) \overline{Y} \gamma_\mu Y\, A^\mu + \frac{e\kappa_Y}{4m_p}\, F_2^Y\left(Q^2\right) \overline{Y}\, \sigma_{\mu\nu} Y\, F^{\mu\nu}\,, \qquad (2.65)
$$

with $F_1^Y(0) = 0$. It is obvious that, with those modifications, the gauge invariance of the combined electric terms is lost.

To remedy this situation, Gross and Riska [95] suggested the following replacements in the vertex functions:

$$
\begin{aligned}
\mathcal{M}^\mu_{s,u-\text{electric}} \sim F_1^{p,Y}\left(Q^2\right) \gamma_\mu \quad &\longrightarrow \quad F_1^{p,Y}\left(Q^2\right) \left[\gamma_\mu + \frac{\not{k}}{Q^2}\, k_\mu\right] \\
&\qquad - F_1^{p,Y}(0)\, \frac{\not{k}}{Q^2}\, k_\mu\,, && (2.66)\\
\mathcal{M}^\mu_t \sim F_K\left(Q^2\right) \left(2p_K - k\right)_\mu \quad &\longrightarrow \quad F_K\left(Q^2\right) \left[\left(2p_K - k\right)_\mu + \frac{\left(2p_K - k\right)\cdot k}{Q^2}\, k_\mu\right] \\
&\qquad - F_K(0) \left[\frac{\left(2p_K - k\right)\cdot k}{Q^2}\, k_\mu\right]\,. && (2.67)
\end{aligned}
$$

Using the above prescription, it is straightforward to show that the Lorentz condition for the total amplitude (Eq. (2.55)) is obeyed at any $Q^2$, provided that it is obeyed at $Q^2 = 0$. In other words, if the EM current is conserved in the real-photon point, the procedure of Gross and Riska allows to construct a gauge-invariant model for the virtual-photon process. We point out that the extra terms introduced in Eqs. (2.66) and (2.67) do not contribute to the observable quantities. They are proportional to the photon four-momentum $k^\mu$ which, in the Lorentz gauge assumed in this work, vanishes in contraction with $\varepsilon_\mu$.

For additional details regarding the isobar model, we refer the reader to the work of Janssen [71]. The remainder of this chapter focuses on the central subject of this thesis, i.e. the construction of an alternative effective-field model, avoiding the ambiguities of the isobar approach concerning form-factor and gauge-restoration prescriptions. In the following chapters, it will be shown that Regge phenomenology provides an elegant solution to this problem.

## 2.4 Beyond the resonance region: the Regge model

A major shortcoming of the isobar approach introduced in Sec. 2.3 is its limited scope in energy. Specifically, isobar models fail to meet a necessary condition for unitarity, known as the *Froissart bound*, which constitutes an upper limit on the high-energy behavior of the cross sections [96]. A realistic total scattering cross section is allowed to increase with energy no faster than $\log^2\left(\frac{s}{s_0}\right)$. In an isobar framework, however, the background contribution rises as a positive power of $s$. This is illustrated for example by Fig. 2.5 from the previous section. Up to a certain energy, this rise can be compensated by destructive interferences with resonant diagrams. For COM energies higher than a few GeV, where adding individual resonances no longer makes sense, unphysical behavior develops.

A solution is provided by a high-energy framework introduced by Regge in 1959 [36]. Originally conceived as an alternative approach to quantum-mechanical potential scattering, this approach distinguishes itself through its elegant treatment of high-spin, high-mass particle exchange. Regge's starting-point was to consider the partial-wave amplitudes as a function of a *complex* angular momentum variable. Interestingly, poles of the amplitude were found to correspond to resonant states, which could be classified into a number of families. The members of such a family, or *Regge trajectory*, turned out to share identical internal quantum numbers, such as strangeness and isospin, while having different total spins. Rather than focusing on the exchange of individual hadrons, Regge theory considers entire trajectories as intermediate states.

Since its initial formulation, the Regge approach has been extended far beyond its original scope. It gained momentum in the sixties and early seventies [97–100], when it was first applied to hadronic scattering processes and meson-production reactions at high energies. In the late nineties, it received renewed attention with the development of a Regge-based effective-Lagrangian model for EM $\pi$ and $K$ production [37–39, 101, 102] by Guidal, Laget and Vanderhaeghen. More recently, several alternative implementations of Regge phenomenology have been proposed, such as the reggeized unitary isobar model [103, 104] and the quark-gluon string model [105].

In this section, we will take the high-energy Guidal-Laget-Vanderhaeghen (GLV) approach as a starting point to construct a $p(\gamma^{(*)}, K)Y$ reaction model valid both in and above the resonance region. As the GLV model consists exclusively of background diagrams, it cannot be expected to account for all aspects of the reaction dynamics at lower energies. We will show that this can be remedied by superimposing a number of s-channel ($N^*$ and/or $\Delta^*$) resonance contributions onto the GLV amplitude. A similar "Regge-plus-resonance" (RPR) strategy was successfully applied to high-energy double-pion production in Ref. [42], and to the production of $\eta$ and $\eta'$ mesons in Ref. [43].

### 2.4.1 Regge theory and complex angular momenta

A "Regge trajectory" refers to a class of particles with the same internal quantum numbers, but different masses and angular momenta. How these trajectories emerge as formal objects in the Regge framework is considerably more complex. Here, we will sketch the main ideas behind Regge theory and focus on its application to the $p(\gamma^{(*)}, K)Y$ processes. For an in-depth discussion we refer to the works of Collins [106] and Donnachie [107], as well as to Refs. [108–110].

A central concept behind the Regge formalism is the principle of *crossing symmetry*. The amplitude for any process involving a particle X with momentum $p$ in the initial state equals the amplitude for an otherwise identical process but having an antiparticle $\overline{X}$ with momentum $p' = -p$ in the final state:

$$\mathcal{M}\big(X(p) + \cdots \longrightarrow \cdots\big) = \mathcal{M}\big(\cdots \longrightarrow \overline{X}(p' = -p) + \cdots\big) \tag{2.68}$$

As mentioned in Sec. 2.3, the reaction amplitude for a two-particle scattering process $1 + 2 \to 3 + 4$ is a function of two independent kinematical quantities. These can for example be chosen as $(s, t)$ or $(s, u)$, with $s = (p_1+p_2)^2$, $t = (p_1-p_3)^2$ and $u = (p_1-p_4)^2$ the usual Mandelstam variables. Crossing symmetry implies that the crossed t- and u-channel reactions $1+\overline{3} \to \overline{2}+4$ and $1+\overline{4} \to \overline{2}+3$ are described by the same function $\mathcal{M}$ as the direct s-channel process, albeit with different values of the variables. Specifically, if $\mathcal{M}_s$, $\mathcal{M}_t$ and $\mathcal{M}_u$ represent the amplitudes for the direct and crossed reactions, the equality

$$\mathcal{M}_s(p_1, p_2, p_3, p_4) = \mathcal{M}_t(p_1, -p_3, -p_2, p_4) = \mathcal{M}_u(p_1, -p_4, p_3, -p_2) \tag{2.69}$$

is guaranteed. In terms of the Mandelstam variables, this becomes:

$$\mathcal{M}_s(s, t, u) \equiv \mathcal{M}_t(t, s, u) \equiv \mathcal{M}_u(u, t, s)\,. \tag{2.70}$$

Eqs. (2.69)-(2.70) can be best understood on a diagram-by-diagram basis, as shown in Fig. 2.8. It is clear that an incoming particle should be replaced by an outgoing

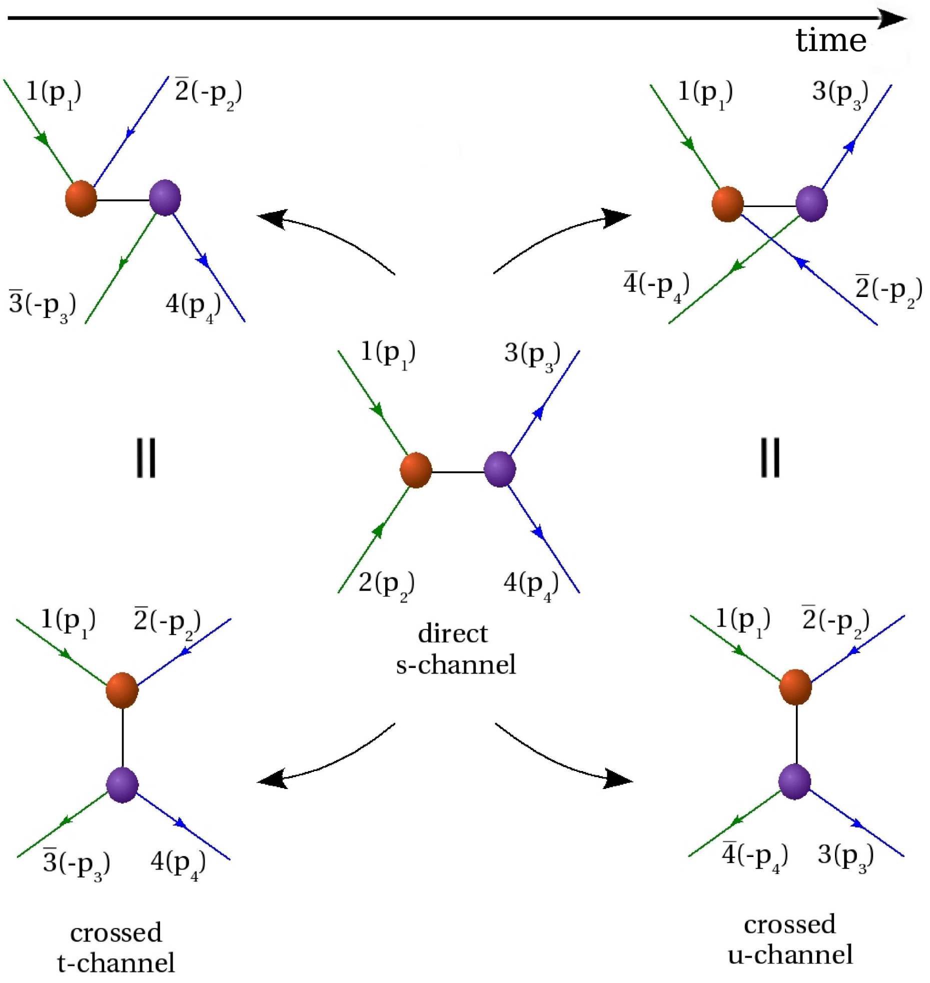

**Figure 2.8** Illustration of crossing symmetry at the Feynman-diagram level. The green (blue) lines correspond to incoming (outgoing) external particles. By deforming the Feynman diagram for the process $1 + 2 \to 3 + 4$ (center), diagrams for the two crossed reactions may be obtained. It can easily be seen that an s-channel diagram in the amplitude for the direct process becomes a t−channel (u-channel) diagram in the crossed reaction $1+\bar{3} \to \bar{2}+4$ ($1+\bar{4} \to \bar{2}+3$).

antiparticle with the opposite momentum, and vice versa, in order for the total lepton number and four-momentum to be conserved.

A useful application of crossing symmetry is that it allows one to obtain the amplitude of the direct $s$-channel process from that of the crossed $t$ or $u$ channel, by means of analytic continuation. While this might seem like an unnecessary detour, it turns out to lead to a very useful formulation of the direct amplitude. The best starting point is to expand the crossed $t$- or $u$-channel amplitude into a Legendre series. For the reaction

$1 + \overline{3} \to \overline{2} + 4$, such a decomposition takes the form:

$$\mathcal{M}_t(t,s) \;=\; \sum_{l=0}^{\infty}(2l+1)\mathcal{M}_l(t)\mathcal{P}_l(\cos\theta_t) \;=\; \mathcal{M}_s(s,t)\,, \tag{2.71}$$

with $\theta_t$ the t-channel scattering angle, i.e. the angle between $\vec{p}_1$ and $-\vec{p}_2$. In the simplified case of spinless external particles, $l$ can be identified with the spin of a resonant state formed in the crossed reaction, $t$ being its squared four-momentum. Unfortunately, Eq. (2.71) does not converge in the physical region of the direct process [111, 112], and is therefore not suitable for analytic continuation. It may, however, be cast into a more practical form by re-writing the sum over $l$ as a contour integral in the complex angular momentum, or $\lambda$, plane. Solving this integral requires a number of assumptions concerning the analytical structure of the partial-wave amplitude $\mathcal{M}_\lambda(t)$. Regge postulated that the only singularities of this amplitude in the complex $\lambda$ plane are poles, located at $\lambda = \alpha_i(t)$. The situation $\alpha_i(t) = n$, with $n$ a positive integer value, corresponds to the creation of a physical particle or resonance with mass $m = \sqrt{t}$ and spin $n$. Precisely these functions $\alpha_i(t)$, or equivalently, the sets of resonances that are their physical manifestations, are known under the name of "Regge trajectories".

A closed expression for the partial-wave decomposition (2.71) can be obtained in the limit of very high energies $W = \sqrt{s}$ and for small values of $t$. The resulting amplitude $M_s(s,t)$ for the direct reaction can be interpreted as corresponding to the exchange of one or several Regge trajectories in the $t$ channel, and is valid for extreme forward kaon angles ($\theta_K^* \approx 0$). Analogously, when taking the crossed $u$-channel process as a starting point, the result for $M_s(s,u)$ is valid at high $s$ and small $u$, i.e. in the extreme backward-angle ($\theta_K^* \approx 180°$) regime, and involves trajectories exchanged in the $u$ channel of the direct process. The amplitudes obtained in this manner obey the Froissart bound.

We wish to stress that the assumption of Regge poles as the sole singularities of the scattering amplitude cannot be formally proven. In fact, it has been known for some time that cuts in the complex $\lambda$ plane are required to explain some features of, for example, the $np \to pn$ scattering process [113]. Still, the success of Regge-pole models in describing a variety of hadronic reactions, including the EM production of kaons, provides ample justification for adopting the Regge-pole assumption.

### 2.4.2 Amplitudes and propagators in the Regge limit

The focus of this work is on the forward-angle kinematical region which, for electromagnetic KY production, implies the exchange of kaonic Regge trajectories in the $t$ channel. Empirically, it is observed that the functions $\alpha(t)$ relating the spins and

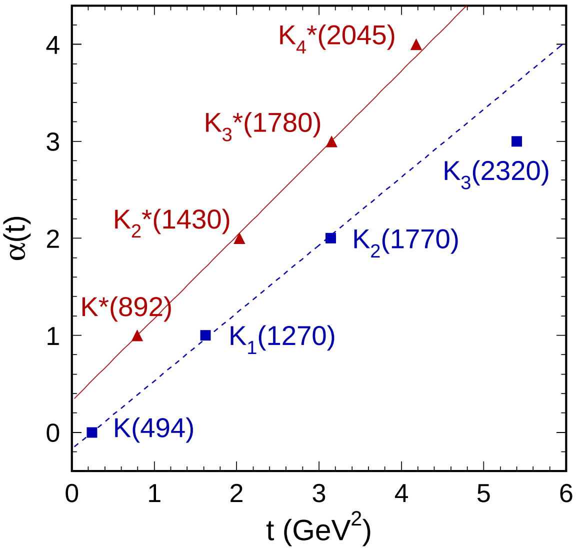

**Figure 2.9** Chew-Frautschi plots for the $K(494)$ and $K^*(892)$ trajectories. The meson masses are from the Particle Data Group [114].

squared masses of the hadronic trajectory members are linear to a very good approximation. Figure 2.9 illustrates this point by showing the $J$ versus $m^2$ plots (Chew-Frautschi plots) for the trajectories with $K(494)$ and $K^*(892)$ as lightest members, or "first materializations".

Since we aim at developing a consistent description of the $p(\gamma^{(*)}, K)Y$ observables in and above the resonance region, we opt to embed the Regge formalism into a tree-level effective-Lagrangian model [115]. This approach was used by Guidal, Laget and Vanderhaeghen in their treatment of high-energy electromagnetic $\pi$ and $K$ production [37, 38, 102]. In such a framework, it turns out that the amplitude for t-channel exchange of a linear kaon trajectory

$$\alpha_X(t) = \alpha_{X,0} + \alpha'_X\,(t - m_X^2)\,, \tag{2.72}$$

with $m_X$ and $\alpha_{X,0}$ the mass and spin of the trajectory's first materialization $X$, can be obtained from the standard Feynman amplitude by replacing the denominator of the Feynman propagator with a Regge propagator:

$$\frac{1}{t - m_X^2} \quad\longrightarrow\quad \mathcal{P}^X_{\text{Regge}}[s, \alpha_X(t)]\,. \tag{2.73}$$

A closed form can be derived for $\mathcal{P}^X_{\text{Regge}}$, starting from the t-channel Regge amplitude for the simplified case of spinless external particles. In the Regge limit of high $s$

and low $|t|$, this amplitude can be written as

$$\begin{aligned}\mathcal{M}^{\zeta=\pm}_{\text{Regge}}(s,t) &= C\left(\frac{s}{s_0}\right)^{\alpha^{\zeta}(t)} \frac{\beta^{\zeta}(t)}{\sin\big(\pi\alpha^{\zeta}(t)\big)} \\ &\quad\times \frac{1+\zeta\, e^{-i\pi\alpha^{\zeta}(t)}}{2} \frac{1}{\Gamma\big(1+\alpha^{\zeta}(t)\big)}\,,\end{aligned} \tag{2.74}$$

with $s_0$ a scale factor, fixed at 1 GeV$^2$, C an unknown constant, and $\beta^{\zeta}(t)$ a yet to be determined function of t. A detailed derivation of Eq. (2.74) can be found in various sources [71,102,106,107]. A brief overview is also given in Appendix C.

The above equation in fact represents two separate Regge amplitudes, labeled by a signature $\zeta = \pm 1$. This is because, in solving the complex-$\lambda$ integrals leading to Eq. (2.74), one has to distinguish between the two signature parts $\alpha^+(t)$ and $\alpha^-(t)$ of the trajectory in order to satisfy the convergence criteria. It can be seen that $\mathcal{M}^{\zeta=\pm}_{\text{Regge}}$ has poles at values of t where $\alpha^{\zeta}(t)$ assumes a non-negative even ($\zeta = +$) or odd ($\zeta = -$) integer value. These values are precisely the spins of the particles lying on the $\alpha^{\pm}(t)$ Regge trajectories, with the corresponding values of t equaling the particles' squared masses. Thus, the $\zeta = +$ trajectory connects particles with $J = 0, 2, 4$ etc., and is of the form

$$\alpha^+(t) = \alpha'^{+}(t - m_0^2)\,, \tag{2.75}$$

with $m_0$ the mass of the spin-0 first materialization. Similarly, the negative-signature trajectory can be written as $\alpha^-(t) = 1 + \alpha'^{-}(t - m_1^2)$.

The unknown ingredients C and $\beta^{\zeta}(t)$ can be determined by linking the $\gamma^{(*)}p \longrightarrow KY$ amplitude to the amplitude of the crossed t-channel process $\gamma^{(*)}\overline{K} \longrightarrow \overline{p}Y$. As explained in Sec. 2.4.1, crossing symmetry implies that both processes can be described by the same function $\mathcal{M}$ in the complex $(s,t)$ plane, albeit with the two Mandelstam variables s and t interchanged. Regge phenomenology exploits this symmetry by analytically continuing the reaction amplitude from the t-channel physical region into the s-channel physical region. In the vicinity of a t-channel pole $m_i^2$, the amplitude for the crossed process reduces to

$$\mathcal{M}^{\gamma\overline{K}\to\overline{p}\Lambda}_{\text{Feyn}}(t,s) \quad \xrightarrow{t=m_i^2} \quad \frac{\beta_i(t)}{t-m_i^2}\,. \tag{2.76}$$

We now demand that the crossed amplitude, when evaluated at its t-channel pole closest to the $\gamma^{(*)}p \longrightarrow KY$ physical region (where $t < 0$), equals the Regge amplitude (2.74). Thus, for the $\zeta = +$ case, we have the requirement

$$\mathcal{M}^{\gamma^{(*)}p\to KY,\,\zeta=+}_{\text{Regge}}(s,t) \quad \overset{t=m_0^2}{=} \quad \mathcal{M}^{\gamma^{(*)}\overline{K}\to\overline{p}Y}_{\text{Feyn}}(t,s) = \frac{\beta_0(t)}{t-m_0^2}\,. \tag{2.77}$$

If $\beta^{\zeta=+}(t)$ is taken to be equal to the residue $\beta_0(t)$ of the crossed Feynman amplitude, Eq. (2.77) leads to $C = \pi\alpha^{+\prime}$. If we now define

$$\mathcal{M}^{\zeta}_{\text{Regge}}(s,t) = \mathcal{P}^{\zeta}_{\text{Regge}}(s,t) \times \beta^{\zeta}(t)\,, \tag{2.78}$$

we finally obtain for the Regge propagator:

$$\mathcal{P}^{\zeta=\pm}_{\text{Regge}} = \frac{\left(\frac{s}{s_0}\right)^{\alpha^{\zeta}(t)}}{\sin\bigl(\pi\alpha^{\zeta}(t)\bigr)} \, \frac{1+\zeta\, e^{-i\pi\alpha^{\zeta}(t)}}{2} \, \frac{\pi\alpha'^{\zeta}}{\Gamma\bigl(1+\alpha^{\zeta}(t)\bigr)}\,. \tag{2.79}$$

While the theoretical derivation of the Regge amplitude (2.74) requires a separate treatment of positive and negative signatures, in practice it is often unnecessary to make this distinction. For many mesonic trajectories, the $\zeta = \pm$ parts approximately coincide (Fig. 2.9). In that case, it can usually be assumed that the positive- and negative-signature amplitudes have identical residues $\beta^{\zeta}(t)$, up to an unknown sign; this is referred to as *strong* degeneracy. The $\zeta = \pm$ amplitudes can then be added so that a single propagator, incorporating the simultaneous exchange of both trajectory parts, is obtained. The phase of this propagator can either be constant (1) or rotating ($e^{-i\pi\alpha(t)}$), depending on the relative sign between the residues of the individual signature parts:

$$\mathcal{P}_{\text{Regge}} = \frac{\left(\frac{s}{s_0}\right)^{\alpha(t)}}{\sin\bigl(\pi\alpha(t)\bigr)} \left\{ \begin{array}{c} 1 \\ e^{-i\pi\alpha(t)} \end{array} \right\} \frac{\pi\alpha'}{\Gamma\bigl(1+\alpha(t)\bigr)}\,. \tag{2.80}$$

It is clear that Eq. (2.80) has poles at nonnegative integer values of $\alpha(t)$, corresponding to the zeroes of $\sin\bigl(\pi\alpha(t)\bigr)$ which are not compensated by the poles of $\Gamma\bigl(1+\alpha(t)\bigr)$. Hence the interpretation that the Regge propagator effectively incorporates the exchange of all members of the $\alpha(t)$ trajectory. It is worth noting that in the physical plane of the processes under study (with $t < 0$), these poles cannot be reached.

Whether or not a trajectory should be treated as degenerate depends less on the trajectory equations themselves than on the process under study. Non-degenerate trajectories give rise to dips in the differential cross section because they exhibit so-called *wrong-signature zeroes* [106]. These are zeroes of the Regge propagator corresponding to poles of the gamma function which are not removed by the sine function in the denominator. For example, for $\zeta = +$ the propagator (2.79) has wrong-signature zeroes at strictly negative, odd values of $\alpha(t)$. Vice versa, a smooth, structureless cross-section points to degenerate trajectories. At first thought, it can seem strange that a certain trajectory may need to be treated as degenerate in one hadronic process, but as non-degenerate in another. This apparent inconsistency is, however, easily explained when realizing that the determining factors for degeneracy are the residues of the positive- and negative-signature amplitudes, which obviously depend on the specific initial and final state.

Generalizing Eq. (2.80) to nonscalar particles is nontrivial [106]. We adopt a pragmatic approach, which consists of the following replacement in the spinless-particle propagator of Eq. (2.80):

$$\alpha_X(t) \longrightarrow \alpha_X(t) - \alpha_{X,0} \,. \tag{2.81}$$

With this recipe, it is guaranteed that the condition (2.77) is also fulfilled for trajectories with a nonscalar first materialization. The altered gamma function further ensures that the resulting propagator has the correct pole structure, with poles at integer $\alpha_X(t) \geq \alpha_{X,0}$. The general Regge propagator for degenerate trajectories then takes the form:

$$\mathcal{P}^X_{\text{Regge}}(s,t) = \frac{\left(\frac{s}{s_0}\right)^{\alpha_X(t)-\alpha_{X,0}}}{\sin\bigl(\pi(\alpha_X(t)-\alpha_{X,0})\bigr)} \left\{ \begin{array}{c} 1 \\ e^{-i\pi(\alpha_X(t)-\alpha_{X,0})} \end{array} \right\} \frac{\pi\alpha'_X}{\Gamma\bigl(1+\alpha_X(t)-\alpha_{X,0}\bigr)} \,. \tag{2.82}$$

The above prescription allows one to construct the high-energy amplitude by selecting the dominant Regge trajectories in the $t$ channel. It turns out that, for fixed $s$, $|\mathcal{P}^X_{\text{Regge}}(s, t = 0)|$ increases with decreasing $|\alpha_X(0) - \alpha_{X,0}| = \alpha'_X m^2_X$. Because all meson trajectories have approximately the same slope $\alpha'_X$, as a rule of thumb those with a low-mass first materialization are assumed to dominate. It should be kept in mind, though, that the coupling strengths contained in the residues $\beta_X(t)$ (Eq. (2.78)) also play a role.

### 2.4.3 The Regge-plus-resonance approach

As explained in Sec. 2.4.1, Regge theory is a high-energy approach by construction. Accordingly, the Regge amplitude based on the propagator of Eq. (2.82) should be interpreted as the asymptotic form of the full amplitude for $s \to \infty$, $|t| \to 0$. The experimental meson production cross sections appear to exhibit this “asymptotic” Regge behavior for photon energies down to about 4 GeV [37, 38, 41]. It is evident that a pure background description such as the Regge-pole model does not suffice to describe the reaction at energies closer to threshold. There exists, however, a theoretical connection between the high- and low-energy domain, which is related to the notion of *duality*. Simply put, the duality hypothesis states that, on average, the sum of all resonant contributions in the $s$ channel equals the sum of all Regge poles exchanged in the $t$ channel. In practice, it is of course impossible to take all $s$-channel diagrams explicitly into account. Hence, the standard procedure consists of identifying a small number of dominant resonances, and supplementing these with a phenomenological background.

In Refs. [39,40,59,102] it is demonstrated that, even with the asymptotic form of the propagators, the gross features of the forward-angle pion and kaon photo- and electroproduction observables in the resonance region are remarkably well reproduced in a pure t-channel Regge model. These results imply that at forward angles, the global features of the $p(\gamma, K)Y$ reaction in the resonance region can be reasonably well reproduced in terms of background diagrams. These considerations have prompted us to adopt the Regge description for the high-energy amplitude to also describe the *background* contribution in the resonance region.

The near-threshold cross sections exhibit structures, such as peaks at certain energies and sudden variations in the angular distributions, which may reflect the presence of individual resonances. These are incorporated into the RPR framework by supplementing the reggeized background with a number of resonant s-channel diagrams. We will describe these resonant contributions using standard Feynman propagators. As in the isobar approach, the resonances' finite lifetimes are taken into account through the substitution

$$s - m_R^2 \longrightarrow s - m_R^2 + i m_R \Gamma_R \tag{2.83}$$

in the propagator denominators ($R = N^*, \Delta^*$). In order to minimize the number of free parameters, we assume the PDG values [114] for the masses and widths of the known resonances. The strong and electromagnetic interaction Lagrangians for coupling to spin-1/2 and spin-3/2 resonances are given in Appendix A.1.

In conventional isobar models, the resonance contributions increase with energy. For our RPR approach to be meaningful, however, the resonance amplitudes should vanish at high values of $\omega_{lab}$. This is accomplished by including a phenomenological form factor $F(s)$ at the strong $KYR$ vertices. Instead of the standard dipole parameterization used in most isobar models (Eq. 2.50), we assume a Gaussian shape

$$F_{Gauss}(s) = \exp\left\{ -\frac{(s - m_R^2)^2}{\Lambda_{res}^4} \right\} , \tag{2.84}$$

with $\Lambda_{res}$ the cutoff value. Both forms are compared in Fig. 2.10. Our primary motivation for introducing Gaussian form factors is that they fall off much more sharply with energy than dipoles. Using Gaussian form factors, for $\omega_{lab} \gtrsim 4$ GeV the resonant contributions to the observables are quenched almost completely, even for cutoff values of 1600 MeV and larger. We found a comparable effect impossible to attain with a dipole, even using a cutoff mass as small as 800 MeV.

The RPR amplitude is shown schematically in Fig. 2.11. It involves t-channel exchanges of kaonic trajectories ($\mathcal{K}$) as well as s-channel Feynman diagrams corresponding to individual baryon resonances ($R$). In practice, the summations $\sum_{\mathcal{K}}$ and $\sum_R$ run

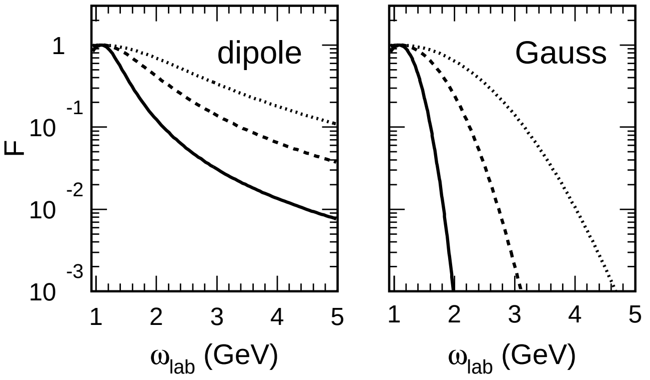

**Figure 2.10** Dipole and Gaussian form factors as a function of the photon lab energy $\omega_{lab}$, for a resonance with mass $m_{N^*} = 1710$ MeV. The full, dashed and dotted curves correspond to cutoffs $\Lambda_{res} = 800, 1200$ and $1600$ MeV respectively.

over a limited set of members of the kaon and nonstrange baryon spectra. Depending on the isospin channel, these sets may or may not include the ground-state $K$ and $p$, as will be explained in Secs. 3.1-3.2. By construction, the RPR amplitude is valid over the entire energy region described by the isobar and Regge models, i.e. from threshold up to about 20 GeV. In the high-energy regime ($\omega_{lab} \gtrsim 4$ GeV), all resonant contributions vanish by construction, so that only the Regge part of the amplitude remains.

The greatest asset of the RPR strategy, apart from its wide scope in energy, lies in the elegant description of the non-resonant part of the reaction amplitude. In standard isobar approaches, the determination of the background requires a significantly larger number of parameters. A typical isobar background amplitude consists of Born terms ($p$, $K$, $\Lambda$ and $\Sigma^0$ exchange) complemented by $K^*(892)$ and $K_1(1270)$ exchange diagrams. In some cases, $u$-channel hyperon resonances are introduced as well. A Regge-inspired model, on the other hand, is limited to $t$- *or* $u$-channel exchanges, with only a small number of trajectories required in either case. In addition, the serious

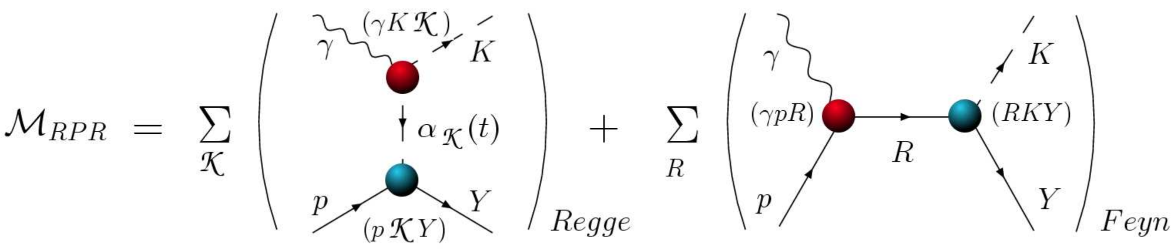

**Figure 2.11** General forward-angle RPR amplitude for the $\gamma p \to KY$ process.

issue of unreasonably large Born-term strength, which constitutes a major challenge for isobar models, does not arise in the RPR approach. Consequently, no strong form factors are required for the background terms and the introduction of an additional background cutoff parameter is avoided. The Regge model faces only one additional uncertainty, namely the choice between constant or rotating trajectories.

One issue which may cloud the presented procedure is double counting, caused by superimposing a (small) number of individual resonances onto the Regge background. Since the $\gamma p \to KY$ processes are largely background-dominated, the few $s$-channel terms may be considered as relatively minor corrections, and double counting is not expected to pose a very serious concern.

CHAPTER

# 3

# KY photoproduction in the Regge limit

As explained in Sec. 2.3, a major challenge for effective-field approaches to $p(\gamma^{(*)}, K)Y$ in the resonance region is modelling the background strength. In the standard isobar framework, the extracted resonance parameters are very sensitive to the choice made for the background parameterization [93]. The RPR approach provides a solution by offering an alternative method to constrain the background dynamics. As the resonant contributions to the RPR amplitudes vanish at high energies, one can distill the background coupling constants from the high-energy $p(\gamma, K)Y$ data. In a next step, these values can be used as input for calculations in the resonance region.

In this chapter, we will construct Regge amplitudes describing the $K^+\Lambda$, $K^+\Sigma^0$ and $K^0\Sigma^+$ photoproduction processes in the high-energy regime. The relevant background parameters in our model are products of a strong and an electromagnetic coupling constant. Through a fit to the available data for $\omega_{lab} \gtrsim 4$ GeV, optimum values for these parameters will be obtained. In our treatment of the various reaction channels, we will focus on the sensitivity of the calculated observables to the different model ingredients, including the choice of Regge-trajectory phases.

## 3.1 The $\gamma p \to K^+\Lambda$ channel

### 3.1.1 Forward-angle amplitude

We deliberately focus on t-channel reggeization. Our main motivation for this is the observation that most of the high-energy data correspond to forward-angle kinematics. The scarcity of the data for $\omega_{lab} \gtrsim 4$ GeV in the backward-angle regime makes it considerably more difficult to constrain the u-channel Regge amplitude. A second reason involves the fact that even the lightest hyperon, the $\Lambda$, is significantly heavier than a K meson. This implies that the u-channel poles are much further removed from the backward-angle kinematical regime than the t-channel poles are from the forward-angle region. Accordingly, for u-channel reggeization, the procedure of requiring the Regge propagator to reduce to the Feynman one at the closest crossed-channel pole is not guaranteed to lead to comparably good results.

#### $K^+$ and $K^{*+}(892)$ trajectories: $t$-channel contribution

We will rely on the t-channel Regge framework outlined in Sec. 2.4. Given the form of the Regge propagator (2.82), one expects the high-energy observables to be dominated by the Regge trajectories with the lowest-mass first materialization. In the kaon sector, $K(494)$ and $K^*(892)$ are by far the lightest states serving as first materializations. Since no obvious structure is present in the $p(\gamma, K^+)\Lambda$ cross-section data for $\omega_{lab} \gtrsim 4$ GeV [116], both the $K^+$ and $K^{*+}(892)$ trajectories will be assumed to be degenerate. As is clear from Fig. 2.9 (Sec. 2.4.2), this is certainly justified in the $K^*(892)$ case. Although the positive- and negative-signature parts of the K trajectory are not as perfectly collinear, it has been shown by Guidal and Vanderhaeghen that the assumption of degenerate trajectories is a valid one in the context of KY production [37,38,102]. Using the prescription of Eq. (2.82), the relevant Regge propagators for the $K^+\Lambda$ channel read:

$$\mathcal{P}^{K^+}_{Regge}(s,t) = \left(\frac{s}{s_0}\right)^{\alpha_{K^+}(t)} \frac{1}{\sin\big(\pi\alpha_{K^+}(t)\big)} \tag{3.1}$$

$$\times \left\{ \begin{array}{c} 1 \\ e^{-i\pi\alpha_{K^+}(t)} \end{array} \right\} \frac{\pi\alpha'_{K^+}}{\Gamma\big(1+\alpha_{K^+}(t)\big)}\,, \tag{3.2}$$

$$\mathcal{P}^{K^{*+}(892)}_{Regge}(s,t) = \left(\frac{s}{s_0}\right)^{\alpha_{K^{*+}(892)}(t)-1} \frac{1}{\sin\big(\pi(\alpha_{K^{*+}(892)}(t)-1)\big)} \tag{3.3}$$

$$\left\{ \begin{array}{c} 1 \\ e^{-i\pi(\alpha_{K^{*+}(892)}(t)-1)} \end{array} \right\} \frac{\pi\alpha'_{K^{*+}(892)}}{\Gamma\big(\alpha_{K^{*+}(892)}(t)\big)}\,, \tag{3.4}$$

with the trajectory equations given by [71]

$$\alpha_{K^+}(t) = 0.70\ \mathrm{GeV}^{-2}\ (t - m_{K^+}^2)\,, \tag{3.5}$$

$$\alpha_{K^{*+}(892)}(t) = 1 + 0.85\ \mathrm{GeV}^{-2}\ (t - m_{K^{*+}(892)}^2)\,. \tag{3.6}$$

**Restoring gauge invariance: $s$-channel contribution**

In Refs. [37, 38, 117] it is argued that apart from the $K^+$ and $K^{*+}(892)$ trajectory exchanges, the Regge amplitude for $K^+$ photoproduction should also include the *electric* contribution (defined in Appendix A.1 as the part proportional to $\gamma^\mu \varepsilon_\mu$) to the $s$-channel Born term. This can be accomplished through the recipe:

$$\begin{aligned}\mathcal{M}_{\mathrm{Regge}}(\gamma p \to K^+\Lambda) = \mathcal{M}_{\mathrm{Regge}}^{K^+} &+ \mathcal{M}_{\mathrm{Regge}}^{K^{*+}(892)} \\ &+ \mathcal{M}_{\mathrm{Feyn}}^{p,\mathrm{elec}} \times\ \mathcal{P}_{\mathrm{Regge}}^{K^+} \times\ (t - m_{K^+}^2)\,.\end{aligned} \tag{3.7}$$

Such a procedure is necessary because of the gauge-breaking nature of the $K^+$-exchange diagram. As explained in Sec. 2.3.3, in a typical effective-Lagrangian framework the Born terms $\mathcal{M}_{\mathrm{Feyn}}^{p,K,Y}$ in the $s$, $t$ and $u$ channels do not individually obey gauge invariance, but their sum does. Because the magnetic parts of the vertices ($\sim \sigma_{\mu\nu} q^\nu \varepsilon_\mu$) are gauge invariant by construction, only the electric parts are of concern. In Sec. 3.1.2, we will show that implementing this gauge-invariance restoration procedure leads to an improved description of the high-energy $p(\gamma, K^+)\Lambda$ differential cross section at $|t| \to 0$.

**Model parameters**

The diagrams contributing to high-energy, forward-angle $K^+\Lambda$ photoproduction are shown in Fig. 3.1. Without any exception, they are background terms, since none of them goes through a pole in the physical plane of the $p(\gamma, K^+)\Lambda$ process. Appendix A.1 summarizes the strong and electromagnetic interaction Lagrangians needed to calculate the Feynman residues $\beta_X(t)$ accompanying the Feynman propagators (Eq. (2.78)). Using these interactions, the $p(\gamma, K^+)\Lambda$ model contains only three parameters:

$$g_{K^+\Lambda p}\,, \quad G_{K^{*+}(892)}^{v,t} = \frac{e g_{K^{*+}(892)\Lambda p}^{v,t}}{4\pi}\ \kappa_{K^+ K^{*+}(892)}\,, \tag{3.8}$$

with $g_{K^{*+}(892)\Lambda p}^{v,t}$ the strong vector and tensor couplings to the $K^{*+}(892)$ vector-meson trajectory. These model parameters have to be optimized against the high-energy data of Refs. [116,118,119]. For $g_{K^+\Lambda p}$ we assume $SU(3)$-flavor symmetry, broken at the 20% level (see Sec. 2.3.2), which implies the constraint:

$$-4.5 \le \frac{g_{K^+\Lambda p}}{\sqrt{4\pi}} \le -3.0\,. \tag{3.9}$$

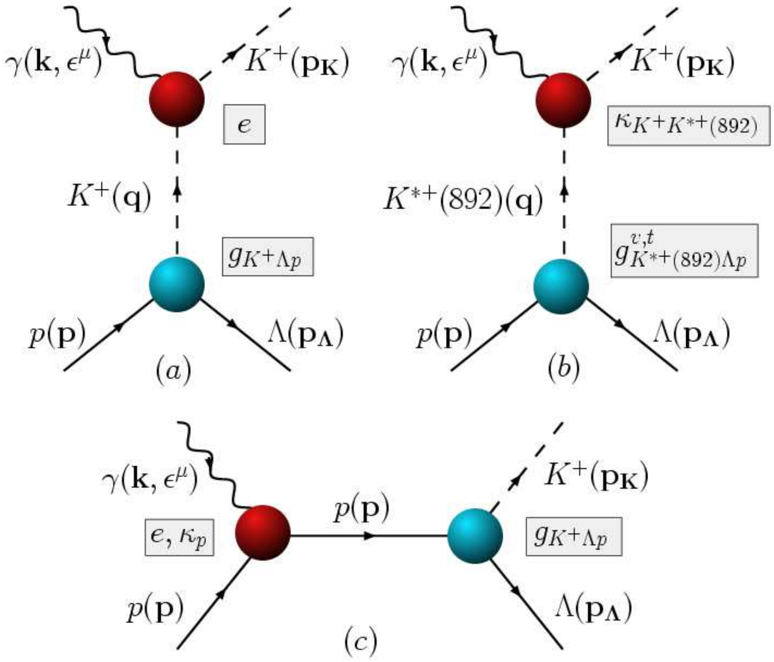

**Figure 3.1** Feynman diagrams contributing to the $p(\gamma, K^+)\Lambda$ amplitude for $\omega_{lab} \gtrsim 4$ GeV at forward angles: exchange of (a) $K^+$ and (b) $K^{*+}(892)$ trajectories. (c) The electric part of the s-channel Born term is added to restore gauge invariance.

The $G^{v,t}_{K^{*+}(892)}$ couplings are left entirely free.

Apart from the three parameters of Eq. (3.8), a choice between constant or rotating trajectory phases needs to be made. In our analysis, we consider three of the four possible phase combinations for the $K^+$ and $K^{*+}(892)$ Regge propagators: rotating K and $K^*$ phases, constant K plus rotating $K^*$ phase, and rotating K plus constant $K^*$ phase. The option with a constant phase for both propagators is not investigated because the corresponding Regge amplitude has no imaginary part. This would result in a vanishing recoil polarization, contradicting experiment [57].

### 3.1.2 Results and discussion

In contrast to the favorable experimental situation in the resonance region, the $p(\gamma, K^+)\Lambda$ data available for $\omega_{lab} \gtrsim 4$ GeV are rather scanty. The relevant low-$|t|$ data comprise 56 differential cross sections in total, at the selected energies $\omega_{lab} = 5$, 8, 11 and 16 GeV [116]. A limited number of polarization observables are available, in the form of 7 recoil and 9 photon beam asymmetry points at $\omega_{lab} = 5$ and 16 GeV respectively [118,119].

While the limited number of couplings contained in the Regge model is certainly an

| BG model | $K^+/K^{*+}(892)$ phase | $\frac{g_{K^+\Lambda p}}{\sqrt{4\pi}}$ | $G^v_{K^{*+}(892)}$ | $G^t_{K^{*+}}(892)$ | $\chi^2$ |
|---|---|---|---|---|---|
| 1 | rot. K, rot. $K^*$ | -3.23 | 0.281 | 1.09 | 3.17 |
| 2 | rot. K, rot. $K^*$ | -3.20 | 0.288 | -0.864 | 2.73 |
| 3 | rot. K, cst. $K^*$ | -3.00 | -0.189 | 1.17 | 4.37 |
| 4 | rot. K, cst. $K^*$ | -3.31 | -0.350 | -0.703 | 3.37 |

**Table 3.1** Comparison of the Regge background (BG) model variants (numbered 1 through 4) found to describe the high-energy, forward-angle $p(\gamma, K^+)\Lambda$ data [116, 118, 119]. The $K^+$ and $K^{*+}(892)$ trajectory phase options are given in the second column, while the last column shows the attained $\chi^2$ value. The remaining columns contain the extracted background parameters.

asset, the scarcity of the data prevents a unique determination of the t-channel background dynamics. Ultimately, we have identified a total of four plausible t-channel Regge model variants capable of describing the high-energy data in a satisfactory way. The model specifications are summarized in Table 3.1. We have performed fits for all four possible sign combinations for the $K^{*+}(892)$ vector and tensor couplings. It turns out that, for a given choice of trajectory phases, *two* sets of parameters can be found that produce acceptable results, each with a different sign for $G^t_{K^{*+}(892)}$. Table 3.1 does not mention any model variants with a constant K and a rotating $K^*$ phase, as all result in unsatisfactory values of $\chi^2$, of the order of 6.5. This can be attributed to these models' failure to reproduce the recoil asymmetry, which is found to be the observable most discriminative with respect to the Regge model variant used.

The calculated high-energy observables for each of the four model variants are compared to the data in Figs. 3.2-3.4.

The differential cross sections are displayed in Fig. 3.2. It turns out that this observable is rather insensitive to the phases chosen for the Regge propagators. Indeed, for each of the two investigated phase combinations shown, as well as for the constant K and rotating $K^*$ phase option, it was found that a fair description of the cross sections can be achieved for certain combinations of the parameters.

At the level of the unpolarized observables, there is only one notable difference between the model variants with two rotating phases, and the ones with a constant plus a rotating phase. While the former option results in differential cross sections that fall steadily with t, the latter leads to a smooth oscillatory behavior of the cross sections. This effect can be attributed to interference between the K- and $K^*$-exchange diagrams. When *e.g.* the $K^*$ phase is constant, the interference terms in question have a phase $e^{\pm i\pi\alpha_K(t)}$. Thus, their contribution to the differential cross section is proportional to

$$\begin{aligned} \mathcal{M}^{K-K^*(892)}_{\text{interf.}} &\sim \mathcal{R}e\,[\mathcal{P}^{K}\,(\mathcal{P}^{K^*(892)})^*] \;\sim\; \cos\pi\alpha_K(t) \\ &= \cos\left\{2\pi\left(\frac{t}{2.9\ \text{GeV}^2} - 0.085\right)\right\}\,, \end{aligned} \tag{3.10}$$

since in the unpolarized cross section only the real part of the propagator product $\mathcal{P}^{K}\,(\mathcal{P}^{K^*(892)})^*$ is retained. This corresponds to a harmonic oscillation in $t$, with a period of 2.9 GeV$^2$. For the situation with two rotating trajectory phases, the interference term is proportional to $\cos\pi(\alpha_K(t) - \alpha_{K^*(892)}(t))$, which has a considerably longer oscillation period of 13.3 GeV$^2$.

Another interesting feature of the differential cross sections is the plateau at extreme forward angles ($t \to 0$). This particular behavior cannot be reproduced in a model with only the $K^+$ and $K^{*+}(892)$ exchange diagrams from Fig. 3.1 (a) and (b). This is due to the specific structure of the $\gamma KK$ and $\gamma KK^*$ Lagrangians of Eqs. (A.4) and (A.5), which result in electromagnetic vertex factors going to zero at $t = 0$. The presence of a Regge propagator does not alter that fact since, at low $|t|$, it approaches the Feynman propagator by construction. Figure 3.2 illustrates the above for the $\gamma KK^*$ interaction, by also showing the $K^{*+}(892)$ contribution (dashed curves) to the differential cross section. Traditionally, the issue of pure t-channel mechanisms being insufficient to describe the data was resolved by resorting to so-called (over)absorption mechanisms [120]. The underlying principle is, simply stated, the following. Elastic and inelastic rescattering of the initial $\gamma p$ and final $K^+\Lambda$ states result in a loss of flux, and thus a reduction of the $p(\gamma, K^+)\Lambda$ amplitude. Hereby, the lower partial waves are absorbed most. As a consequence, the sum of all reduced partial-wave amplitudes will no longer be identically zero at $t = 0$. Although this prescription is quite effective in describing the cross-section data, it results in an unphysical change of sign of the lowest partial waves. In the model presented here, the plateau in the differential cross section is naturally reproduced through the inclusion of the gauge-restoring $s$-channel electric Born term (Eq. (3.7)). Due to its vertex structure, this diagram has an amplitude which peaks at extreme forward angles. When $|t|$ increases, its influence gradually diminishes and, as is clear from Fig. 3.2, the $K^{*+}(892)$- exchange diagram starts dominating the process. The $K^+$ contribution remains quite modest in the entire $t$ region under consideration, since $\mathcal{P}_{\text{Regge}} \sim s^{\alpha(t)}$ and the $K^+$ trajectory has a smaller offset than the $K^{*+}(892)$ trajectory (Eqs. (3.5) and (3.6)). The inclusion of the $s$-channel electric Born diagram can result in either a peak or a plateau, depending on the relative values of the coupling constants of the $K^{*+}(892)$-exchange and nucleon-pole diagram. In the $p(\gamma, K^+)\Lambda$ case, the interplay between both diagrams results in a plateau.

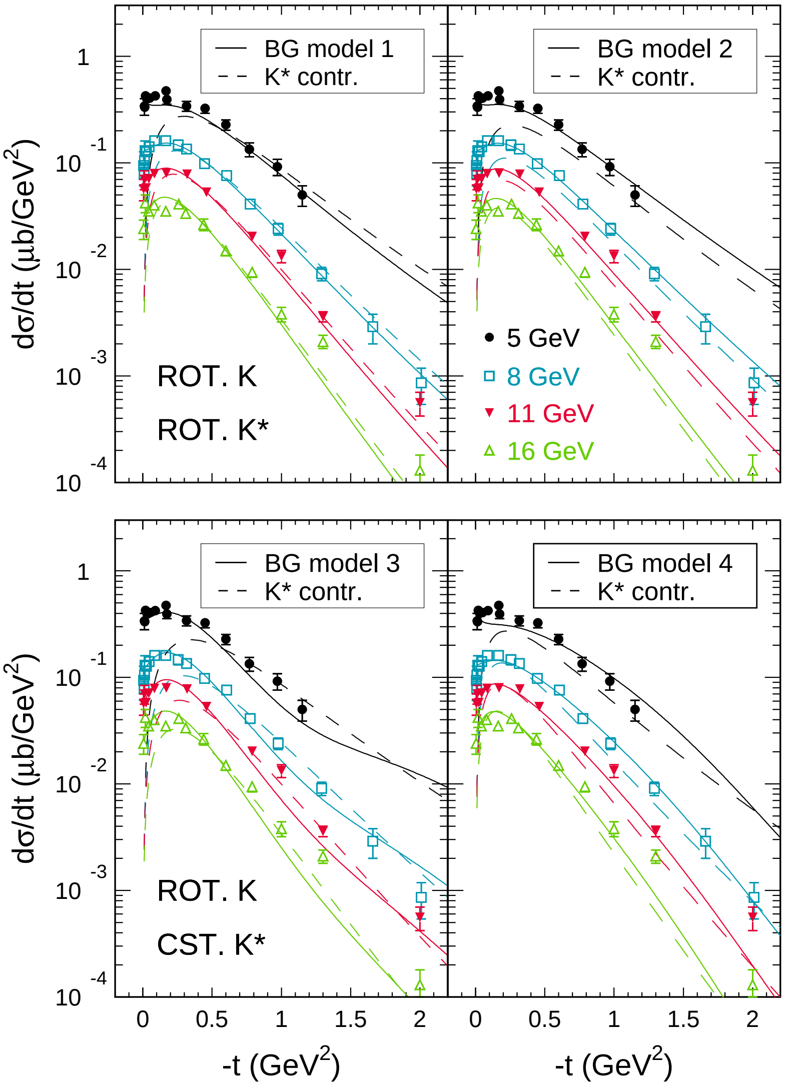

**Figure 3.2** Forward-angle differential $p(\gamma, K^+)\Lambda$ cross sections at photon lab energies of 5 (●), 8 (□), 11 (▼) and 16 (△) GeV. The upper panels correspond to the Regge BG models 1 and 2, with a rotating phase for the $K^+$ and $K^{*+}(892)$ trajectories. In the lower panels, BG models 3 and 4, with a constant $K^{*+}(892)$ phase, are shown. The full curves represent the complete result, while for the dashed curves only the $K^{*+}(892)$ contribution was considered. The data are from Ref. [116].

Figure 3.3 displays the photon beam asymmetry $\Sigma$ at $\omega_{lab} = 16$ GeV. This observable is extremely well reproduced in all four models presented here. Its insensitivity to the particular choice of background model is even more pronounced than for the differential cross sections. Only the result for model variant 1 is shown, since the three other curves are nearly identical. The asymmetry is small at extreme forward angles, rising quickly towards 1. The fact that the $\sigma_\perp$ contribution dominates at higher $|t|$ indicates that a natural-parity particle, here the $K^{*+}(892)$, is exchanged. The exchange of the unnatural-parity $K^+$ mostly influences $\sigma_\parallel$, while the $s$-channel Born diagram contributes more or less equally to $\sigma_\perp$ and $\sigma_\parallel$. This explains the behavior of $\Sigma$ at forward angles, where the dynamics are mostly governed by the $s$-channel Born diagram.

To our knowledge, the sole high-energy $p(\gamma, K^+)\Lambda$ recoil asymmetry data available were collected at a photon energy of 5 GeV in the early seventies [119]. A comparison with our results for the different Regge model variants is presented in Fig. 3.4. Since the measured asymmetry is nonzero, we conclude that the t-channel dynamics are governed by the exchange of two or more trajectories. Indeed, polarized baryon asymmetries reflect interference effects, requiring at least two non-vanishing contributions to the amplitude, with different phases.

The recoil asymmetry is an extremely useful observable for constraining the reggeized background dynamics. Firstly, since it is proportional to $\mathcal{I}m\,[\mathcal{P}^K\,(\mathcal{P}^{K^*(892)})^*]$, the assumption of a constant $K^+$ phase would lead to a $\sin \pi\alpha_{K^*}(t)$ dependence for $P$. The calculated asymmetry would then be exactly zero at $t = -0.38$ GeV$^2$. This is, however, precisely the point where the measured asymmetry reaches its maximum.

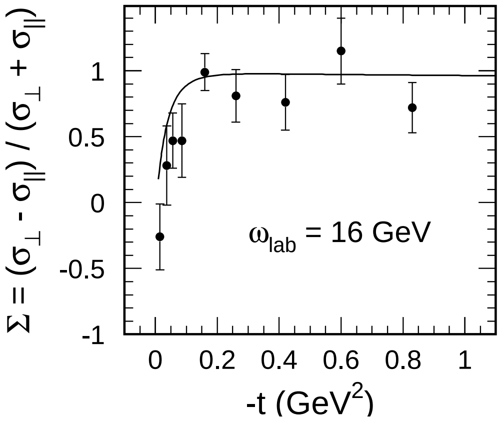

**Figure 3.3** Results for the forward-angle $p(\gamma, K^+)\Lambda$ photon beam asymmetry at $\omega_{lab} = 16$ GeV. The curves for the various models are virtually indistinguishable, so for the sake of clarity we display only the asymmetry for BG model 1. The data are from Ref. [118].

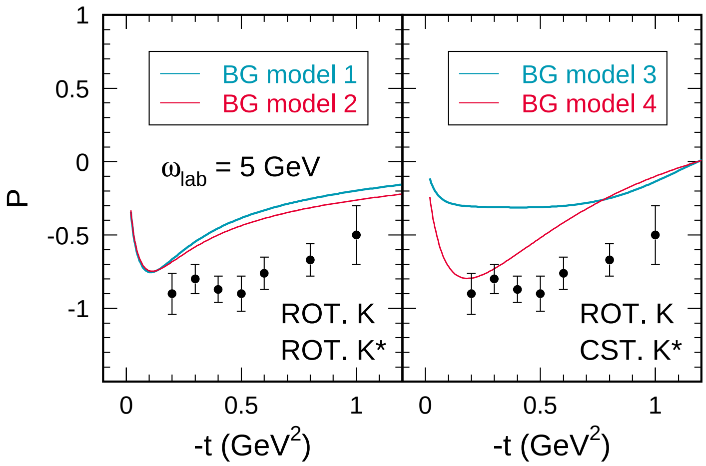

**Figure 3.4** Results for the forward-angle $p(\gamma, K^+)\Lambda$ recoil asymmetry at $\omega_{lab} = 5$ GeV. The blue and red curves in the left panel correspond to the Regge BG models 1 and 2, respectively, with a rotating phase for the $K^+$ and $K^{*+}(892)$ trajectories. In the right panel, BG models 3 (blue) and 4 (red), with a constant $K^{*+}(892)$ phase, are shown. The data are from Ref. [119].

This explains why the possibility of a constant $K^+$ trajectory phase is rejected. Secondly, the sign of the recoil asymmetry is directly linked to the relative signs of the $g_{K^+\Lambda p}$ and $G^{v,t}_{K^{*+}(892)}$ couplings. Indeed, Table 3.1 shows that the negative sign for the recoil asymmetry imposes severe constraints upon the signs of the $K^{*+}(892)$ couplings. For a rotating $K^{*+}(892)$ phase, the coupling $G^{v}_{K^{*+}(892)}$ should be positive; for a constant $K^{*+}(892)$ phase a negative vector coupling is needed. The sign of the tensor coupling appears to be of less importance.

## 3.2 The $\gamma p \longrightarrow K\Sigma$ channels

### 3.2.1 $K^+\Sigma^0$ photoproduction

Since the interaction Lagrangians for the $p(\gamma, K^+)\Lambda$ and $p(\gamma, K^+)\Sigma^0$ processes are essentially identical, the $K^+\Sigma^0$ Regge amplitude can be constructed in complete analogy to the $K^+\Lambda$ one. Of the three free model parameters

$$g_{K^+\Sigma^0 p}\,, \qquad G^{v,t}_{K^{*+}(892)} = \frac{e\, g^{v,t}_{K^{*+}(892)\,\Sigma^0 p}}{4\pi}\, \kappa_{K^+K^{*+}(892)}\,, \tag{3.11}$$

$g_{K^+\Sigma^0 p}$ is constrained between

$$0.9 \leq \frac{g_{K^+\Sigma^0 p}}{\sqrt{4\pi}} \leq 1.3 \tag{3.12}$$

on the basis of broken SU(3)-flavor symmetry, whereas the $K^{*+}(892)$ vector and tensor couplings are left entirely free. For each trajectory, a choice between constant or rotating phases again needs to be made.

Unfortunately, the published $p(\gamma, K^+)\Sigma^0$ data for $\omega_{lab} \gtrsim 4$ GeV are rather scarce. The relevant low-$|t|$ data comprise 48 differential cross section points in total, at the selected energies $\omega_{lab} = 5, 8, 11$ and 16 GeV [116], as well as 8 photon beam asymmetry points at $\omega_{lab} = 16$ GeV [118]. No high-energy hyperon-polarization measurements have been performed for the $K\Sigma$ channels.

In our treatment of $K^+\Lambda$ photoproduction (Sec. 3.1), the recoil asymmetry $P$ was found to be particularly sensitive to the details of the Regge amplitude, much more so than the unpolarized cross section and photon beam asymmetry. The absence of high-energy recoil-polarization data for the $p(\gamma, K^+)\Sigma^0$ process constitutes a serious hindrance to constraining the various Regge-model parameters. There is, however, a way to circumvent this problem. While a pure $t$-channel approach falls short of providing a quantitative description of the resonance-region data, the Regge model has been observed to reproduce all trends of the polarized and unpolarized $p(\gamma, K^+)\Lambda, \Sigma^0$ observables, including $P$ [37, 38, 102]. In view of these considerations, the procedure followed in this section amounts to discarding all Regge model variants which fail in reproducing the sign of the recoil asymmetry in the *resonance region*. Imposing this extra requirement reduces the number of possible model variants from sixteen (four combinations of signs for $G^{v,t}_{K^{*+}(892)}$ multiplied by four combinations of trajectory phases) to four. They are classified in Table 3.2 according to the sign of $G^{v,t}_{K^{*+}(892)}$ and the phases of the $K^+$ and $K^{*+}(892)$ trajectories. The smaller values of $\chi^2$ as compared to what was found for the $K^+\Lambda$ channel (see Table 3.1) can be attributed to the significantly larger error bars for the $K^+\Sigma^0$ high-energy cross sections.

A comparison between the calculated high-energy observables, resulting from the

| BG model | $K^+/K^{*+}(892)$ phase | $\frac{g_{K^+\Sigma^0 p}}{\sqrt{4\pi}}$ | $G^v_{K^{*+}(892)}$ | $G^t_{K^{*+}(892)}$ | $\chi^2$ |
|---|---|---|---|---|---|
| 1 | rot. K, rot. K* | 1.3 | 0.32 | 0.77 | 1.25 |
| 2 | rot. K, rot. K* | 1.3 | 0.33 | -0.86 | 1.28 |
| 3 | rot. K, cst. K* | 1.3 | -0.35 | 0.68 | 1.31 |
| 4 | rot. K, cst. K* | 1.3 | -0.32 | -0.87 | 1.27 |

**Table 3.2** Fitted coupling constants for the Regge background (BG) model variants describing both the high-energy $p(\gamma, K^+)\Sigma^0$ data [116, 118] and the sign of the recoil polarization in the resonance region [57]. The phase options for the $K^+$ and $K^{*+}(892)$ trajectories are listed in the second column. The last column mentions the attained $\chi^2$ value for the high-energy data.

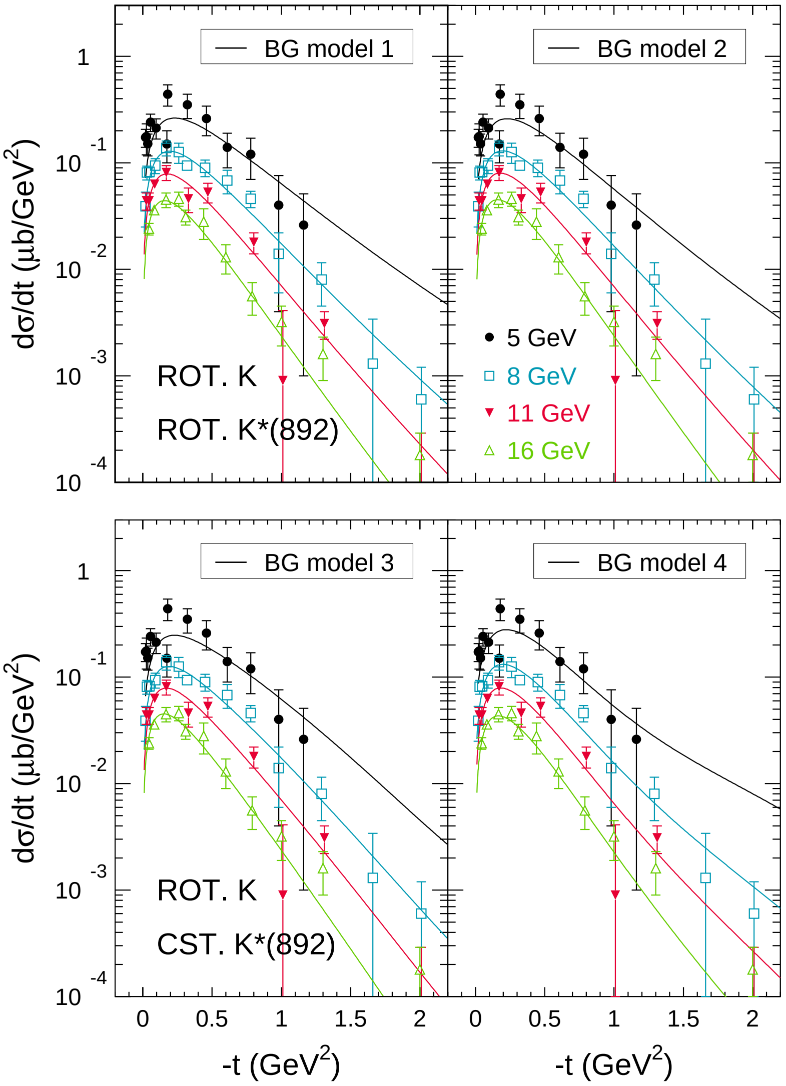

**Figure 3.5** Low-t differential $p(\gamma, K^+)\Sigma^0$ cross sections at photon lab energies of 5 (●), 8 (□), 11 (▼) and 16 (△) GeV. The left panel corresponds to the Regge BG model variants with a rotating phase for the $K^+$ and $K^{*+}(892)$ trajectories. In the right panel, the BG models with a rotating $K^+$ and constant $K^{*+}(892)$ phase are shown. The data are from Ref. [116].

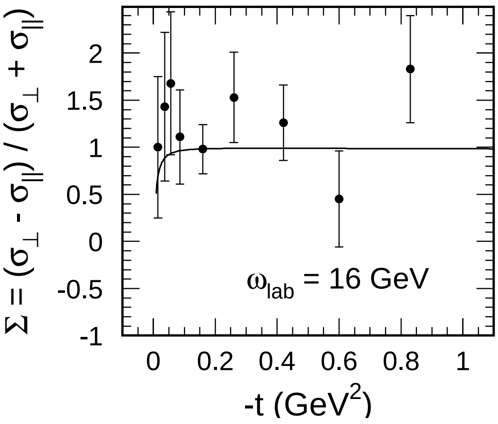

**Figure 3.6** Results for the forward-angle $p(\gamma, K^+)\Sigma^0$ photon beam asymmetry at $\omega_{lab}$ = 16 GeV. The curves for the various background models are nearly indistinguishable. For the sake of clarity, only the result for BG model 1 is displayed. The data are from Ref. [118].

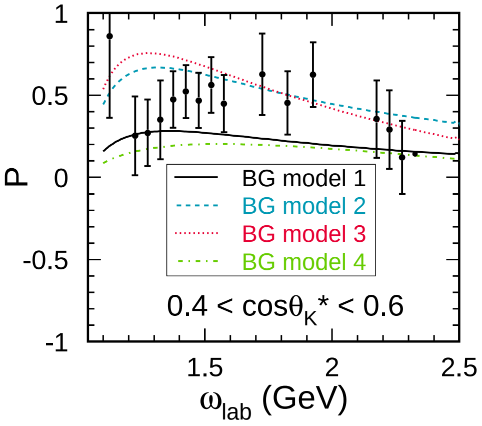

**Figure 3.7** Results for the $p(\gamma, K^+)\Sigma^0$ recoil asymmetry in the resonance region, for $0.4 < \cos\theta_K^* < 0.6$. The data are from Ref. [57].

four Regge model variants of Table 3.2, and the data is shown in Figs. 3.5 and 3.6. Figure 3.7 displays the recoil asymmetry in the resonance region for one representative $\cos\theta_K^*$ bin. As expected, the differential cross section (Fig. 3.5) and photon beam asymmetry (Fig. 3.6) are rather insensitive to the choices made with respect to the trajectory phases and the signs of the coupling constants. On the other hand, the overall positive sign of the recoil asymmetry is only compatible with the four specific sign and phase combinations from Table 3.2. In particular, a strong correlation between the phase of the $K^{*+}(892)$ trajectory and the sign of the corresponding vector coupling is observed. A rotating (constant) $K^{*+}(892)$ phase requires a positive (negative) $G^{\nu}_{K^{*+}(892)}$ coupling.

It is clear from Table 3.2 and Figs. 3.5-3.6 that the high-energy data do not allow to further discriminate between the retained Regge model variants, as all four provide a comparably good description.

### 3.2.2 $K^0\Sigma^+$ photoproduction

Due to the lack of $\gamma p \rightarrow K^0\Sigma^+$ data for $\omega_{lab} \gtrsim 4$ GeV, we are forced to determine the Regge amplitude for this process through comparison with the resonance-region data. We deem this to be a feasible strategy, as the Regge model is known to provide very reasonable descriptions of the $K^+\Lambda$ and $K^+\Sigma^0$ photoproduction observables in the resonance region [37,38,102].

In principle, isospin arguments allow one to transform a reaction model for $\gamma p \rightarrow K^+\Sigma^0$ into one for $\gamma p \rightarrow K^0\Sigma^+$. By exploiting the fact that the $\Sigma^+$ and $\Sigma^0$ hyperons are members of an isotriplet, any coupling constant occurring in the $K^+\Sigma^0$ photoproduction amplitude can be converted into the corresponding $p(\gamma, K^0)\Sigma^+$ parameter. The strong coupling strengths are linked via $SU(2)$ Clebsch-Gordan coefficients, whereas for relating the electromagnetic couplings, experimental input in the form of $\Gamma_{K^* \rightarrow K\gamma}$ decay widths is required. The isospin relations used in this work can be found in Appendix A.3.

In practice, developing a common description for isospin-related channels is often less straightforward than one might infer from the preceding paragraph. Subtle interference effects might, for example, cause certain contributions to be masked in one channel, but strongly enhanced in the other. In fact, reconciling the $p(\gamma, K^+)\Sigma^0$ and $p(\gamma, K^0)\Sigma^+$ model predictions in the resonance region has proven challenging, as the measured $\Sigma^+$ cross-sections are considerably smaller than those for the $\Sigma^0$ [58,60,64]. This observation is in apparent contradiction with the relation

$$g_{K^0\Sigma^+p} = \sqrt{2}\, g_{K^+\Sigma^0p} \tag{3.13}$$

(see Appendix A.3), with similar expressions holding when a $N^*$, $K^*$ or $Y^*$ resonance is involved at the vertex.

In isobar models, this difficulty is often circumvented by strongly reducing the $g_{K\Sigma p}$ coupling in both channels (thus disregarding the $SU(3)_f$ constraints of Eq. (3.12)), and/or by carefully counterbalancing the superfluous strength in the $K^0\Sigma^+$ channel through destructive interferences induced by other contributions [27,29]. It shall be demonstrated that, in the context of the RPR approach, this issue can be elegantly resolved at the level of the *background* terms.

It will become clear that the $p(\gamma, K^+)\Sigma^0$ Regge model variants proposed in Sec. 3.2.1 cannot be readily extended to the $K^0\Sigma^+$ channel. Since the $\gamma KK$ vertex is proportional to the kaon charge, the K-trajectory exchange diagram, as well as the accompanying gauge-restoring s-channel electric Born term, do not contribute to the $K^0\Sigma^+$ photoproduction amplitude. Therefore, the equivalent of Eq. (3.7) in this channel simply reads:

$$\mathcal{M}_{\text{Regge}}(\gamma\, p \to K^0\Sigma^+) = \mathcal{M}_{\text{Regge}}^{K^{*0}(892)} . \tag{3.14}$$

Figure 3.8 displays the predictions for the $p(\gamma, K^0)\Sigma^+$ differential cross section for one particular $\cos\theta_K^*$ bin in the resonance region, using the above-mentioned form for the amplitude. The $G^{v,t}_{K^{*0}(892)}$ couplings have been determined through the isospin relations from Appendix A.3, starting from the fitted values listed in Table 3.2. The same Regge propagator has been assumed for the $K^{*0}(892)$ and $K^{*+}(892)$ trajectories. It is instantly clear that the model parameters determined from the high-energy $\gamma p \to K^+\Sigma^0$ data, when converted to the $K^0\Sigma^+$ channel, result in cross sections that overshoot the experimental data by a factor of 10. Thus, an amplitude of the type of Eq. (3.14) apparently does not suffice to provide a reasonable description of the $\gamma p \to K^0\Sigma^+$ process [1].

A parallel can be drawn between the Regge descriptions of photoinduced kaon and pion production. Indeed, in Refs. [37,38,102], Guidal, Laget and Vanderhaeghen modelled the charged-$\pi$ photoproduction channels through $\pi$ and $\rho$ trajectory exchanges.

---

[1] In this respect, we deem it relevant to mention the $K^0\Sigma^+$ total cross-section result obtained by Guidal, Laget and Vanderhaeghen [40] by means of Eq. (3.14). As confirmed to us by the authors [121], the curves shown in Fig. 3 of their article do not take into account the isospin factor of $\sqrt{2}$, relating the strong $g_{K^+\Sigma^0 p}$ and $g_{K^0\Sigma^+ p}$ couplings (Eq. (3.13)). Inclusion of this factor would increase the quoted cross section by a factor of two, considerably worsening the quality of agreement with the data.

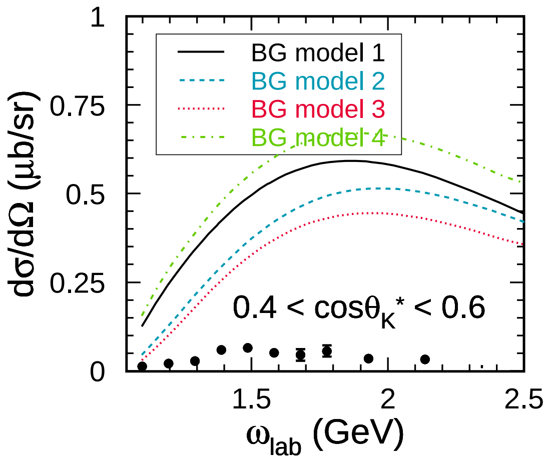

**Figure 3.8** Results for the $p(\gamma, K^0)\Sigma^+$ differential cross section in the resonance region for $0.4 < \cos\theta_K^* < 0.6$, obtained by converting the model parameters from Table 3.2 to the $K^0\Sigma^+$ channel and using Eq. (3.14). The data are from Ref. [64].

In $\pi^0$ production, on the other hand, an $\omega$ trajectory was introduced to compensate for the vanishing $\pi$-exchange diagram. Similarly, in the absence of a $K^0$ contribution to the $K^0\Sigma^+$ amplitude, a higher-mass trajectory may become important in this channel, serving to counterbalance the $K^{*0}(892)$ strength.

It can be intuitively understood that the strong destructive interference needed to reduce the predicted cross sections to the level of the data (Fig. 3.8) can be efficiently realized when the added contribution exhibits an angular distribution comparable to that of the $K^{*0}(892)$-exchange diagram. This implies that a natural-parity particle should be involved. A second $K^*$ trajectory is likely to realize the required effect. As it turns out, the PDG tables hint at the presence of such a trajectory, with the $K^*(1410)$ vector particle as first materialization and the $K_2^*(1980)$ as a probable second member. However, whereas the meson trajectories tend to possess a more or less universal slope, the slope of this experimental $K^*(1410)$ trajectory is significantly smaller than those of the well-known $K(494)$ and $K^*(892)$ trajectories, i.e. 0.53 $\text{GeV}^{-2}$ as compared to 0.7 and 0.85 $\text{GeV}^{-2}$.

As the properties of the $K^*(1410)$ trajectory cannot be put on solid grounds with the available experimental information, we turned our attention to the predictions of a constituent-quark model (CQM) calculation of the kaon spectrum. The Lorentz covariant quark model developed by the Bonn group [12] provides a satisfactory description of the light meson masses and decay properties. Figure 3.9 displays the results of the calculations using two different options ($A$ and $B$) for the Dirac structure of the confinement potential. After selecting from the predicted spectra the states most likely to correspond to the $K^*(1410)$ and $K_2^*(1980)$ resonances, and supplementing these with a set of suitable higher-spin states, a linear relation presents itself.

The slopes of the theoretical and experimental trajectories clearly differ. Strikingly, however, the two calculated curves have practically identical slopes, which are also perfectly compatible with those of the $K(494)$ and $K^*(892)$ trajectories (Eqs. (3.5) and (3.6)). The calculated masses and spins of the members of the $K^*(1410)$ trajectory are nearly perfectly fitted by a linear curve.

We have opted to use the calculated value of 0.83 $\text{GeV}^{-2}$, corresponding to the Bonn-model variant A, leading to a trajectory of the form

$$\alpha_{K^*(1410)}(t) = 1 + 0.83\ \text{GeV}^{-2}\ (t - m^2_{K^*(1410),\text{PDG}})\,, \tag{3.15}$$

with $m_{K^*(1410),\text{PDG}} = 1414$ MeV. The corresponding Regge propagator takes on the form of Eq. (3.4). Again, the trajectory phase may either be constant or rotating.

After adding the $K^{*0}(1410)$-trajectory exchange diagram, the $\gamma p \to K^0\Sigma^+$ Regge am-

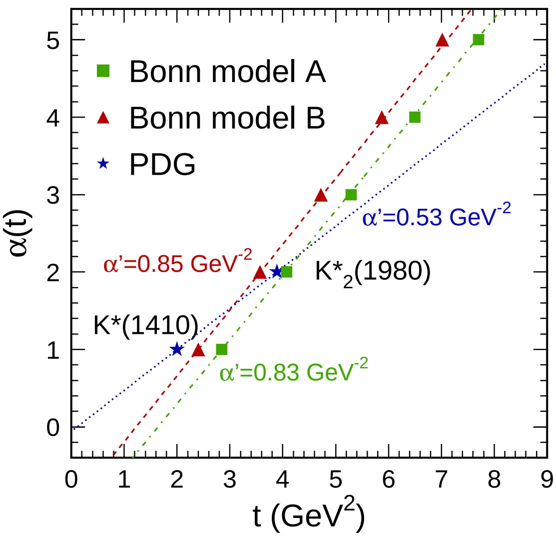

**Figure 3.9** Comparison between the experimental $K^*(1410)$ trajectory and the Bonn-model predictions [12]. The experimental meson masses are from the Particle Data Group [114].

plitude is given by

$$\mathcal{M}_{\text{Regge}}(\gamma p \to K^0\Sigma^+) = \mathcal{M}^{K^{*0}(892)}_{\text{Regge}} + \mathcal{M}^{K^{*0}(1410)}_{\text{Regge}} \tag{3.16}$$

and the number of model parameters is increased by two. Contrary to the $K^{*0}(892)$ parameters, which are constrained by the high-energy $p(\gamma, K^+)\Sigma^0$ data, the $K^{*0}(1410)$ vector and tensor couplings remain as yet unknown, as does the matching trajectory phase. In the absence of high-energy data for the $K^0\Sigma^+$ channel, we fix the $K^{*0}(1410)$ parameters through a fit to the forward-angle ($\cos\theta^*_K > 0$) part of the $p(\gamma, K^0)\Sigma^+$ differential cross-section data for the resonance region.

Table 3.3 displays the extracted $K^{*0}(1410)$ parameters for each of the background models proposed in Sec. 3.2.2. The values of the $G^{v,t}_{K^{*0}(892)}$ couplings can be found from

| BG model | $K^{*0}(892)/K^{*0}(1410)$ phase | $G^v_{K^{*0}(1410)}$ | $G^t_{K^{*0}(1410)}$ | $\chi^2$ |
|---|---|---|---|---|
| 1 | rot. $K^{*0}(892)$, rot. $K^{*0}(1410)$ | -3.0 | -5.0 | 11.8 |
| 2 | rot. $K^{*0}(892)$, rot. $K^{*0}(1410)$ | -3.4 | 4.5 | 8.3 |
| 3 | cst. $K^{*0}(892)$, cst. $K^{*0}(1410)$ | -3.1 | 6.1 | 10.5 |
| 4 | cst. $K^{*0}(892)$, cst. $K^{*0}(1410)$ | -2.9 | -6.3 | 10.2 |

**Table 3.3** Extracted $K^{*0}(1410)$ parameters for each of the background (BG) model variants from Table 3.2. The trajectory phase options are given in the second column, while the last column shows the attained $\chi^2$ value when comparing to the resonance-region $p(\gamma, K^0)\Sigma^+$ cross-section data.

the $G^{v,t}_{K^{*+}(892)}$ values (Table 3.2) by applying the relations from Appendix A.3. It is clear from Table 3.3 that the $K^{*0}(892)$ and $K^{*0}(1410)$ trajectory phases are strongly coupled. It can be intuitively understood that destructive interference is strongest when the same phase choice is adopted for both trajectories. Because of its larger mass, the Regge propagator for the $K^{*0}(1410)$ is smaller than the $K^{*0}(892)$ one, hence a larger coupling constant is needed to produce contributions of similar magnitude. The results for the $p(\gamma, K^0)\Sigma^+$ differential cross sections in the resonance region are shown in Fig. 3.10 for three bins of $\cos\theta^*_K$ in the forward hemisphere. Apart from the slight rise with energy at $\cos\theta^*_K \approx 0.9$, the order of magnitude of the experimental curves is now reasonably well-matched by the calculations. While this channel appears to be background-dominated, some resonance dynamics are clearly missing in the $\omega_{lab} \lesssim 1.7$ GeV region, especially at the more forward angles. This will be remedied in the next chapter.

The inclusion of the $K^{*0}(1410)$ trajectory in the $K^0\Sigma^+$ channel also affects the high-

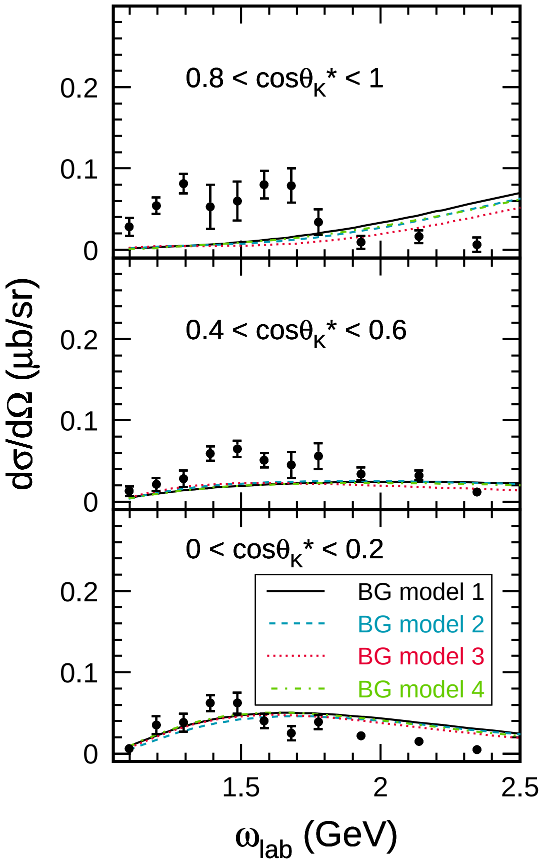

**Figure 3.10** Results for the $p(\gamma, K^0)\Sigma^+$ differential cross section in the resonance region. The data are from Ref. [64].

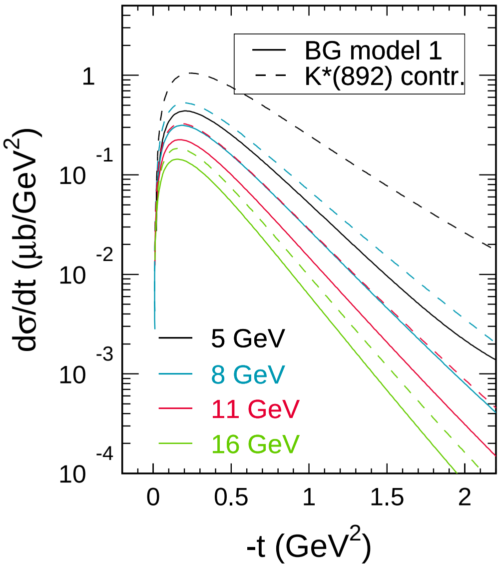

**Figure 3.11** Predictions for the low-t differential $p(\gamma, K^0)\Sigma^+$ cross sections at photon lab energies of 5, 8, 11 and 16 GeV (the highest energy corresponding to the smallest cross-section) using Regge model 1. The full curves represent the total amplitude, whereas the dashed curves show the contribution of the $K^{*0}(892)$ trajectory.

energy observables. Figure 3.11 displays a prediction for the $p(\gamma, K^0)\Sigma^+$ differential cross section, using the Regge model variant 1, at photon lab energies of 5, 8, 11 and 16 GeV. The other three model variants result in a comparable behavior for the cross section. When comparing Fig. 3.11 with Fig. 3.5, it is clear that the Regge amplitude of Eq. (3.16), incorporating both $K^{*0}$ trajectories (full lines), produces cross sections of the same order of magnitude as those for the $\gamma p \to K^+\Sigma^0$ process. On the other hand, use of Eq. (3.14), accounting for $K^{*0}(892)$-trajectory exchange only (dashed lines), leads to cross sections that are higher by a factor of 2 up to 10, depending on the energy. It can be seen that the relative importance of the $K^{*0}(1410)$ contribution diminishes with increasing photon energy. We wish to stress that Fig. 3.11 shows a prediction for the $p(\gamma, K^0)\Sigma^+$ cross section at high energies, obtained with background parameters constrained by the *resonance-region* data. A high-energy measurement performed for this reaction channel would prove extremely useful in putting these predictions to a stringent test.

CHAPTER

4

# KY photoproduction in the resonance region

The extraction of resonance information from scattering reactions is one of the core ongoing projects in the field of hadronic physics. Although the KY channels pose a greater technical challenge than the πN ones, experimental progress is gradually nearing the point where a complete dataset for the resonance region will become available. Over the past years, the KY photoproduction database has been supplemented with new high-precision data from the CLAS [57–59], LEPS [61, 62], GRAAL [63] and SAPHIR [60, 64] facilities. Despite these achievements, considerable diversity of opinion still exists on the theoretical front. The resonance content of the various $p(\gamma, K)Y$ channels constitutes a central topic of discussion. Can convincing evidence for any "missing" resonances as yet be claimed? How likely is it that ill-understood structures in the observables can be explained through final-state interactions or channel couplings, instead of pointing to actual $N^*$ or $\Delta^*$ contributions? These and many other questions continue to call for a convincing answer.

In this chapter, the RPR approach introduced in Sec. 2.4.3 will be applied to the KY photoproduction reactions in the near-threshold regime ($\omega_{lab} \lesssim 3.5$ GeV). When using the background parameters determined from the high-energy data (Chapter 3), only the coupling constants of the added $s$-channel diagrams remain to be constrained to the resonance-region data. We will compare various implementations of the RPR model and investigate which known resonance contributions are required to fit the data presently at hand. In addition, we will examine to what extent the description of the data can be improved by introducing "new" resonances. The $\gamma + p \to K^+\Lambda$ process is tackled in Sec. 4.1, whereas Sec. 4.2 focuses on a simultaneous description of the $\gamma + p \to K^+\Sigma^0$ and $K^0\Sigma^+$ channels.

## 4.1 The $\gamma + p \to K^+\Lambda$ channel

In contrast to their smooth behavior at high $\omega_{lab}$, the $p(\gamma, K^+)\Lambda$ observables exhibit a richer structure in the near-threshold region. The total cross section is dominated by a pair of broad shoulders, suggesting contributions from several overlapping resonances. In the RPR approach, these are modeled by superimposing a number of $s$-channel diagrams onto the reggeized background. For the high-energy description from Sec. 3.1 to remain valid, it is required that all $N^*$ contributions vanish in the high-$s$ limit. As explained in Sec. 2.4.3, the latter is accomplished by introducing a Gaussian form factor at each of the strong $K\Lambda N^*$ vertices.

The results presented in this section constitute an update of those contained in Ref. [122]. The data used in the fitting procedure have been supplemented with new datapoints from the GRAAL collaboration [63].

### 4.1.1 $N^*$ contributions

In previous analyses, the $S_{11}(1650)$, $P_{11}(1710)$ and $P_{13}(1720)$ states (which we will refer to as the "core" $N^*$s) were identified as the main resonance contributions to the $p(\gamma, K^+)\Lambda$ reaction dynamics [28, 123, 124]. While the relevance of these "core" resonances has long been considered a well-established fact, very recently two independent analyses have called the importance of the $P_{11}(1710)$ state into question [30, 33].

For most observables, the core set of $N^*$s falls short of reproducing the experimental results in the region 1.3 GeV $\leq \omega_{lab} \leq$ 1.6 GeV (or, 1.8 GeV $\leq W \leq$ 2 GeV). The Particle Data Group mentions the two-star $P_{13}(1900)$ as the sole established nucleon resonance in the 1900-MeV mass region [114]. Taking into account the width of 500 MeV cited for this resonance, it appears unlikely that the $P_{13}(1900)$ state by itself can explain the quite narrow structure visible in the measured forward-angle cross sections [58]. Various authors have suggested that a second, as yet unknown resonance is manifesting itself in the $p(\gamma, K^+)\Lambda$ observables.

In the past few years, many claims have been made with respect to the nature of this missing state. A new $D_{13}$ resonance was first introduced in Ref. [28] to explain a structure in the old SAPHIR total cross-section data [55] at $W \approx 1900$ MeV. Hitherto unobserved in $\pi N$ reactions, this $D_{13}$ state has been predicted in constituent-quark model

| $N^*$ set | $S_{11}(1650)$, $P_{11}(1710)$, $P_{13}(1720)$ ("core") | $P_{13}(1900)$ (PDG) | $D_{13}(1900)$ ("missing") | $P_{11}(1900)$ ("missing") | NFP |
|---|---|---|---|---|---|
| a | ★ | – | – | – | 8 |
| b | ★ | – | – | ★ | 9 |
| c | ★ | ★ | – | – | 13 |
| d | ★ | – | ★ | – | 13 |
| e | ★ | ★ | – | ★ | 14 |
| f | ★ | ★ | ★ | – | 18 |

**Table 4.1** Sets of $N^*$ resonances used in the RPR calculations for $K^+\Lambda$. The last column mentions the number of free parameters in the resulting RPR $p(\gamma, K^+)\Lambda$ amplitude. This number does not include background couplings, since they were fixed against the high-energy data.

calculations by Capstick and Roberts with a significant branching into the $K\Lambda$ channel [16]. The evidence for this "missing" resonance is far from conclusive, however. While recent results from Diaz et al. [35] and Mart et al. [85] appear to confirm that a $D_{13}$ state with a mass around 1900 MeV is required by both the CLAS and SAPHIR $p(\gamma, K^+)\Lambda$ data, the analysis of Ref. [30] contradicts this conclusion. Ref. [125] specifically points to a $P_{11}(1900)$ state as a more likely missing-resonance candidate, while the results from Ref. [34] suggest that a third $S_{11}$ resonance might be playing a role. A recent coupled-channels study of the $(\pi, \gamma)N \rightarrow K\Lambda$ reactions revealed no evidence for any missing resonance; inclusion of the established $P_{13}(1900)$ state proved sufficient to describe the measured structures in the $p(\gamma, K^+)\Lambda$ observables [33]. Following the discussion in Refs. [30, 85, 124–126], we investigate the options of a missing $D_{13}(1900)$ or $P_{11}(1900)$ state.

In the following section, we will present the results of numerical calculations performed with different sets of known and (as yet) unobserved resonances. Table 4.1 gathers the various combinations of $N^*$ states used for these calculations. Since we wish to keep the model uncertainties at a strict minimum, resonances with spin $J$ larger than $3/2$ are not taken into account because the corresponding Lagrangians cannot be given in an unambiguous way [80–82]. This choice is supported by the conclusion from Refs. [33, 127] that spin-5/2 resonances do not contribute significantly to the $p(\gamma, K^+)\Lambda$ reaction dynamics. We also refrain from including resonances with a mass above 2 GeV, in order to minimize any double-counting effects that might arise from superimposing a large number of individual $s$-channel diagrams onto the $t$-channel Regge amplitude.

It is worth noting that the much-debated $W \approx 1900$ MeV cross-section peak is angle dependent in position and shape [58]. This may hint at the interference of two or more resonances with a mass in the indicated *W* range. Alternatively, photoproduction of an $\eta$ particle or of $K\Lambda^*$ and $K^*\Lambda$ states could lead to additional structure in the observables through final-state interactions. We deem that reproducing the angle-dependence of this structure may be easier to accomplish in a Regge-inspired model than in the standard isobar approaches, since reggeization requires the forward- and backward-angle kinematical regions to be treated separately. Here, we direct our efforts towards the forward-angle observables. An investigation of the structure appearing at backward angles would require $u$-channel reggeization.

To our knowledge, the sole other study of the $p(\gamma, K^+)\Lambda$ process in a mixed Regge-isobar framework is the one carried out by Mart and Bennhold (MB) [128]. It differs from ours in many respects. Most importantly, the MB model combines the high-energy $t$-channel Regge amplitude with the *full* Feynman amplitude for the resonance region. Contrary to our RPR approach, isobar background terms are explicitly included, resulting in a larger number of free parameters and a more serious violation of duality. Furthermore, the transition from the resonance to the high-energy region involves a phenomenological mixing of the Regge and isobar parts. Finally, Mart and Bennhold have considered only the case of rotating phases for the $K^+$ and $K^{*+}(892)$ trajectories. With regard to the $s$-channel resonances, the MB model contains the "core" set of $S_{11}(1650)$, $P_{11}(1710)$ and $P_{13}(1720)$ $N^*$ states, supplemented with a $D_{13}(1900)$. In Sec. 4.1.2, where we show the RPR results for $p(\gamma, K^+)\Lambda$, we will briefly discuss for each observable how our conclusions compare to those of the MB model.

### 4.1.2 RPR model variants for $p(\gamma, K^+)\Lambda$

The latest $p(\gamma, K^+)\Lambda$ resonance-region data provided by CLAS and SAPHIR consist of differential and total cross sections and hyperon polarizations [57, 58, 60] over an extensive energy range. Differential cross sections and photon beam asymmetries for the forward-angle kinematical region have been supplied by LEPS [61, 62]. Further, the GRAAL collaboration has been involved in beam- and recoil- polarization measurements in the first resonance region [63]. The double-polarization results released by CLAS earlier this year [59] constitute the most recent addition to the $p(\gamma, K^+)\Lambda$ database.

The discrepancy between the CLAS and SAPHIR cross sections for the $K^+\Lambda$ final state has been heavily discussed [30, 33, 85]. This issue has been cleared up somewhat with the release of new data by CLAS [58], which are in better agreement with those from SAPHIR [60] than the older CLAS results [57]. Still, a degree of inconsistency between both datasets remains. We shall limit our analysis to the most recent data from CLAS for the sake of consistency, as in Chapter 5 we will be obliged to turn to CLAS as the main provider of electroproduction data.

Since the forward-angle kinematical region constitutes the focus of our analysis, we do not consider any datapoints outside the $\cos\theta_K^* > 0$ range. For the CLAS data of Refs. [57, 58], an even stricter selection is required. It turns out that the CLAS results for $\cos\theta_K^* \lesssim 0.35$ cannot be described by any of the RPR models, even when the data in question are included in the fitting procedure. For this reason, we have opted to only take the $\cos\theta_K^* > 0.35$ part of the CLAS dataset into account. This leaves in total 786 data points with which to adjust the model parameters. The quoted number includes 470 differential cross sections, 193 recoil asymmetries (82 from CLAS and 111 from GRAAL) and 123 photon beam asymmetries (45 from LEPS and 78 from GRAAL).

As data for the double-polarization observables $C_x$ and $C_z$ have only recently become available, we have not been able to use these in the fitting procedure. All results shown for these observables should therefore be considered as pure predictions.

We started our analysis by combining each of the six $N^*$ sets (a through f) from Table 4.1 with the four background model variants (1 through 4) from Table 3.1. This resulted in twenty-four RPR model variants to be considered. In a second step, the parameters of these models were determined by a fit to the data of Refs. [57, 58, 61–63, 116, 118, 119]. While our initial intention was to keep the background couplings entirely fixed, this was found to result in fits of inferior quality. Instead, we allowed each background coupling to vary in a small interval $[c_l, c_u]$ around its high-energy value $c_h$, determined by $\chi^2(c_{l,u}) \leq \chi^2(c_h) + 1$.

Of the initial twenty-four combinations, six were found to stand out as providing the best global description of the high- and low-energy observables. The properties of these "preferred" model variants are summarized in Table 4.2. They are labeled RPR-$2^{(\prime)}$, RPR-$3^{(\prime)}$ and RPR-$4^{(\prime)}$, corresponding to the background (BG) model variants 2, 3 and 4 respectively. The primed (unprimed) notation indicates that a missing $D_{13}$ ($P_{11}$) resonance is included in the amplitude. Apart from this missing state, each model variant in Table 4.2 contains the "core" resonances $S_{11}(1650)$, $P_{11}(1710)$ and $P_{13}(1720)$, as well as the 2-star PDG state $P_{13}(1900)$.

The $\chi^2$ values cited in Table 4.2 result from a comparison of the $p(\gamma, K^+)\Lambda$ calculations with the data in the resonance and high-energy regions. Apart from these "raw" $\chi^2$ values, the number of free parameters (NFPs) serves as an important additional criterion by which to compare the different model variants. For the masses and widths of the known resonances we have assumed the PDG values [114] instead of treating them as additional free parameters as is often done. For the cutoff $\Lambda_{res}$ of the strong

| BG mod. | N* set | RPR mod. | core + $P_{13}(1900)$ | $P_{11}(1900)$ | $D_{13}(1900)$ | $\Lambda_{res}$ (MeV) | NFP | $\chi^2$ |
|---|---|---|---|---|---|---|---|---|
| 2: rot.K, rot. | f | 2 | ★ | ★ | – | 2461 | 14 | 3.2 |
| $K^*$, $G^t_{K^*} < 0$ | e | $2'$ | ★ | – | ★ | 1636 | 18 | 2.7 |
| | | | | | | | | |
| 3: rot.K, cst. | f | 3 | ★ | ★ | – | 2035 | 14 | 3.2 |
| $K^*$, $G^t_{K^*} > 0$ | e | $3'$ | ★ | – | ★ | 1371 | 18 | 3.1 |
| | | | | | | | | |
| 4: rot.K, cst. | f | 4 | ★ | ★ | – | 1498 | 14 | 3.1 |
| $K^*$, $G^t_{K^*} < 0$ | e | $4'$ | ★ | – | ★ | 1460 | 18 | 3.1 |

**Table 4.2** RPR model variants providing the best description of the $p(\gamma, K^+)\Lambda$ data in the high-energy and resonance regions. Apart from the information also contained in Table 4.1, the Regge background (BG) model is given (using the numbering from Sec. 3.1), as are the resonance cutoff $\Lambda_{res}$ and the attained value of $\chi^2$. "Rot." and "cst." refer to the rotating or constant Regge trajectory phase assumed for the K(494) and K*(892) contributions.

resonance form factors, results between 1400 and 2500 MeV were obtained. These are compatible with the values typically used for the dipole form factors in isobar models.

BG model 1 is missing from Table 4.2, as it failed to produce acceptable results in combination with any of the proposed $N^*$ sets. This prompts the conclusion that a rotating phase for both the K and $K^*$ trajectories, in combination with positive $G^{v,t}_{K^*}$ couplings, is ruled out by the resonance-region data. We stress again that the high-energy observables alone *do not* allow one to distinguish between the background model variants 1 through 4. In fact, BG model 1 closely resembles the Regge model originally proposed by Guidal, Laget and Vanderhaeghen for the description of high-energy electromagnetic production of kaons from the proton [37, 38, 102].

It is clear from Table 4.2 that the best description of the data used in the fitting procedure is achieved with the RPR-2′ amplitude, which is based on BG model 2 and contains a missing $D_{13}(1900)$. When employing BG model 3 or 4, the quality of the fit does not depend on whether a missing $D_{13}$ and $P_{11}$ is used, but the attained values of $\chi^2$ are significantly higher than for RPR-2′. On these grounds, we are tempted to consider $D_{13}(1900)$ as the most likely missing-resonance candidate. However, while RPR-2′ undeniably produces the best result, it should be realized that this model contains four free parameters more than the "unprimed" models. This becomes clear when comparing the Lagrangians for coupling to spin-1/2 and spin-3/2 resonances in Appendix A.1.2. As is discussed in Refs. [93, 125], the inclusion of additional parameters, while invariably leading to a decrease in $\chi^2$, does not always imply an increased likelihood for the resulting model. For this reason, we deem that the presence of a $P_{11}(1900)$

contribution cannot be entirely ruled out at this point. A comparison with observables not included in the fits, such as $C_x$ and $C_z$ (Sec. 4.1.3) and electroproduction responses (Chapter 5), will prove useful in resolving this issue.

### 4.1.3 Results and discussion

**Unpolarized cross section.** Figure 4.1 shows the differential $p(\gamma, K^+)\Lambda$ cross sections obtained with the model variants from Table 4.2 and their respective background contributions. Although the pure Regge model leads to smoother behavior than the full RPR calculations, it produces cross sections having the right order of magnitude. One would expect the best agreement between the background amplitude and the cross-section data to be observed in the high-energy, forward-angle region. This condition is fulfilled by BG models 2 and 4. BG model 3, on the other hand, overestimates the cross section for $\omega_{lab} \gtrsim 2$ GeV at forward angles, but matches it at intermediate angles. We should point out that the BG contribution shown in Fig. 4.1 is not identical to the original BG model from Chapter 3.1. As explained in the previous section, its parameters have been slightly readjusted to fit the data in the resonance region. Apparently, for the RPR variants using BG model 3, an improved description of the resonance-region observables could be attained by allowing the background couplings to increase beyond their high-energy values.

With the exception of the extreme forward-angle range, very comparable results are produced by the different RPR model variants. In other words, the unpolarized cross section is not the ideal observable for distinguishing between the various background and resonant options. Since the energy behavior of the differential cross sections is well reproduced in all six of the proposed RPR models, we conclude that the problematic "flattening out" of the resonance peaks found by Mart and Bennhold [128] is not an issue when the Regge and isobar approaches are combined via the RPR prescription.

Fig. 4.2 illustrates the relative importance of the different $s$-channel contributions to the $p(\gamma, K^+)\Lambda$ cross section for the case of the RPR-2′ model. The $P_{13}(1720)$, $P_{13}(1900)$ and $D_{13}(1900)$ resonances play a vital role in the description of the unpolarized process. Interestingly, the quite reasonable agreement between the background model and the data is spoiled somewhat when the $P_{13}(1720)$ and $P_{13}(1900)$ resonances are included. Particularly striking is the strong destructive interference between the $P_{13}(1900)$ contribution and the "core" amplitude (compare green and purple curves) at forward angles and $\omega_{lab} \approx 1.7$ GeV ($W \approx 2$ GeV). This gives rise to a sharp dip in the cross sections. An additional $D_{13}(1900)$ resonance is needed to temper this structure by interfering destructively with the background and core diagrams. Remarkably, even

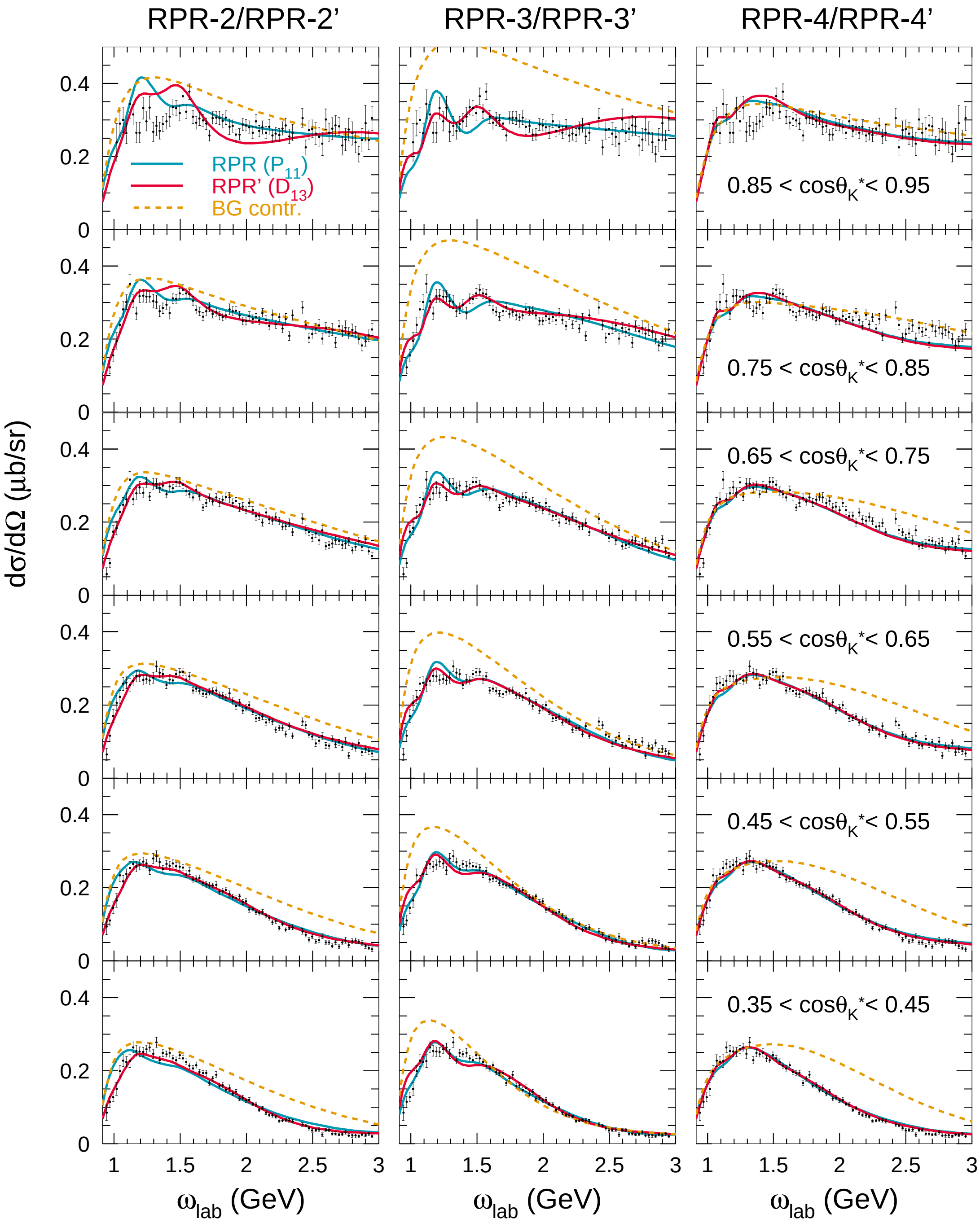

**Figure 4.1** Energy dependence of the forward-angle differential $p(\gamma, K^+)\Lambda$ cross sections in the resonance region. The RPR (blue curves) and RPR′ (red curves) model calculations include the core N*s, the two-star $P_{13}(1900)$, and either a missing $P_{11}(1900)$ or $D_{13}(1900)$. The dashed orange curve corresponds to the background contribution, which is identical for the "primed" and "unprimed" variants. The data are from CLAS [58].

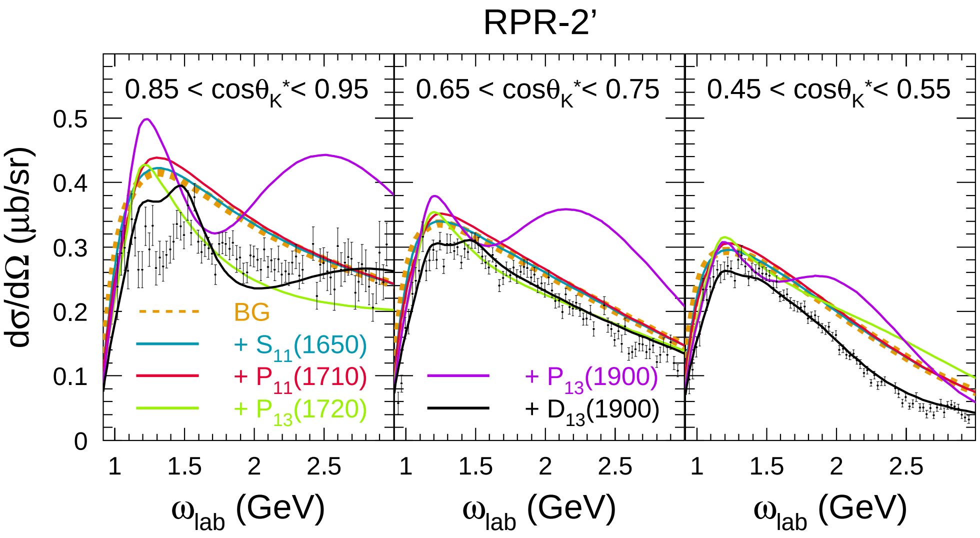

**Figure 4.2** Energy dependence of the differential $p(\gamma, K^+)\Lambda$ cross section in the resonance region, for three representative bins of $\cos\theta^*_K$. The different curves correspond to calculations within the RPR-2′ model, where the amplitude is built up by adding one $N^*$ state at a time. The black curve represents the full RPR-2′ result. The data are from CLAS [58].

though they are generally included in effective-field descriptions of $p(\gamma, K^+)\Lambda$, both the $S_{11}(1650)$ and $P_{11}(1710)$ states turn out to be of minor importance here.

**Recoil asymmetry.** In Figures 4.3 and 4.4, we compare the computed recoil polarizations $P$ with recent data from CLAS [57]. Figure 4.3 demonstrates that all RPR-model variants do an excellent job of describing $P$ over the entire angular region considered for the fitting procedure. Again, the resonance-region data are matched quite well by the background contribution alone. The difference between the Regge and full RPR results is practically negligible for all BG models except 4, implying that the recoil asymmetry is rather insensitive to the number and type of resonant states. Since the RPR-4 and RPR-4′ results are practically indistinguishable, one may conclude that BG model 4 does not support a significant contribution from any “missing” state. As is clear from Fig. 4.4, $P_{13}(1900)$ and $D_{13}(1900)$ constitute the dominant contributions to the RPR-2′ result for $P$, corroborating the conclusions drawn from the differential cross-section data (Fig. 4.3).

In Ref. [128], Mart and Bennhold reported that a satisfactory description of the CLAS recoil polarization could not be achieved in their Regge-inspired model. Particularly, the dip in $P$ at $W \approx 1.75$ GeV ($\omega_{lab} \approx 1.16$ GeV) for $\cos\theta^*_K < 0.6$ proved problematic to describe. This discrepancy was tentatively attributed to an unidentified resonance.

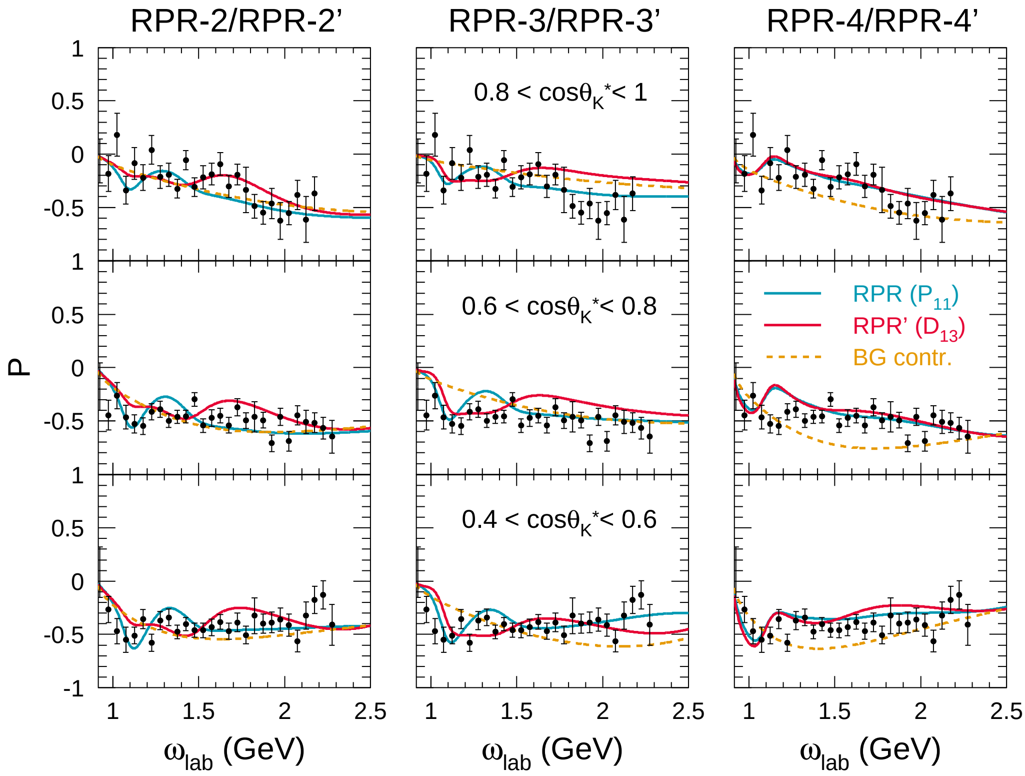

**Figure 4.3** Energy dependence of the $p(\gamma, K^+)\Lambda$ recoil polarization for those bins of $\cos\theta^*_K$ considered in the fitting procedure. Line conventions are as in Fig. 4.1. The data are from CLAS [57].

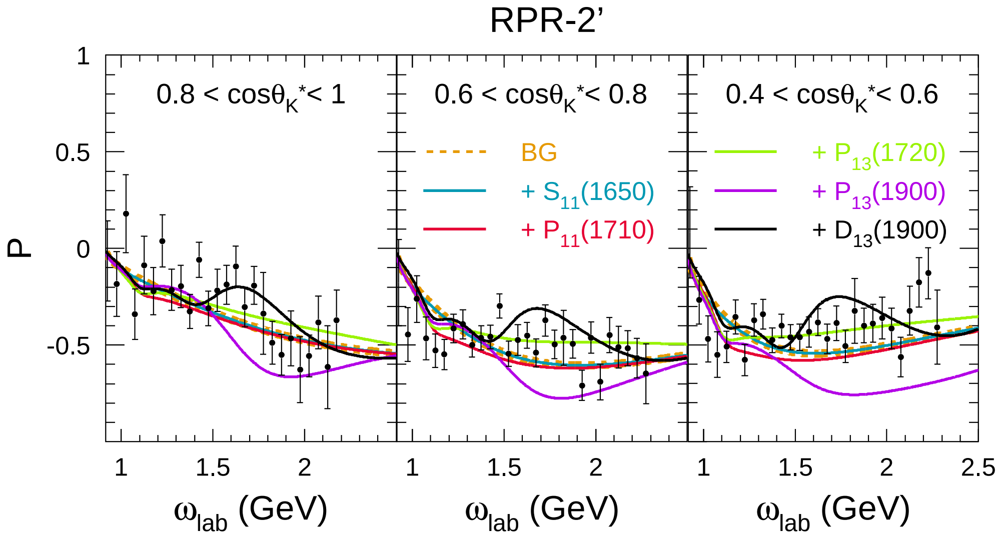

**Figure 4.4** Energy dependence of the $p(\gamma, K^+)\Lambda$ recoil polarization for those bins of $\cos\theta^*_K$ considered in the fitting procedure. Line conventions are as in Fig. 4.2. The data are from CLAS [57].

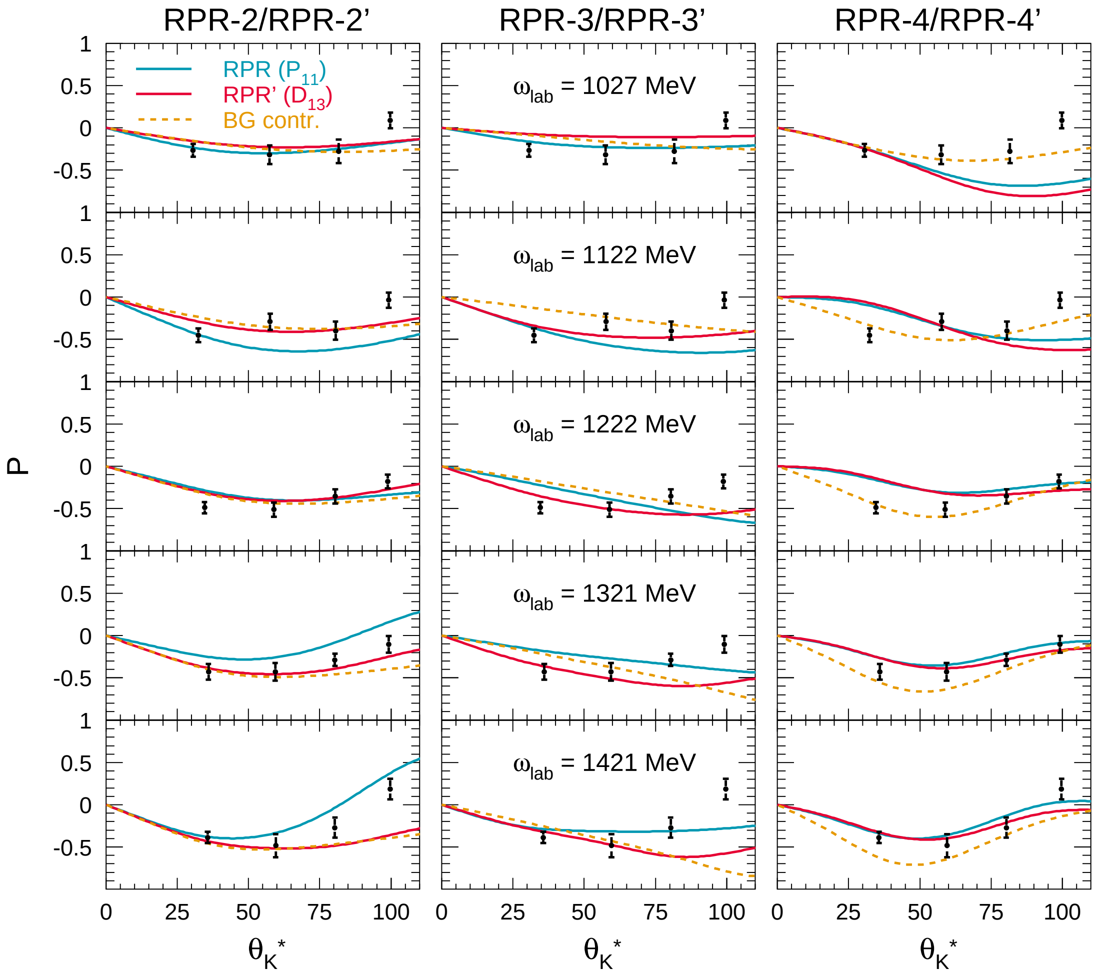

**Figure 4.5** Angular dependence of the forward-angle $p(\gamma, K^+)\Lambda$ recoil polarization for five of the energy bins covered by the GRAAL experiment. Line conventions are as in Fig. 4.1. The data are from [63].

As is clear from the lower graphs in Fig. 4.3, all "unprimed" model variants are able to reproduce the dip in the asymmetries, while the three RPR′ variants lead to a smoother behavior near threshold. Considering the size of the error bars, the importance of this feature should not be overestimated, though.

Very recently, the GRAAL collaboration has released a set of high-quality recoil-polarization data for photon energies between 980 and 1470 MeV [63]. Figure 4.5 features a comparison between the RPR calculations and these data for a number of representative bins in $\omega_{\text{lab}}$. As could be expected, the impact of the specific resonance content of the RPR amplitude is most pronounced at the more backward angles. For BG models 2 and 3, there is an obvious difference between the model variants containing a missing $D_{13}$ and $P_{11}$ state. This difference is significantly less pronounced when assuming BG model 4.

**Photon beam asymmetry.** Data for the photon beam asymmetry $\Sigma$ are available from the LEPS and GRAAL facilities [61, 63]. Our results for this observable are contained in Figs 4.6 to 4.8. Since only a limited number of data points are available, these calculations might be considered more as predictions than as the actual outcome of a fit. As evidenced by Fig. 4.6, each of the proposed RPR model variants reproduces the beam asymmetry well at extreme forward angles, as was the case for $P$. The intermediate angles turn out to present a greater challenge. This observation is compatible with Mart and Bennhold's findings, except that their results underestimated the low-energy data, while we find a more serious discrepancy at the highest energies covered by LEPS. For the photon asymmetries, the MB approach provides a slightly better description than the model variants presented in this work. It should be realized, though, that the number of free parameters contained in the RPR model is considerably smaller. Again, $P_{13}(1720)$, $P_{13}(1900)$ and $D_{13}(1900)$ dominate the resonant part of the amplitudes (Fig. 4.7). With the exception of BG model 4, the difference between the RPR, RPR′ and BG results becomes more pronounced with increasing energy and scattering angle (Fig. 4.8).

**Beam-recoil asymmetries.** Finally, in Fig. 4.9 we show predictions for the beam-recoil polarizations $C_x$ and $C_z$ recently measured at CLAS [59]. Of all observables presented in this section, these are clearly the ones most sensitive to the choice of RPR-model ingredients. While all variants perform well at extreme forward angles, the description in the intermediate-angle region still needs considerable improvement, with the most flagrant discrepancy occurring for $C_z$ in the $W \gtrsim 2$ GeV region. No obvious preference for any particular model variant is expressed by the data. With a view to further refining the existing models, it should prove very instructive to include these observables in the fitting procedure.

Summarizing, we have identified the RPR-2′ model variant as providing the best overall description of the world $K^+\Lambda$ photoproduction data. While the other five RPR amplitudes do not produce equally good results as RPR-2′, we deem it inadvisable to completely discard them at this point. In Chapter 5, we will further test the predictive power of the different variants by confronting them with the world $K^+\Lambda$ electroproduction data.

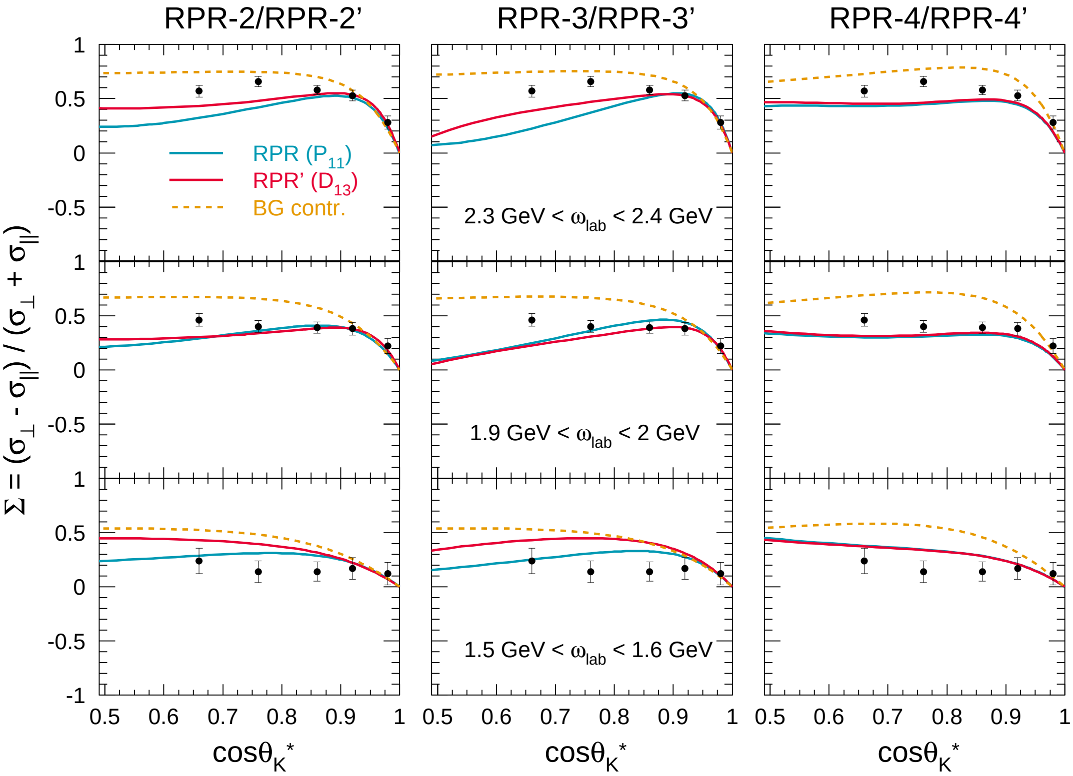

**Figure 4.6** Results for the forward-angle $p(\gamma, K^+)\Lambda$ photon beam asymmetry, for $0.5 < \cos\theta_K^* < 1.0$ and for three representative bins of $\omega_{\text{lab}}$, corresponding to center-of-mass energy bins $2.28$ GeV $< W < 2.32$ GeV, $2.11$ GeV $< W < 2.15$ GeV, and $1.92$ GeV $< W < 1.97$ GeV. Line conventions are as in Fig. 4.1. The data are from LEPS [61].

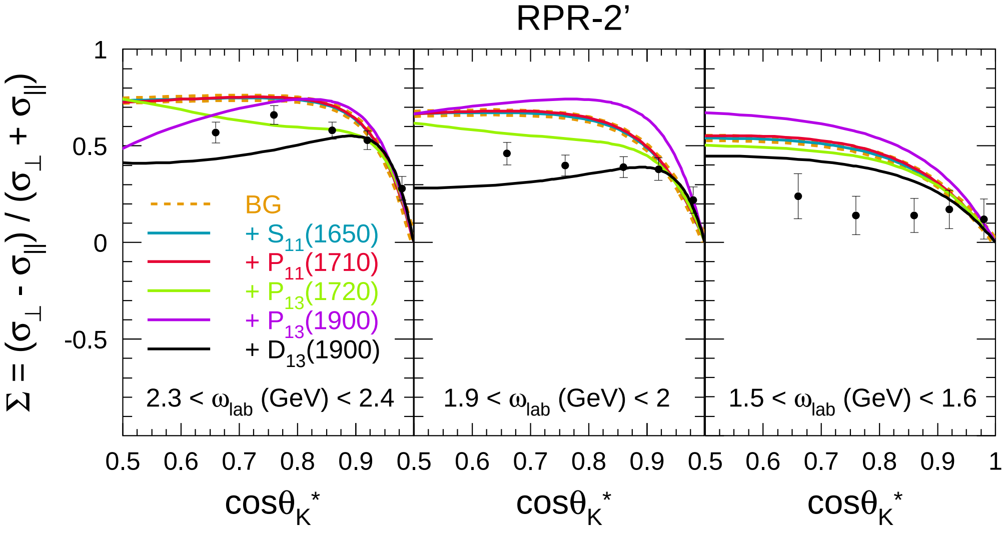

**Figure 4.7** Results for the forward-angle $p(\gamma, K^+)\Lambda$ photon beam asymmetry. Line conventions are as in Fig. 4.2. The data are from LEPS [61].

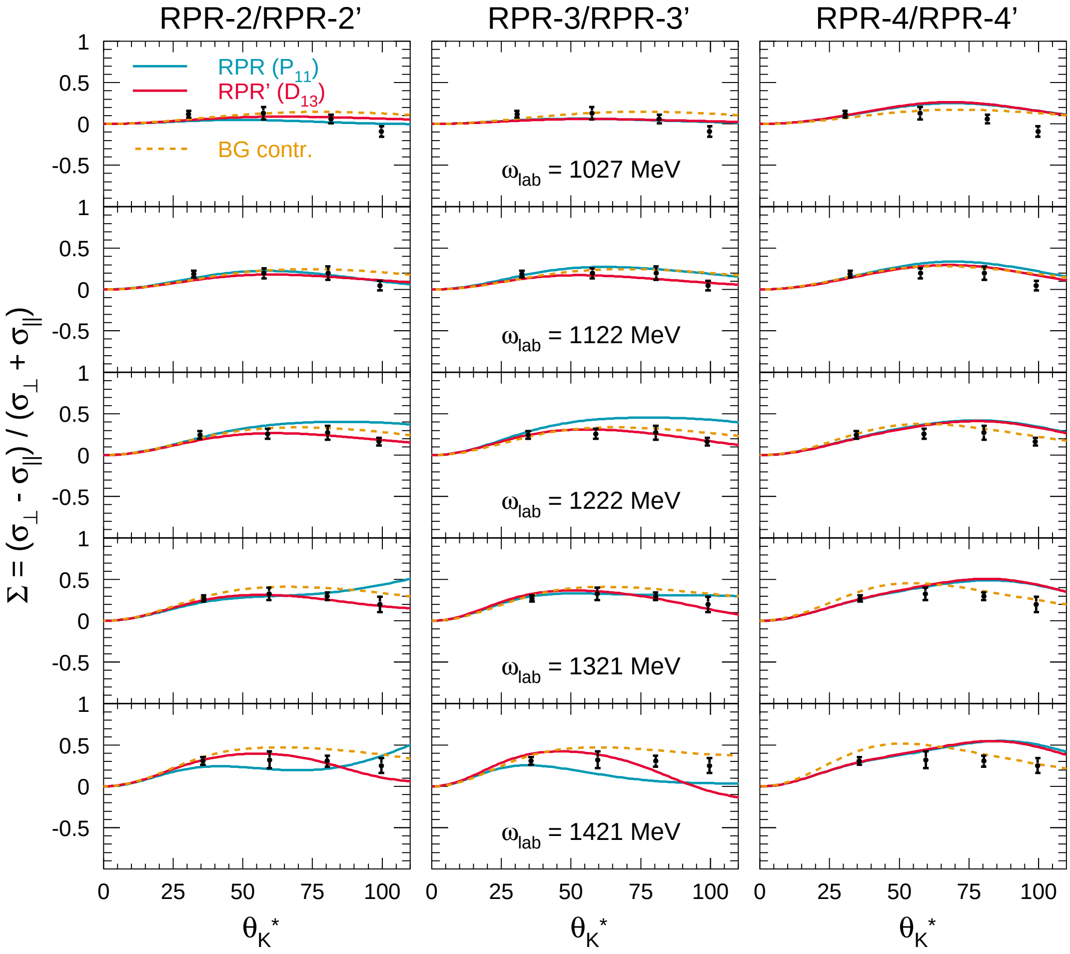

**Figure 4.8** Angular dependence of the forward-angle $p(\gamma, K^+)\Lambda$ photon beam asymmetry, for five of the energy bins covered by the GRAAL experiment. Line conventions are as in Fig. 4.1. The data are from GRAAL [63].

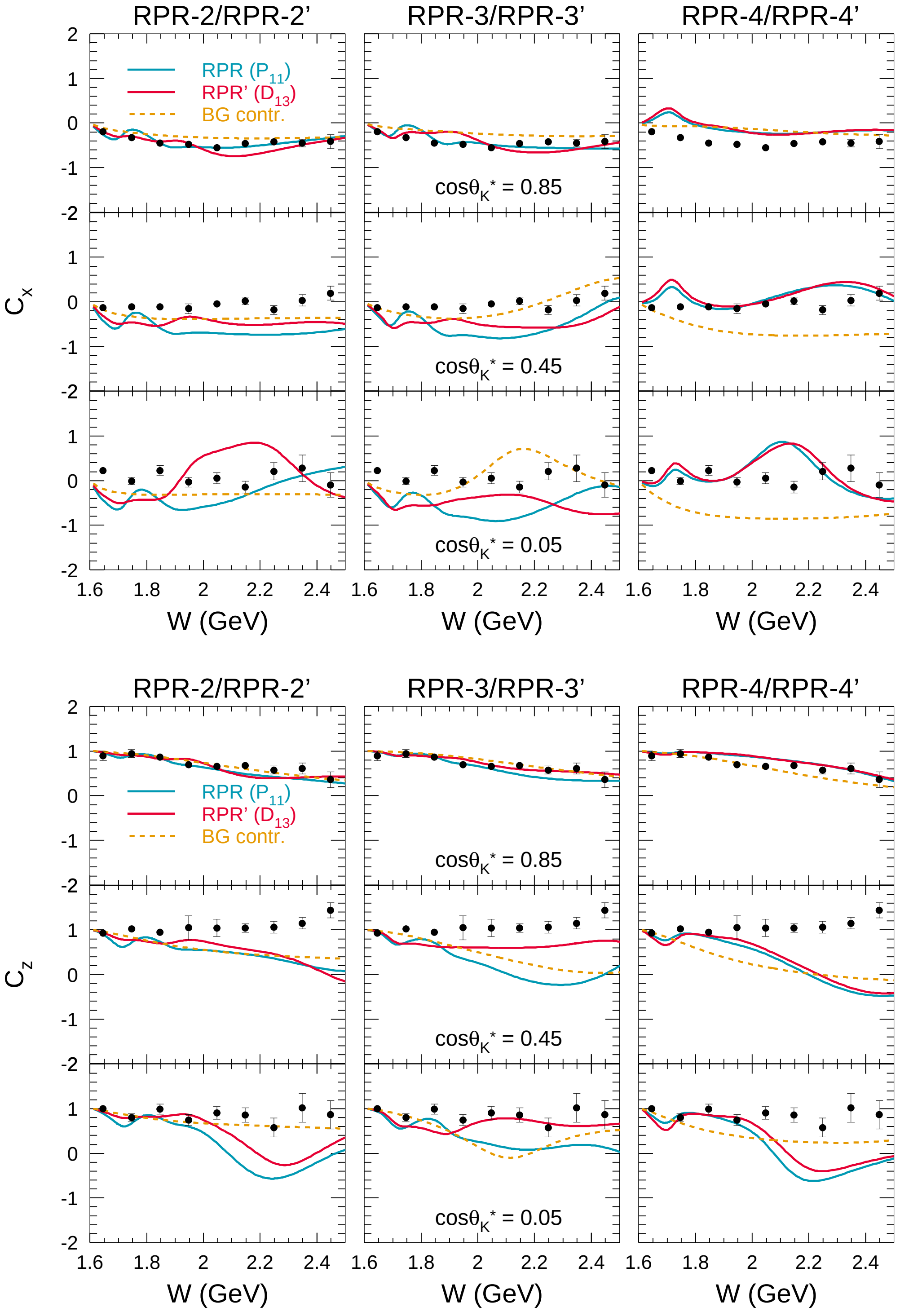

**Figure 4.9** Energy dependence of the $p(\gamma, K^+)\Lambda$ double polarization asymmetry observables $C_x$ (top) and $C_z$ (bottom), for three of the energy bins covered by CLAS. Line conventions are as in Fig. 4.1. The data are from CLAS [59].

## 4.2 The $\gamma p \to K\Sigma$ channels

In this section, the RPR prescription is applied to the $p(\gamma, K)\Sigma$ photoproduction processes. These open a new window onto the hadronic spectrum because the $\Sigma$ particle's isovector nature allows for spin-3/2 states to play a role in the reaction mechanism. While this implies more resonance candidates to be considered, the number of model parameters can be kept within bounds by exploiting the isospin relations between the $\gamma p \to K^+\Sigma^0$ and $\gamma p \to K^0\Sigma^+$ coupling constants. These have been collected in Appendix A.3. The results shown in this section are also contained in Ref. [129].

### 4.2.1 $N^*$ and $\Delta^*$ contributions

In the literature, a consensus regarding the dominant $N^*$ and $\Delta^*$ contributions to the $p(\gamma, K)\Sigma$ dynamics is still far from being reached. Rather confusingly, while most of the published reaction models are based on the SAPHIR data released in the late nineties [55, 56], the few analyses employing a more recent dataset [60, 64] appear to yield different conclusions [30, 34].

A continuous point of debate is the sense or not of introducing new resonances in these channels. Since the $K^+\Sigma^0$ photoproduction data do not exhibit an explicit resonant structure, it was long deemed unnecessary to assume any "missing" states in the $\Sigma$ production reactions [29, 32, 44]. The new data, however, are characterized by significantly reduced error bars, so that a detailed analysis may reveal effects previously clouded by experimental uncertainty. Specifically, it has been shown that the $K^0\Sigma^+$ observables may point to a second $S_{11}$ resonance [64], indications of which have also been reported for the $K^+\Lambda$ channel [34]. On the other hand, the recent analysis of the $K^+\Sigma^0$ and $K^0\Sigma^+$ photoproduction channels by Sarantsev et al. [30] calls for the inclusion of missing $D_{13}(1870)$, $D_{13}(2170)$ and $P_{11}(1840)$ states.

In our calculations, we aim at keeping the number of resonant contributions at a strict minimum, as each implies the introduction of at least one additional parameter. Only resonances with spin $J \leq 3/2$ and a mass below 2 GeV will therefore be considered. Furthermore, we restrict our scope to the established PDG states with a star classification of two or higher. No "missing" states are included at this point.

The six leftmost columns of Table 4.3 gather the combinations of nucleon and $\Delta$ resonances assumed in the various calculations. The simplest resonance set, RS A, corresponds to the standard combination of states assumed in most of the early isobar calculations [28, 29, 130]. As in the $K^+\Lambda$ channel, this "core" $N^*$ set consists of the $S_{11}(1650)$, $P_{11}(1710)$ and $P_{13}(1720)$ resonances. Two $\Delta^*$ states, $S_{31}(1900)$ and $P_{31}(1910)$,

| RS | $P_{13}(1900)$ | $S_{31}(1900)$ | $P_{31}(1910)$ | $D_{33}(1700)$ | $P_{33}(1920)$ | NFP | $\chi^2$ for BG mod. | | | |
|---|---|---|---|---|---|---|---|---|---|---|
| | | | | | | | 1 | 2 | 3 | 4 |
| A | – | ★ | ★ | – | – | 10 | 10.4 | 6.0 | 9.0 | 3.8 |
| B | ★ | ★ | ★ | – | – | 15 | 4.4 | 4.0 | 4.4 | 3.4 |
| C | ★ | ★ | ★ | ★ | – | 20 | 3.5 | 3.6 | 2.2 | 2.1 |
| D | ★ | – | ★ | ★ | – | 19 | 3.5 | 3.7 | 2.4 | 2.3 |
| E | ★ | ★ | – | ★ | – | 19 | 3.7 | 3.8 | 3.1 | 2.4 |
| F | ★ | ★ | ★ | – | ★ | 20 | 3.5 | 3.7 | 3.2 | 2.6 |
| G | ★ | – | ★ | – | ★ | 19 | 3.6 | 3.7 | 3.6 | 2.9 |
| H | ★ | ★ | – | – | ★ | 19 | 3.7 | 4.1 | 3.3 | 2.7 |
| I | ★ | ★ | ★ | ★ | ★ | 25 | 3.5 | 2.8 | 2.0 | 2.0 |

**Table 4.3** Combinations of resonances used in the calculations, in addition to the "core" $N^*$ set consisting of $S_{11}(1650)$, $P_{11}(1710)$ and $P_{13}(1720)$. Also mentioned is the number of free parameters (NFP) for each model variant, not including the background couplings. The nine resonance sets (RS) can be combined with any of the four background model options 1-4 derived in Sec. 3.2 (Tables 3.2-3.3), resulting in a total of 36 RPR model variants (1A, 1B, 2A etc.). The last four columns list the values of $\chi^2$ attained for each combination, after adjusting the resonance parameters to the resonance-region data.

each having spin 1/2 and thus involving one extra free parameter, are also included in RS A. We further consider three additional spin-3/2 resonances: $P_{13}(1900)$, $D_{33}(1700)$ and $P_{33}(1920)$.

In our treatment of $\Lambda$ photoproduction (Sec. 4.1), we estimated the importance of the various $N^*$ and $\Delta^*$ states by visually comparing the magnitude of their contributions to the various observables. For the $K\Sigma$ amplitude, which can contain a considerably larger number of resonance candidates, we adopt a different strategy. We shall perform not merely one, but a series of fits to the resonance-region data. Thereby, the resonances will be added one at a time, and all parameters readjusted after each addition. This will allow us to check the impact of each candidate on the attained value of $\chi^2$ in a more quantitative way.

### 4.2.2 RPR model variants for $p(\gamma, K)\Sigma$

For the $p(\gamma, K^+)\Sigma^0$ reaction, high-precision data are available from CLAS, comprising an extensive set of unpolarized cross sections and hyperon polarizations [57, 58]. Photon-beam asymmetry data for the second and third resonance regions, taken specifically at forward kaon angles, have been provided by LEPS [61]. In addition, the GRAAL collaboration has been involved in beam- and recoil-polarization measurements in the first resonance region over an extensive angular range [63]. For $p(\gamma, K^0)\Sigma^+$, the cross-section and recoil-asymmetry data provided by the SAPHIR collaboration are employed [64].

As this work hinges on t-channel reggeization, only the forward-angle portion of the various datasets is considered for fitting purposes. In order to be consistent with our analysis of the $K^+\Lambda$ channel, we impose the restriction $\cos\theta_K^* > 0.35$ upon the CLAS data, while taking the entire $\cos\theta_K^* > 0.0$ part of the other datasets into account. This leaves in total 618 data points with which to adjust the model parameters. The quoted number includes 435 differential cross sections, 53 recoil asymmetries (49 from CLAS and 4 from GRAAL) and 66 photon beam asymmetries (45 from LEPS and 21 from GRAAL) for the $K^+\Sigma^0$ channel, and for the $K^0\Sigma^+$ channel 60 differential cross sections plus 4 recoil asymmetry points. Unlike for $\Lambda$ production, keeping the $p(\gamma, K)\Sigma$ background parameters fixed to their high-energy values was found to lead to a satisfactory quality of fit. Thus, the only parameters that remain to be adjusted to the resonance-region data are the resonance couplings and the strong resonance cutoff $\Lambda_{res}$. We again assume the PDG values [114] for the masses and widths of the known resonances.

We have combined all resonance sets (RS) A through I listed in Table 4.3 with each of the four background options constructed in Sec. 3.2. This amounts to thirty-six RPR model variants, with parameters fixed to the resonance-region data of Refs. [57,58,61, 63,64]. Table 4.3 lists the attained value of $\chi^2$ for each combination.

From Table 4.3, a number of trends may readily be spotted. Only background (BG) model 1 fails to produce a $\chi^2$ smaller than 3.5 in combination with any of the resonance sets. BG model 2 leads to somewhat better results, although 25 parameters are required to reduce $\chi^2$ below 3.6. Both of the above-mentioned models assume rotating phases for all Regge trajectories, so one may conclude that this choice - though adequate for the high-energy description - is less suitable for the resonance region. The models assuming constant $K^*(892)$ and $K^*(1410)$ phases along with a rotating $K(494)$ phase, i.e. BG models 3 and 4, perform considerably better. Although the minimal value of $\chi^2 = 2.0$ is identical for both model variants, BG model 4 exhibits significantly less need for the inclusion of additional resonances than BG model 3. This is evident when comparing the $\chi^2$ values found for the resonance sets with the smallest (RS A) and largest (RS I) number of free parameters. Note also that all BG model-4 variants with more than 15 free parameters have a $\chi^2$ below 3.0, contrary to BG model 3, for which only three of the resonance sets (C, D and I) perform this well.

Table 4.3 also prompts a number of conclusions regarding the resonant structure of the amplitudes. Comparing RS A and B shows that adding the $P_{13}(1900)$ state significantly improves $\chi^2$ for all four Regge model variants. On the other hand, the conclusions with regard to the $\Delta$ resonances clearly depend on the background choice.

| **BG mod.** | **RS** | **RPR mod.** | NFP | $\chi^2_{K^+\Sigma^0}$ | $\chi^2_{K^0\Sigma^+}$ | $\chi^2$ |
|---|---|---|---|---|---|---|
| 3: rot.K, cst. $K^*(892)$,<br>cst. $K^*(1410)$, $G^t_{K^*(892)} > 0$ | I | 3 | 18 | 1.8 | 3.8 | 2.0 |
| 4: rot.K, cst. $K^*(892)$,<br>cst. $K^*(1410)$, $G^t_{K^*(892)} < 0$ | I | 4 | 18 | 1.9 | 2.6 | 2.0 |

**Table 4.4** RPR model variants providing the best common description of the $p(\gamma, K^+)\Sigma^0$ and $p(\gamma, K^0)\Sigma^+$ data. The Regge background (BG) model and resonance set (RS) are given, using the numbering from Tables 3.2 and 4.3. Also listed are the partial $\chi^2$ values for the $K^+\Sigma^0$ and $K^0\Sigma^+$ channels, as well as the total $\chi^2$.

The general trends for the "preferred" background models 3 and 4 are largely comparable, however. Including the $D_{33}(1700)$ state considerably reduces $\chi^2$, in contrast to $P_{33}(1920)$, which has a fairly limited impact on the quality of the fit (compare RS C to F, D to G, and E to H). Removing either $S_{31}(1900)$ or $P_{31}(1910)$ does not spoil the agreement with the data, indicating that only a single spin-1/2 $\Delta$ resonance is required, the parity of which remains unclear.

Judging by the $\chi^2$ values from Table 4.3, the two RPR model variants providing the best common description of the high- and low-energy $p(\gamma, K)\Sigma$ observables are those assuming background options 3 and 4, combined with the most complete resonance set, RS I. These models will be referred to as RPR-3 and RPR-4, respectively. The specifications for both are summarized in Table 4.4.

### 4.2.3 Results and discussion

The results of the RPR-3 and RPR-4 calculations for the various $p(\gamma, K)\Sigma$ observables are compared to the world data in Figs. 4.10-4.17. The curves indicated as "BG" correspond to the background contributions to the full RPR amplitudes. Also displayed are the results for two alternative RPR model variants, consisting of the "core" resonance set A from Table 4.1 in combination with background model variants 3 and 4, respectively.

#### The $K^+\Sigma^0$ channel

**Differential cross section.** Figure 4.10 shows the $p(\gamma, K^+)\Sigma^0$ differential cross section as a function of $\omega_{lab}$. Both RPR-3 and RPR-4 succeed remarkably well in reproducing this observable, including the subtle "shoulder" in the energy dependence at

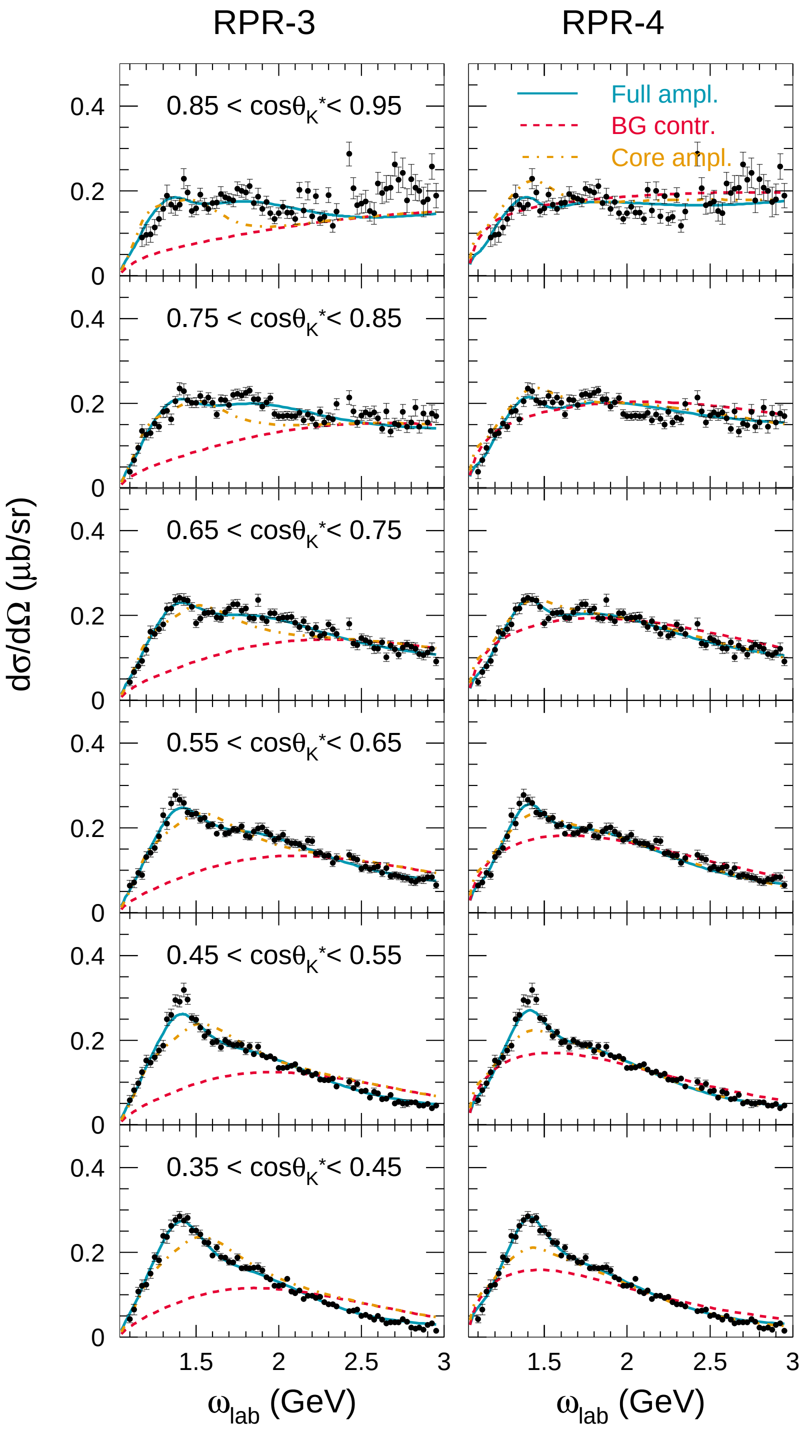

**Figure 4.10** Energy dependence of the differential $p(\gamma, K^+)\Sigma^0$ cross sections in the resonance region, for a number of representative bins in $\cos\theta^*_K$. The full curves represent the complete result, the dotted curves show the contribution of the Reggeized background (BG) amplitude, whereas the dot-dashed curves correspond to RPR model variants containing only the "core" resonance set A from Table 4.3 (see text). The data are from CLAS [58].

$\omega_{\mathrm{lab}} \approx 1.75$ GeV ($W \approx 2.05$ GeV), which is likely to arise from destructive interference of the background with resonances in the 1900-GeV mass range. The "core" models, containing only lower-mass resonances, clearly fall short on this account. In addition, they seriously underestimate the value of the cross-section maximum at the more backward kaon angles. Similar to the $K\Lambda$ case, the Regge model produces smooth curves. Towards the highest $\omega_{\mathrm{lab}}$ measured by CLAS, it describes the unpolarized data without the inclusion of any resonant diagrams. For $\omega_{\mathrm{lab}} \lesssim 2$ GeV ($W \lesssim 2.15$ GeV), $s$-channel contributions are obviously required.

**Recoil and photon beam asymmetry.** The computed recoil polarization $P$ and photon beam asymmetry $\Sigma$ are shown in Figs. 4.11-4.14. Both the LEPS and GRAAL data for these observables are well reproduced by RPR-3 and RPR-4. Again, the Regge contribution in itself provides a good approximation of the experimental hyperon polarization. This justifies the choice to constrain the Regge model variants by requiring them to predict the correct sign for $P$ in the resonance region. In their description of the recoil asymmetry, the "core" models perform comparably to RPR-3 and RPR-4, indicating that the size of the error bars for this observable hampers the extraction of information on the underlying resonance structure. While the Regge and core amplitudes reproduce the sign of the photon beam asymmetry, its magnitude and energy dependence can only be explained by a reaction model containing a sufficiently large number of resonances. The impact of the resonant part of the amplitude on $P$ and $\Sigma$ persists up to significantly higher energies than was the case for the unpolarized cross section.

**Beam-recoil asymmetries.** In Fig. 4.15, we show our predictions for the double-polarization observables $C_x$ and $C_z$ [59] for the $K^+\Sigma^0$ final state. As in $\Lambda$ production, the obtained result depends strongly on the background and resonance choices. Quite surprisingly, the pure background models 3 and 4 perform as well in reproducing $C_x$ and $C_z$ as their full RPR counterparts. We take this to signify that the dataset employed in the fitting procedure is insufficiently discriminative with respect to the models' resonance content, because it solely consists of unpolarized and singly-polarized data. Including the data for $C_x$ and $C_z$ in the fitting procedure should be the logical next step toward refining the existing models.

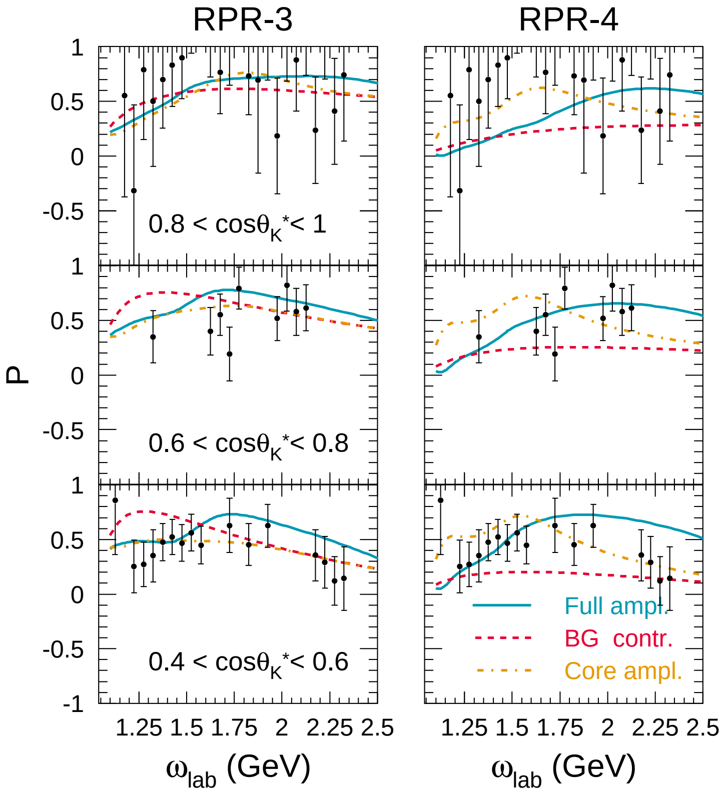

**Figure 4.11** Energy dependence of the $p(\gamma, K^+)\Sigma^0$ recoil polarization for those bins of $\cos\theta^*_K$ considered in the fitting procedure. Line conventions are as in Fig. 4.10. The data are from CLAS [57].

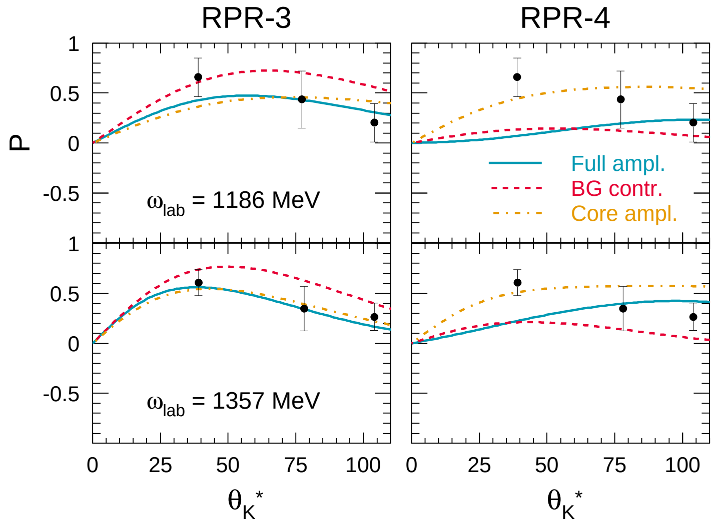

**Figure 4.12** Angular dependence of the forward-angle $p(\gamma, K^+)\Sigma^0$ recoil polarization for two of the energy bins covered by the GRAAL experiment. Line conventions are as in Fig. 4.10. The data are from [63].

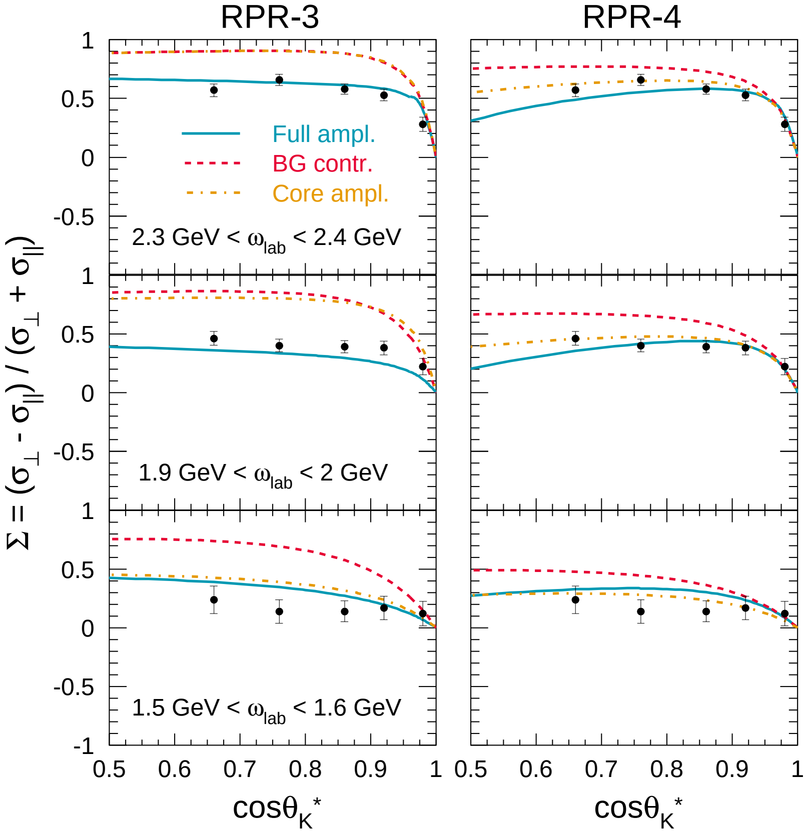

**Figure 4.13** Results for the forward-angle $p(\gamma, K^+)\Sigma^0$ photon beam asymmetry, for three representative bins of $\omega_{lab}$, corresponding to center-of-mass energy bins 2.28 GeV $< W <$ 2.32 GeV, 2.11 GeV $< W <$ 2.15 GeV, and 1.92 GeV $< W <$ 1.97 GeV. Line conventions are as in Fig. 4.10. The data are from LEPS [61].

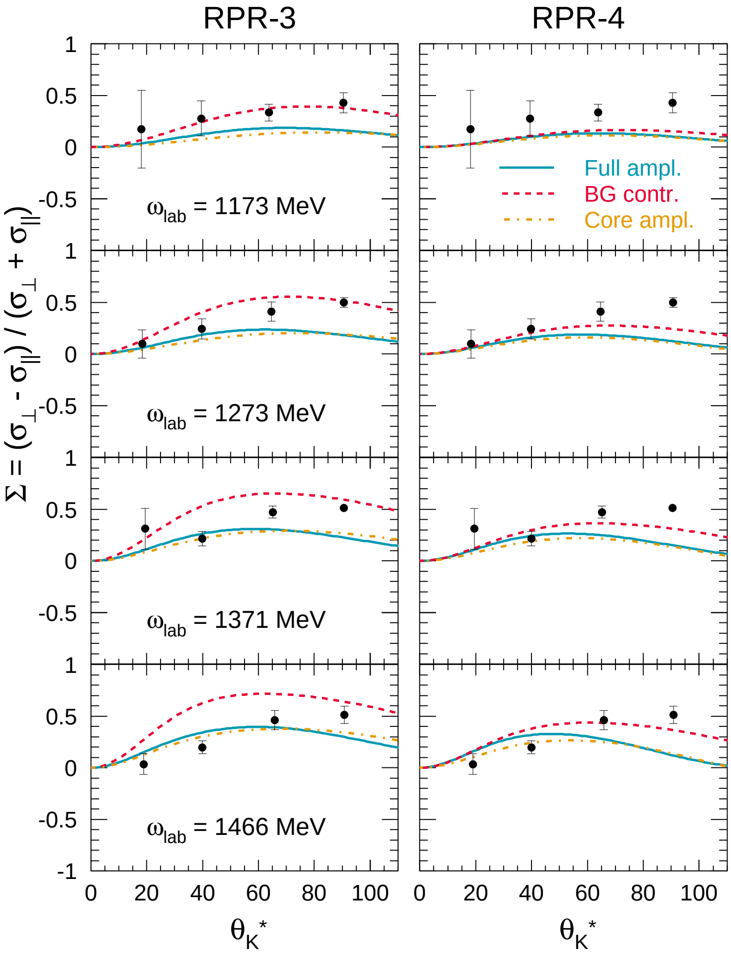

**Figure 4.14** Angular dependence of the forward-angle $p(\gamma, K^+)\Sigma^0$ photon beam asymmetry for four of the energy bins covered by the GRAAL experiment. Line conventions are as in Fig. 4.10. The data are from [63].

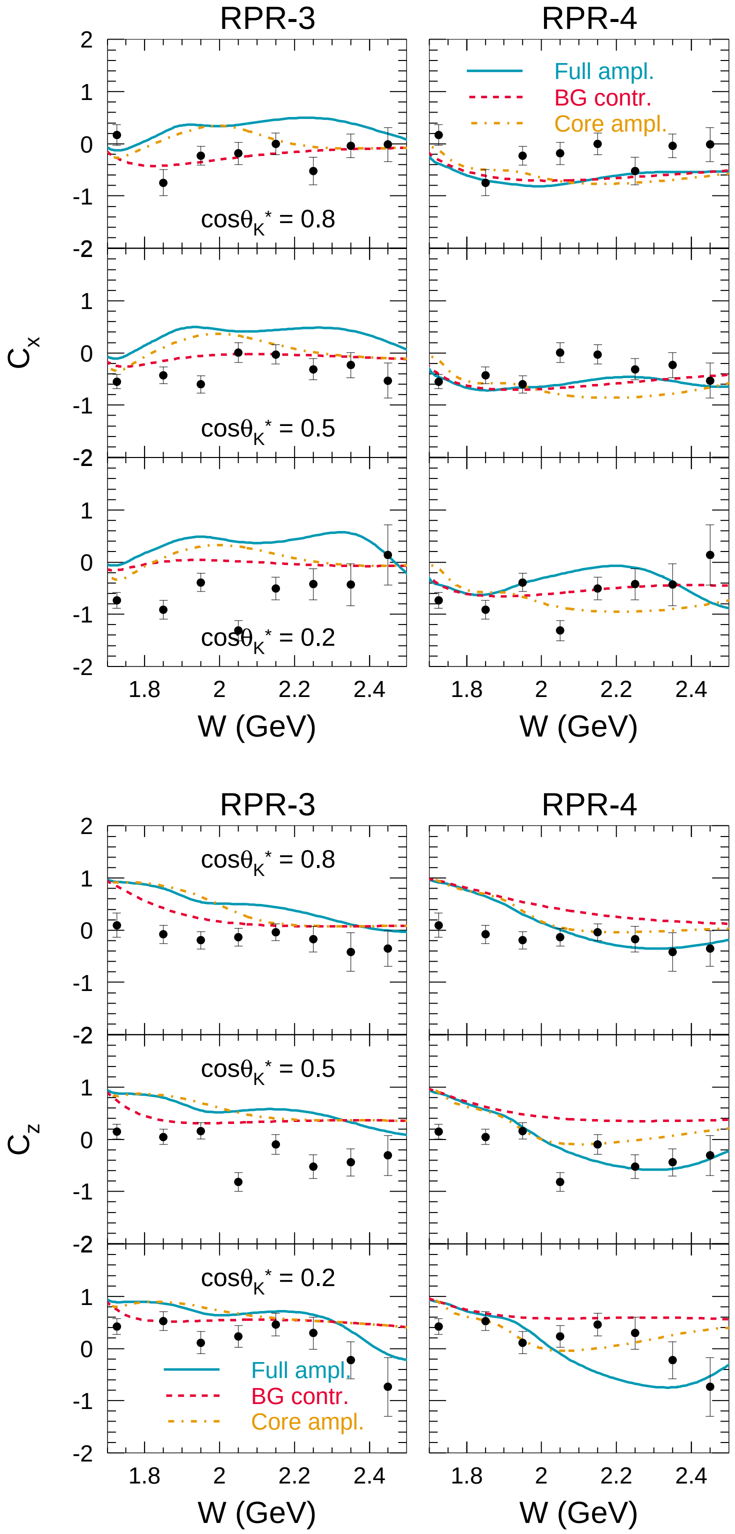

**Figure 4.15** Energy dependence of the $p(\gamma, K^+)\Sigma^0$ double polarization asymmetry observables $C_x$ (top) and $C_z$ (bottom), for three of the energy bins covered by CLAS. Line conventions are as in Fig. 4.1. The data are from CLAS [59].

### The $K^0\Sigma^+$ channel

**Differential cross section.** The differential cross section, displayed in Fig. 4.16, is quite well reproduced. As explained in Sec. 3.2.2, the good performance of the background models in this channel hinges entirely on the inclusion of the $K^*(1410)$ trajectory. Specifically, this trajectory provides the necessary destructive interference to counteract the sharp rise of the cross section with energy, brought about by the $K^*(892)$ contribution (Fig. 3.8). At the most forward kaon angles, the computed cross sections exhibit a brief increase around 2.5 GeV, not observed in the data, before dipping back down to meet their high-energy values (Fig. 3.11). For $0.0 \lessapprox \cos\theta_K^* \lessapprox 0.6$, the measured behavior of the cross sections is well reproduced by both the RPR-3 and RPR-4 models.

**Recoil asymmetry.** In Fig. 4.17, the $p(\gamma, K^0)\Sigma^+$ recoil asymmetry is presented. Because only four data points are available for $\cos\theta_K^* > 0$, this result may in fact be regarded as a prediction. The background contribution equals zero because of the constant phase assumed for the $K^*(892)$ and $K^*(1410)$ trajectories, which are the only ingredients of the Regge model in the $K^0\Sigma^+$ channel. Real propagators for $K^*(892)$ and $K^*(1410)$ result in a real amplitude, and since $P$ is related to the amplitude's imaginary part, it vanishes for this background choice. The RPR-3 model provides a slightly better overall description of $P$.

Based on the above results, one should conclude that the $p(\gamma, K)\Sigma$ data do not allow to distinguish between the RPR-3 and RPR-4 model variants, i.e. between the positive or negative sign for $G^t_{K^*(892)}$. It will be shown in the next chapter that the $K^+\Sigma^0$ electroproduction observables are considerably more discriminative in this respect.

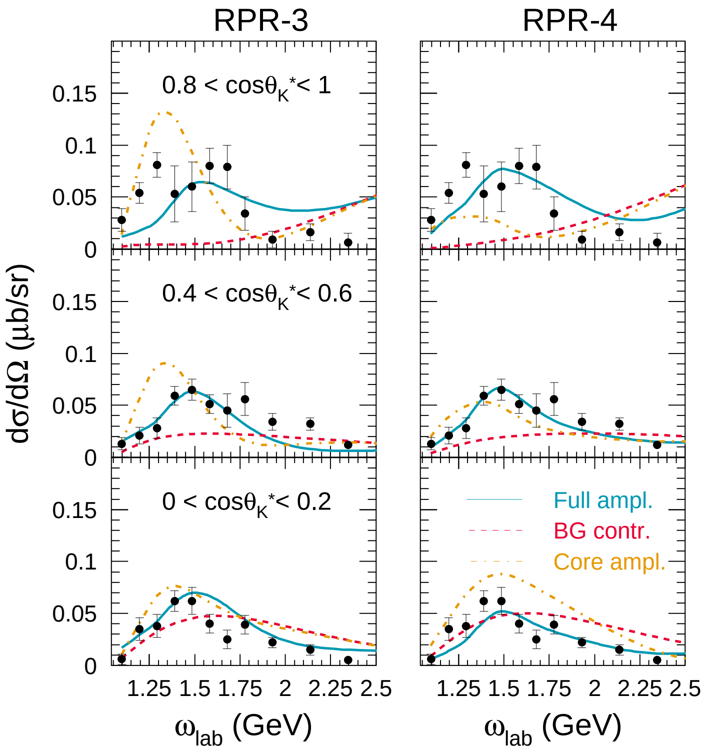

**Figure 4.16** Energy dependence of the differential $p(\gamma, K^0)\Sigma^+$ cross sections in the resonance region, for a number of representative bins in $\cos\theta^*_K$. Line conventions are¡ as in Fig. 4.10. The data are from SAPHIR [64].

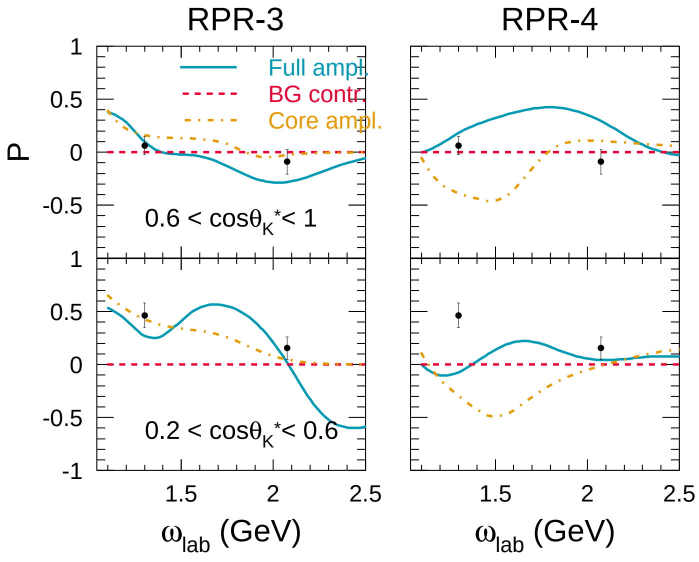

**Figure 4.17** Energy dependence of the $p(\gamma, K^0)\Sigma^+$ recoil polarization for those bins of $\cos\theta^*_K$ considered in the fitting procedure. Line conventions are as in Fig. 4.10. The data are from SAPHIR [64].

CHAPTER

5

# KY electroproduction in the resonance region

Before the CLAS collaboration released its first KY electroproduction results in 2003 [65, 66], the world $p(\gamma^{(*)}, K)Y$ database was made up almost exclusively of photoproduction observables. Consequentially, most theoretical models developed in the 1980s and 1990s applied to real photons only. Even in recent years, relatively little progress has been made in further developing the electroproduction models on the market [25, 26, 131, 132]. As was shown by Janssen *et al.*, however, even a small set of $p(e, e'K^+)Y$ datapoints can yield important insights and tight constraints on the KY production dynamics [133]. With the release of new high-precision $p(e, e'K^+)\Lambda, \Sigma^0$ data by the CLAS collaboration [67] earlier this year, we are in a unique position to further explore this conjecture in the context of the RPR approach.

As a combined coupled-channels analysis of $p(\gamma, K)Y$ and $p(e, e'K)Y$ has not yet been realized, a tree-level model currently represents the best possibility of studying both reactions in the same framework. Remarkably, the new CLAS data appear to favor a reggeized description of the $p(e, e'K^+)Y$ processes. In particular, Ref. [67] demonstrates that the Regge model of Guidal [40] describes the data consistently better than the isobar models of both Janssen [133] and Mart [28]. Although the reasonable performance of the pure Regge description for most observables suggests a $t$-channel dominated process, there are obvious discrepancies between the Regge predictions and the data, indicative of $s$-channel dynamics. The RPR approach represents an ideal framework to parameterize these contributions.

In what follows, we will employ the RPR model variants from Chapter 4 to obtain predictions for the $p(e,e'K^+)\Lambda,\Sigma^0$ processes. Hereby, the electromagnetic form factors of the intermediate $N^*$s and $\Delta^*$s will be computed in the Bonn constituent-quark model [12, 45]. With this input, it turns out that a reasonable description of the data can be obtained without adding or readjusting any parameters. We will show that the electroproduction response functions are extremely useful for fine-tuning both the background and resonant contributions to the RPR amplitudes. A selection of results was earlier presented in Refs. [134] and [135].

## 5.1 The RPR amplitude at finite $Q^2$

In this work, it will be assumed that the photo- and electroinduced $KY$ production processes can be described by the same type of reaction amplitudes. Under this condition, extrapolating a photoproduction model to finite values of $Q^2$ simply involves modifying each EM coupling with a suitable electromagnetic form factor (EMFF). While results from past analyses [25, 26, 131–133] support such a course of action, it is an approximate solution. For example, the inelastic EM vertex for coupling to a spin-$1/2$ resonance acquires an extra longitudinal contribution ($\sim \gamma^\mu \varepsilon_\mu$) when an off-shell photon is involved [83]. When explicitly including this term in the electroproduction calculations, knowledge of both the strong and EM couplings $g_{KYR}$ and $\kappa_{pR}$ is required, whereas the photoproduction description solely depends on the product $g_{KYR} \cdot \kappa_{pR}$. A comparable situation occurs for the EM coupling to spin-$3/2$ states.

We start out from the RPR photoproduction amplitudes constructed in Chapter 4. So far, the different model variants have been judged nearly exclusively by their ability to reproduce the data to which they were fitted. However, the *likelihood* of a theoretical description is not solely determined by its adequacy to describe the data, but also by the number of free parameters and stability of the minimum-$\chi^2$ solution [125]. An alternative measure of a model's likelihood is its potential to predict observables not included in the fit. The recent $p(e,e'K^+)Y$ data from CLAS [67] provide a good opportunity to subject the predictive power of the RPR model to a stringent test. As a first step, we will determine the necessary background and resonant EMFFs with which to modify the EM couplings (Secs. 5.1.1 and 5.1.2). Then, we will compare the RPR variants from the previous chapter with the electroproduction observables *without* adding or readjusting any parameters (Sec. 5.2). Since no $p(e,e'K^0)\Sigma^+$ data are available at this point, we focus our analysis on the $K^+\Lambda$ and $K^+\Sigma^0$ final states.

### 5.1.1 Background contributions

When applying the Gross-Riska procedure to ensure gauge invariance for the electroproduction amplitude (Sec. 2.3.3), three different EMFFs can be assumed at the $\gamma^* K^+ K^+$, $\gamma^* K^+ K^{*+}$, and $\gamma^* pp$ vertices:

$$\begin{aligned} \mathcal{M}_{\text{Regge}}(\gamma^* p \to K^+ \Lambda) = & \\ & \mathcal{M}_{\text{Regge}}^{K^+} F^{K^+}(Q^2) + \mathcal{M}_{\text{Regge}}^{K^{*+}(892)} F^{K^{*+}(892)}(Q^2) \\ & + \mathcal{M}_{\text{Feyn}}^{p,\text{elec}} F_1^p(Q^2) \times \mathcal{P}_{\text{Regge}}^{K^+} \times (t - m_{K^+}^2)\,, \end{aligned} \tag{5.1}$$

where $F_1^p$ is the proton Dirac form factor, corresponding to the electric part of the vertex (see Appendix A.1). However, it has been shown by Guidal and Vanderhaeghen that the measured $Q^2$ behavior of the $\sigma_L/\sigma_T$ ratio can only be reproduced provided that the same form factor is used at the $\gamma^* pp$ and $\gamma^* K^+ K^+$ vertices [37]:

$$F_1^p(Q^2) \equiv F_{K^+}(Q^2)\,, \tag{5.2}$$

a result which is confirmed by our calculations. Since the $s$-channel electric Born term of Eq. (5.1) is essentially an artefact of the gauge-breaking nature of the $K^+$-exchange diagram, this is not only the simplest, but also the most natural way to guarantee current conservation.

For the $K^+(494)$ and $K^{*+}(892)$ trajectories, a monopole EMFF

$$F_{K^+}(Q^2) = \frac{1}{1 + Q^2/\Lambda_{K^+}^2}\,, \quad F_{K^+K^{*+}}(Q^2) = \frac{1}{1 + Q^2/\Lambda_{K^{*+}}^2} \tag{5.3}$$

is assumed, with $\Lambda_{K^+} = \Lambda_{K^{*+}} = 1300$ MeV, in accordance with Refs. [39, 40]. The cutoff values were chosen to optimally match the behavior of the electroproduction data for $Q^2 \gtrsim 2.5$ GeV$^2$ [66], where the resonant contributions are expected to fade more quickly than the $t$-channel background terms.

### 5.1.2 Resonance form factors and the Bonn model

While some experimental information regarding resonant EMFFs is available, little of it applies to the mass region of interest to kaon production ($m_R \gtrsim 1.6$ GeV). For this reason, most theoretical descriptions of $p(e, e'K)Y$ opt for a phenomenological dipole parameterization for the EMFFs of the resonant diagrams [25, 26, 131, 132]. However, it is our opinion that the degree of arbitrariness in the $p(e, e'K^+)Y$ description can be considerably reduced by using computed EMFFs instead of the standard dipole shape. Therefore, we calculate the EMFFs of the contributing $N^*$ and $\Delta^*$ states within a covariant constituent-quark model (CQM), developed by the Bonn group [45, 136–139].

As the Bonn CQM contains a mere seven parameters, all of which have been fitted to the baryon spectrum [12], the computation of the EMFFs is parameter-free. It has been shown that the Bonn EMFF results compare favourably to the existing data for the low-lying $N^*$ and $\Delta^*$ states [45].

The Bonn CQM does not provide direct access to the form factors themselves, but rather to matrix elements of the EM current operator:

$$\langle\, R\,(P'), \lambda' \mid J_\mu(0) \mid p\,(P), \lambda \,\rangle\ . \tag{5.4}$$

Herein, $P, \lambda$ and $P', \lambda'$ are the four-momenta and helicities of the proton $p$ and resonance $R$ involved in the transition. $J_\mu(0)$ is related to the $\gamma^* pR$ interaction Lagrangian through

$$\langle\, R\,(P'), \lambda' \mid \mathcal{L}_{\gamma^* pR}(x) \mid p\,(P), \lambda \,\rangle = e^{i(P'-P)x}\, \langle\, R\,(P'), \lambda' \mid J_\mu(0)\, A^\mu(x) \mid p\,(P), \lambda \,\rangle\,. \tag{5.5}$$

While many current matrix elements (CMEs) of the type (5.4) can be written down, only a limited number of them are independent. It turns out that there are two independent CMEs if $R$ is a spin-1/2 resonance, and three for a spin-3/2 state. A possible choice is:

$$\mathcal{M}^{+}_{\frac{1}{2},-\frac{1}{2}} = \left\langle\, R\,(P'),\, \frac{1}{2} \,\middle|\, J_1(0) + i\, J_2(0) \,\middle|\, p\,(P),\, -\frac{1}{2} \,\right\rangle\ , \tag{5.6}$$

$$\mathcal{M}^{+}_{\frac{3}{2},\frac{1}{2}} = \left\langle\, R\,(P'),\, \frac{3}{2} \,\middle|\, J_1(0) + i\, J_2(0) \,\middle|\, p\,(P),\, \frac{1}{2} \,\right\rangle\ , \tag{5.7}$$

$$\mathcal{M}^{0}_{\frac{1}{2},\frac{1}{2}} = \left\langle\, R\,(P'),\, \frac{1}{2} \,\middle|\, J_0(0) \,\middle|\, p\,(P),\, \frac{1}{2} \,\right\rangle\ . \tag{5.8}$$

where $M^{+}_{\frac{3}{2},\frac{1}{2}}$ only exists if $R$ has a spin of 3/2 or larger. The CMEs from Eqs. (5.6)-(5.8), which are usually modified with an appropriate kinematical factor, are commonly referred to as the *helicity amplitudes* (HAs) of the EM transition. When calculating HAs using the current derived from a particular $\mathcal{L}_{\gamma^* pR}$, one obtains a system of linear equations relating the HAs to the EMFFs. In order for this system to have a solution, the number of EMFFs should equal the number of HAs. Strangely enough, this condition does not seem to be met, as we assume only one EMFF for a spin-1/2 resonance and two for a spin-3/2 state, i.e. one less than the number of HAs. It should be realized, though, that the Lagrangians (A.12) and (A.13) from Appendix A.1 do not represent the most general form of the interactions. As mentioned in the introduction to Sec. 5.1, the Lagrangians for the spin-1/2 and -3/2 states also contain a longitudinal part, which vanishes at $Q^2 = 0$ and has been neglected in our calculations. The full interactions are given by [82]:

$$\begin{aligned}\mathcal{L}_{\gamma^* pR(1/2^\pm)} =& - e\, F_1^{pR(1/2^\pm)}(Q^2)\;\overline{R}\Gamma_\mu N A^\mu \\ &+ \frac{e\kappa_{pR(1/2^\pm)}}{4m_p}\, F_2^{pR(1/2^\pm)}(Q^2)\;\overline{R}\Gamma_{\mu\nu} N F^{\mu\nu} + \text{h.c.}\,, \end{aligned} \tag{5.9}$$

$$\begin{aligned}\mathcal{L}_{\gamma pR(3/2^\pm)} =&\; i\,\frac{e\kappa^{(1)}_{pR(3/2^\pm)}}{m_R+m_p}\, F_{(1)}^{pR(3/2^\pm)}(Q^2)\;\overline{R}^\mu\theta_{\mu\nu}(Y)\,\Gamma'_\lambda N F^{\lambda\nu} \\ &- \frac{e\kappa^{(2)}_{pR(3/2^\pm)}}{(m_R+m_p)^2}\, F_{(2)}^{pR(3/2^\pm)}(Q^2)\;\overline{R}^\mu\theta_{\mu\nu}(X)\,\Gamma\,(\partial_\lambda N)\,F^{\nu\lambda} \\ &+ \frac{e\kappa^{(3)}_{pR(3/2^\pm)}}{(m_R+m_p)^2}\, F_{(3)}^{pR(3/2^\pm)}(Q^2)\;\overline{R}^\mu\theta_{\mu\nu}(V)\,\Gamma\, N\delta_\lambda F^{\nu\lambda} + \text{h.c}\,, \end{aligned} \tag{5.10}$$

with $\Gamma^\mu = \gamma^\mu\ (\gamma^5\gamma^\mu)$, $\Gamma^{\mu\nu} = \sigma^{\mu\nu}\ (\gamma^5\sigma^{\mu\nu})$, $\Gamma = \gamma^5\ (1)$, and $\Gamma'^\mu = \gamma^5\gamma^\mu(\gamma^\mu)$ for even (odd) parity resonances. $F^{\mu\nu}$ and $\theta_{\mu\nu}$ are defined in Appendix A.1. The $F_1^{pR(1/2^\pm)}$ term of Eq. (5.9) and the $F_{(3)}^{pR(3/2^\pm)}$ term of Eq. (5.10) are neglected in the $p(e,e'K)Y$ calculations. It is clear, however, that the full expressions should be used to derive the HA/EMFF relations. After a straightforward but tedious calculation, one finds the following expressions for the EMFFs of the non-longitudinal terms:

$$F_2^{pR(1/2)^\pm}(Q^2) = f_2^\pm(Q^2)/f_2^\pm(0)\,, \tag{5.11}$$

with

$$f_2^\pm(Q^2) = \frac{\mp 1}{Q^\pm\sqrt{Q^\mp}}\left[\frac{Q^2}{|\vec{p}|}\,\mathcal{M}^0_{\frac{1}{2},\frac{1}{2}} \mp \frac{m_R \pm m_p}{2}\,\mathcal{M}^+_{\frac{1}{2},-\frac{1}{2}}\right]. \tag{5.12}$$

Herein, $|\vec{p}|$ is the magnitude of the three-momentum of the proton in the rest frame of the decaying resonance $R$ (see Ref. [83]), given by

$$|\vec{p}| = \left[\left(\frac{m_p^2 + m_R^2 + Q^2}{2m_R}\right)^2 - m_p^2\right]^{\frac{1}{2}}\,, \tag{5.13}$$

and $Q^\pm = Q^2 + (m_R \pm m_p)^2$. The spin-3/2 EMFFs can be written as:

$$F_{(i)}^{pR(3/2^\pm)}(Q^2) = \frac{f_{(i)}^\pm(Q^2)}{f_{(i)}^\pm(0)} \quad (i = 1,2)\,, \tag{5.14}$$

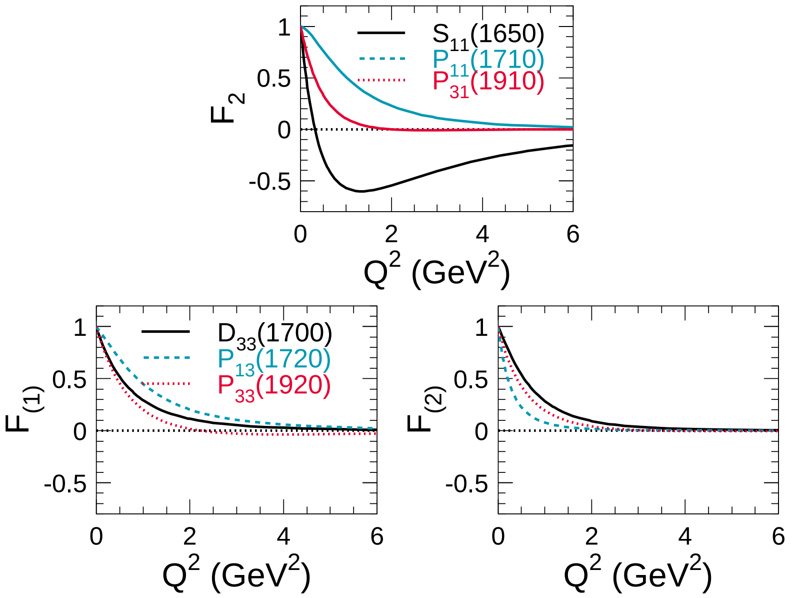

**Figure 5.1** Resonant EMFFs as computed in the Bonn CQM. The upper graph shows the Pauli EMFF for the electric $\gamma^* pR(1/2^{\pm})$ $(R = N^*, \Delta^*)$ interactions, whereas the lower two graphs contain the EMFFs needed in the $\gamma^* pR(3/2^{\pm})$ vertices.

with

$$f^{\pm}_{(1)}(Q^2) = \frac{1}{Q^{\pm}\sqrt{Q^{\mp}}} \left[\sqrt{3}\,\mathcal{M}^{+}_{\frac{1}{2},-\frac{1}{2}} \pm \mathcal{M}^{+}_{\frac{3}{2},\frac{1}{2}}\right], \tag{5.15}$$

$$\begin{aligned} f^{\pm}_{(2)}(Q^2) = & \frac{1}{(Q^{\pm})^{\frac{3}{2}}(Q^{\mp})^{\frac{5}{2}}} \left[-6Q^2\sqrt{Q^{\mp}}\,\mathcal{M}^{0}_{\frac{1}{2},\frac{1}{2}}\right. \\ & + 3\,\frac{m_p \mp m_R}{2m_R}\, Q^{\mp}\sqrt{Q^{\pm}}\,\mathcal{M}^{+}_{\frac{1}{2},-\frac{1}{2}} \\ & \left. \pm\sqrt{3}\,\frac{m_p m_R \mp m_p^2 \mp Q^2}{2m_R^2}\, Q^{\mp}\sqrt{Q^{\pm}}\mathcal{M}^{+}_{\frac{3}{2},\frac{1}{2}}\right]. \end{aligned} \tag{5.16}$$

Figure 5.1 displays the results for the $S_{11}(1650)$, $P_{11}(1710)$, $P_{13}(1720)$, $D_{33}(1700)$, $P_{31}(1910)$ and $P_{33}(1920)$ EMFFs as computed in the Bonn CQM. While most of the obtained curves resemble the standard dipole shape, the $S_{11}(1650)$ Pauli form factor exhibits an entirely different $Q^2$ dependence. As the computed form factors of the $P_{13}(1900)$ turned out to be too small, we used a dipole with a cutoff of 840 MeV [133] for this resonance. The same parameterization was adopted for the $S_{31}(1900)$, the mass of which is overestimated in all existing CQMs, and for the missing $D_{13}(1900)$ and $P_{11}(1900)$ states.

## 5.2 Results and discussion

In the previous chapter, we constructed RPR amplitudes for the various KY photoproduction channels. A number of model variants were found to provide a comparably good description of the available data. Their properties are recalled in Table 5.1.

As can be appreciated from Table 5.1, it turned out to be impossible to determine the sign of $G^t_{K^*(892)}$ from the photoproduction observables. Futhermore, in the $K^+\Lambda$ channel two combinations of K and $K^*(892)$ trajectory phases (rotating K and $K^*$, or rotating K and constant $K^*$) produce a comparable quality of agreement with experiment. With respect to the quantum numbers of a potential "missing" $N^*(1900)$ resonance, both $P_{11}$ and $D_{13}$ emerged as valid candidates, with $D_{13}$ the likelier of the two. For $K^+\Sigma^0$, the K and $K^*(892)$ trajectory phases could be fixed by the photoinduced data, and no "missing" resonances were needed to achieve a fair description of the data.

Without readjusting or tuning any parameter, we now compare the RPR variants from Table 5.1 with the electroproduction data.

### 5.2.1 The $\gamma p \to K^+\Lambda$ channel

In Fig. 5.2, we display the $Q^2$ dependence of the unseparated differential $p(e,e'K^+)\Lambda$ cross section $\sigma_T + \varepsilon\, \sigma_L$ and its separated components at $W = 2.15$ GeV. It is clear that

| | **RPR** | **Backgr.** | $D_{13}$ | $P_{11}$ | $\chi^2$ |
|---|---|---|---|---|---|
| $K^+\Lambda$ | RPR-2 | rot.K, rot.$K^*(892)$, $G^t_{K^*(892)} < 0$ | – | ★ | 3.2 |
| | RPR-2′ | " | ★ | – | 2.7 |
| | RPR-3 | rot.K, cst.$K^*(892)$, $G^t_{K^*(892)} > 0$ | – | ★ | 3.1 |
| | RPR-3′ | " | ★ | – | 3.2 |
| | RPR-4 | rot.K, cst.$K^*(892)$, $G^t_{K^*(892)} < 0$ | – | ★ | 3.1 |
| | RPR-4′ | " | ★ | – | 3.1 |
| $K^+\Sigma^0$ | RPR-3 | rot.K, cst.$K^*(892)$, $G^t_{K^*(892)} > 0$ | – | – | 2.0 |
| | RPR-4 | rot.K, cst.$K^*(892)$, $G^t_{K^*(892)} < 0$ | – | – | 2.0 |

**Table 5.1** RPR variants providing the best description of the high- and low-energy $p(\gamma,K^+)\Lambda$ and $p(\gamma,K^+)\Sigma^0$ data from Refs. [57,58,61,63,64,116,118,119]. "Rot." and "cst." refer to the rotating or constant Regge trajectory phase. All models include the known $S_{11}(1650)$, $P_{11}(1710)$, $P_{13}(1720)$ and $P_{13}(1900)$ resonances. Apart from these, each $K^+\Lambda$ variant assumes either a missing $D_{13}(1900)$ or $P_{11}(1900)$. The $K^+\Sigma^0$ amplitude further contains the $D_{33}(1700)$, $S_{31}(1900)$, $P_{31}(1910)$ and $P_{33}(1920)$ $\Delta^*$ states.

RPR-3$^{(\prime)}$ and RPR-4$^{(\prime)}$ are incompatible with the data for $\sigma_T$, for which they predict an unrealistically steep decrease as a function of $Q^2$. The RPR-2$^{(\prime)}$ variants, on the other hand, describe the slope of this observable rather well. As the $\sigma_T + \varepsilon\, \sigma_L$ and $\sigma_L$ data are accompanied by rather large error bars, they do not allow to distinguish between the different parameterizations.

Figure 5.3 shows the $Q^2$ dependence of the unseparated $p(e, e'K^+)\Lambda$ differential cross sections $\sigma_T + \varepsilon\, \sigma_L$ for three different $W$ bins. The RPR-3$^{(\prime)}$ variants underestimate the data by several factors, whereas RPR-2$^{(\prime)}$ and RPR-4$^{(\prime)}$ lead to acceptable results at all but the lowest energy.

The separated observables $\sigma_L$ and $\sigma_T$ are shown in Fig. 5.4 as a function of $\cos\theta_K^*$. The longitudinal cross section is clearly the least sensitive to the specific structure of the amplitude, with only the RPR-4$^{(\prime)}$ variants failing to reproduce its behavior at higher energies. The transverse cross section is more difficult to describe, as none of the six model variants are able to reproduce its magnitude at forward angles and $W \approx 1.75$ GeV. At higher energies, the RPR-2$'$ variant with a missing $D_{13}(1900)$ performs reasonably, as do both RPR-3 and RPR-3$'$. The latter two were, however, excluded by comparison with the unseparated data (Fig. 5.3).

Figure 5.5, which shows the $\cos\theta_K^*$ dependence of $\sigma_T + \varepsilon\, \sigma_L$, as well as of the previously unmeasured observables $\sigma_{TT}$ and $\sigma_{LT}$, supports the above conclusions. The RPR-2$'$ variant reasonably reproduces the trends of the data, including the strong forward-peaking behavior of the unseparated cross section. The differences between the full RPR-2$'$ (dashed lines) and background (dotted lines) curves are relatively small. The RPR-2 option with a missing $P_{11}$ leads to very poor results for $\sigma_T + \varepsilon\, \sigma_L$ and $\sigma_{TT}$. The RPR-4$^{(\prime)}$ results also deviate strongly from the data, as was the case for Fig. 5.4.

We further consider the transferred polarization for the $\vec{e}p \to e'K\vec{\Lambda}$ process. Figure 5.6 compares our results for the observables $P'_x$, $P'_z$, $P'_{x'}$ and $P'_{z'}$, obtained with the RPR-2 and RPR-2$'$ variants, to the data of Ref. [65]. Once more the RPR-2 model, corresponding to the $P_{11}(1900)$ option, leads to inferior results. The RPR-2$'$ variant with a missing $D_{13}$ provides a fair description of the data.

Based on the above results, the RPR-2$'$ model clearly represents the optimum choice for describing the combined photo- and electroproduction processes. This result supports the recent conclusion from Refs. [35,85] that a $D_{13}$ state with a mass around 1900 MeV is required by both the CLAS and SAPHIR $p(\gamma, K^+)\Lambda$ data.

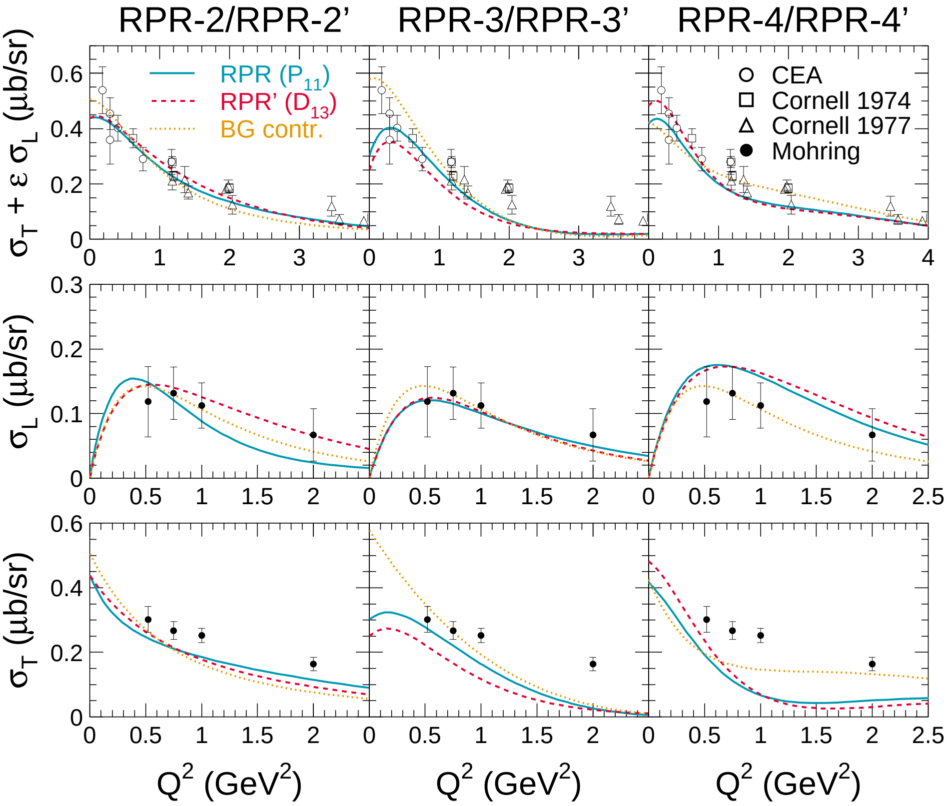

**Figure 5.2** $Q^2$ dependence of the unseparated and separated differential cross sections for the $K^+\Lambda$ final state, using the six RPR model variants from Table 5.1. The data for $\sigma_T + \varepsilon\sigma_L$ were taken at $W \approx 2.15$ GeV and $\theta_K^* \approx 0$, and those for $\sigma_L$ and $\sigma_T$ at $W \approx 1.84$ GeV and $\theta_K^* \approx 8$ deg. The data are from [66,68–70].

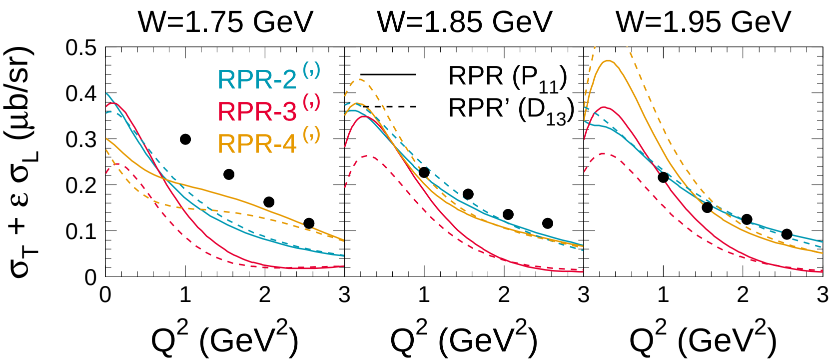

**Figure 5.3** $Q^2$ dependence of the unseparated differential cross section $\sigma_T + \varepsilon\, \sigma_L$ for the $K^+\Lambda$ final state at $\cos\theta_K^* = 0.9$, using the six RPR model variants from Table 5.1. The data are from [67].

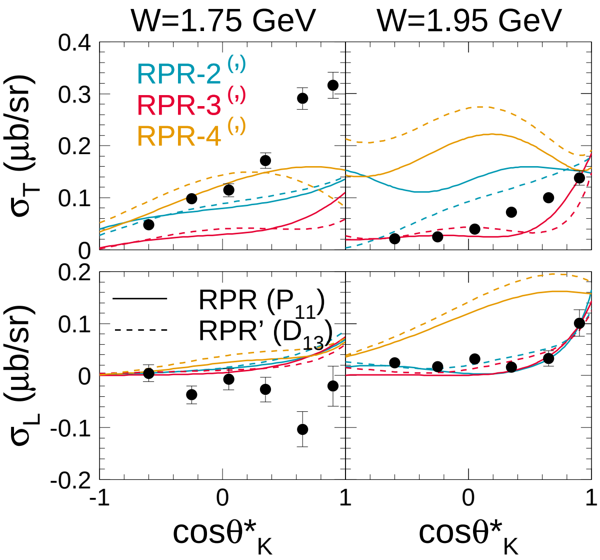

**Figure 5.4** $\cos\theta^*_K$ dependence of the separated differential cross sections $\sigma_L$ and $\sigma_T$ for the $K^+\Lambda$ final state at $Q^2 = 1.0$ GeV$^2$, using the six RPR model variants from Table 5.1. The data are from [67].

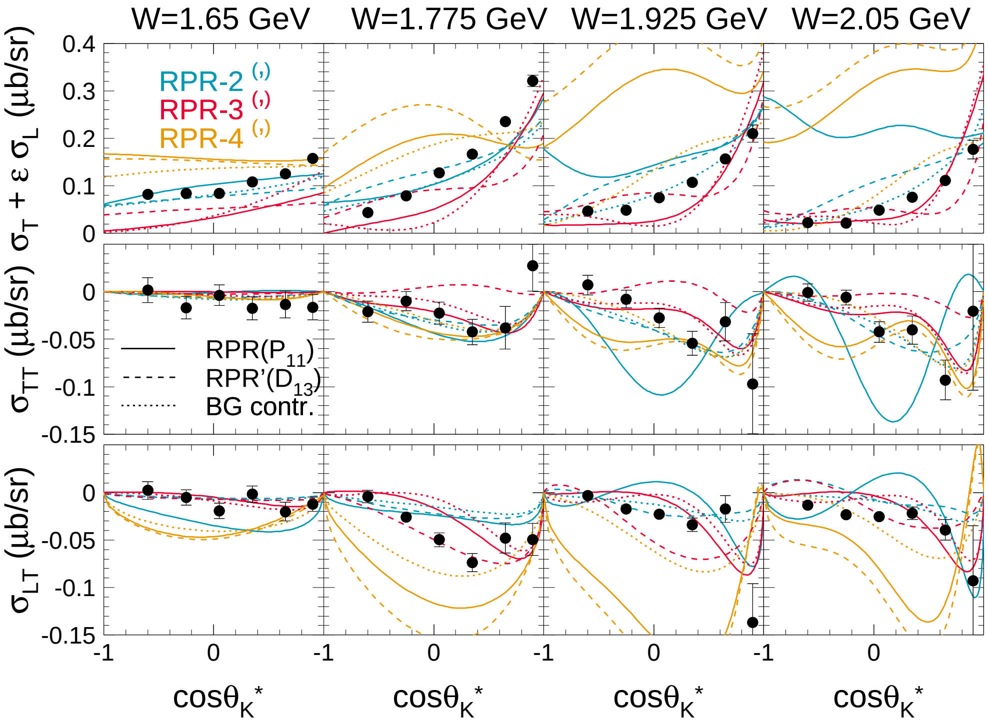

**Figure 5.5** $\cos\theta^*_K$ dependence of the differential cross sections $\sigma_T + \varepsilon\,\sigma_L$, $\sigma_{TT}$ and $\sigma_{LT}$ for the $K^+\Lambda$ final state at $Q^2 = 0.65$, using the six RPR model variants from Table 5.1. The dotted lines indicate the background contribution. The data are from [67].

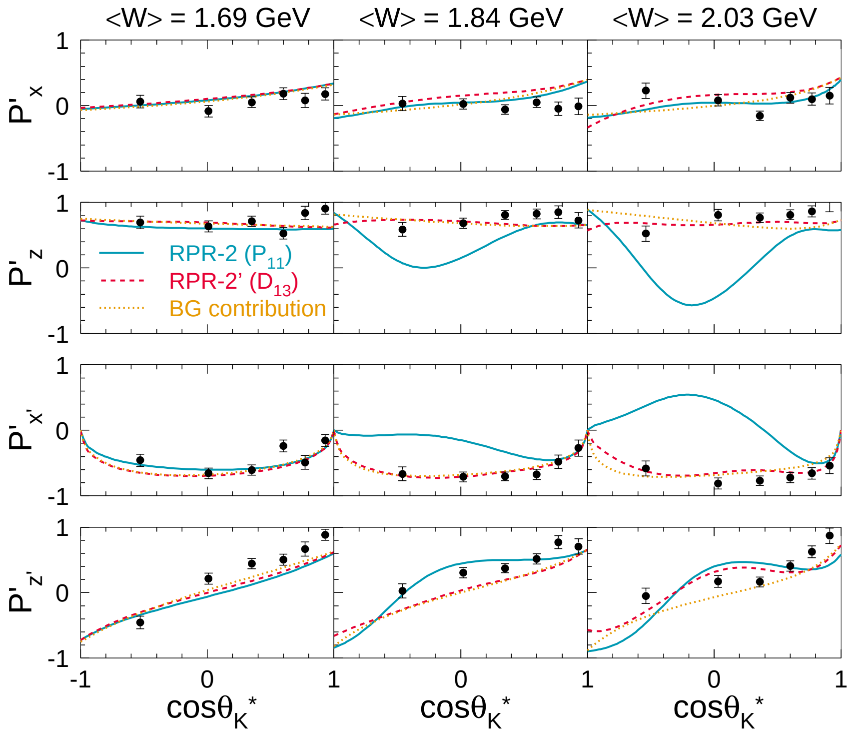

**Figure 5.6** Transferred polarization components $P'_x$, $P'_z$, $P'_{x'}$ and $P'_{z'}$ for the $K\Lambda$ final state as a function of $\cos\theta^*_K$ for $W \approx 1.69$, 1.84 and 2.03 GeV, for the RPR-2 and RPR-2′ variants from Table 5.1. Line conventions as in Fig. 5.2 (left panel). The data are from [65].

### 5.2.2 The $\gamma p \longrightarrow K^+\Sigma^0$ channel

For the $p(e,e'K^+)\Sigma^0$ process, only unpolarized data are available. In Fig. 5.7, the separated and unseparated cross sections are compared with the results of the RPR-3 and RPR-4 model variants from the lower part of Table 5.1. Neither $\sigma_T + \varepsilon\,\sigma_L$ nor its separated components exhibit a clear preference for either parameterizarion. It turns out that $\sigma_T + \varepsilon\sigma_L$ and $\sigma_L$ can be reasonably well described in a pure background model, whereas reproducing the slope of $\sigma_T$ clearly requires some resonant contributions to the amplitude.

The situation is different for the newly measured observables $\sigma_{TT}$ and $\sigma_{LT}$, displayed in Fig. 5.8 along with the unseparated cross section. It is clear that RPR-3 performs significantly better than RPR-4 in reproducing the global characteristics of the data. The quality of agreement is, however, considerably worse than for the $K^+\Lambda$ final state, although the absence of any forward peaking of $\sigma_T$+$\varepsilon$ $\sigma_L$ is qualitatively reproduced. In contrast to the RPR-2′ model for the $p(e,e'K^+)\Lambda$ reaction (Fig. 5.5), we find relatively large contributions beyond the background for both $K^+\Sigma^0$ models, hinting that the

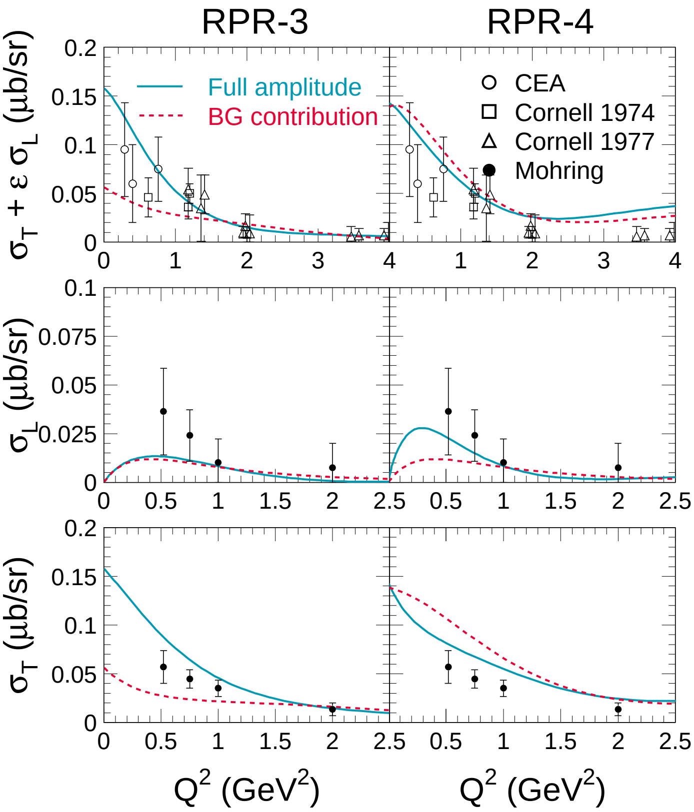

**Figure 5.7** $Q^2$ dependence of the unseparated and separated differential cross sections for the $K^+\Sigma^0$ final state. The data for $\sigma_T + \varepsilon\sigma_L$ were taken at $W \approx 2.15$ GeV and $\theta^*_K \approx 0$, and those for $\sigma_L$ and $\sigma_T$ at $W \approx 1.84$ GeV and $\theta^*_K \approx 8$ deg. Results of the RPR-3 and RPR-4 variants from Table 4.4 are displayed. The dashed curves correspond to the Regge background. The data are from [66, 68–70].

$p(e, e'K^+)\Sigma^0$ channel is more likely to provide interesting resonance information.

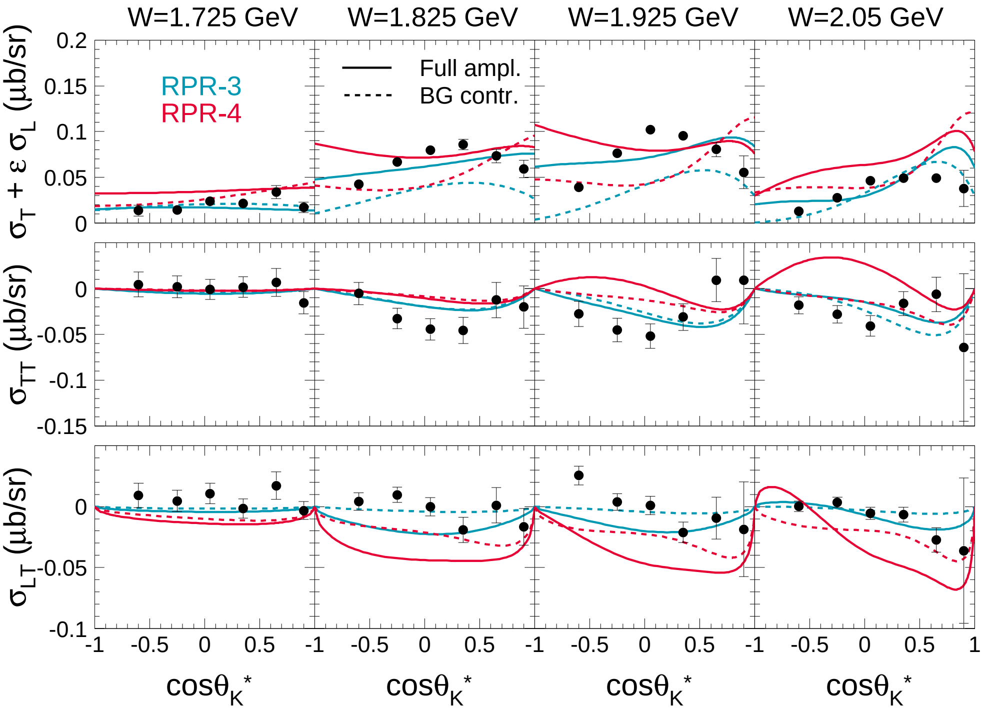

**Figure 5.8** $\cos\theta_K^*$ dependence of the differential cross sections $\sigma_T + \varepsilon\,\sigma_L$, $\sigma_{TT}$ and $\sigma_{LT}$ for the $K^+\Sigma^0$ final state at $Q^2 = 0.65$, using the two RPR model variants from Table 5.1 and their respective background contributions (dashed lines). The data are from [67].

CHAPTER

6

# Conclusions

We have presented an effective-Lagrangian framework describing the $p(\gamma, K)Y$ and $p(e, e'K)Y$ processes over an energy range from threshold up to $\omega_{lab} = 16$ GeV. To construct the reaction amplitudes, we have resorted to a "Regge-plus-resonance" (RPR) strategy, involving the superposition of a limited number of $s$-channel resonances onto a reggeized $t$-channel background. The Regge-inspired approach guarantees an appropriate high-energy limit of the model, while the $s$-channel terms provide the necessary resonant structure to the low-energy observables.

### Photoproduction in the Regge limit

In a first step, the parameters of the $t$-channel background amplitude were fixed against the $p(\gamma, K^+)\Lambda, \Sigma^0$ data for $\omega_{lab} \gtrsim 5$ GeV. The $K^+\Lambda$ and $K^+\Sigma^0$ photoproduction reactions were assumed to be dominated by $K$ and $K^*(892)$ Regge-trajectory exchanges. We addressed the question of whether a constant or a rotating phase represents the optimum choice for these trajectories.

For the $K^+\Lambda$ final state, the option of a constant $K$-trajectory phase could be ruled out by comparison with the high-energy recoil asymmetry data. Despite the parameter-poorness of the Regge amplitude, singling out one particular $p(\gamma, K^+)\Lambda$ background model turned out to pose some difficulties due to the scarcity of the high-energy data. Specifically, it proved impossible to determine either the sign of the $K^*(892)$ tensor coupling or the phase of the $K^*(892)$ trajectory.

In the $K^+\Sigma^0$ case, the amount of high-energy data is too limited to constrain the model parameters adequately. We adopted the strategy of retaining only those Regge model variants reproducing the sign of the recoil asymmetry in the resonance region. By imposing this requirement, the option of a constant K-trajectory phase could again be ruled out. As in the $K^+\Lambda$ case, the $K^*(892)$ phase and the sign of its tensor coupling remained undetermined.

In principle, isospin considerations allow one to transform the $K^+\Sigma^0$ photoproduction amplitude into an amplitude applicable to the $\gamma p \to K^0\Sigma^+$ process. Because the $K^0$-exchange diagram vanishes in photoproduction, the $K^0\Sigma^+$ amplitude constructed in this manner would solely comprise $K^*(892)$ exchange. Such a single-trajectory model was found to overshoot the $p(\gamma, K^+)\Sigma^0$ data in the resonance region by several factors. This could be explained by realizing that, with one of the leading t-channel contributions missing, higher-mass kaon trajectories are expected to start playing a role. Including the exchange of an additional $K^*(1410)$ trajectory was found to lead to very good results. Due to the lack of high-energy $p(\gamma, K^0)\Sigma^+$ data, the $K^*(1410)$ parameters and trajectory phase had to be determined against the resonance-region data.

### Photoproduction in the resonance region

In a second step, we added $s$-channel diagrams to the reggeized background amplitudes. In order to minimize any double-counting effects that might arise, the number of resonances was deliberately constrained. Apart from the well-established $S_{11}(1650)$, $P_{11}(1710)$ and $P_{13}(1720)$ nucleon resonances, we investigated possible contributions of the two-star $P_{13}(1900)$ state, as well as of the $\Delta^*$s $S_{31}(1900)$, $P_{31}(1910)$, $D_{33}(1700)$ and $P_{33}(1920)$. In the $K^+\Lambda$ channel, the missing $D_{13}(1900)$ and $P_{11}(1900)$ states were also considered as possible resonance candidates.

For the $p(\gamma, K^+)\Lambda$ process, we tentatively identified a single RPR model as providing the best description of the collective high- and low-energy data. A rotating phase was found to be the optimum choice for both the $K(494)$ and $K^*(892)$ trajectories. The optimum sign for the $K^*(892)$ tensor coupling turned out to be the negative one. It was further shown that the description of the resonance-region observables could be significantly improved by including a contribution from a new resonance. A missing resonance with the quantum numbers $D_{13}(1900)$ was found to be compatible with the data. The known spin-3/2 resonances $P_{13}(1720)$ and $P_{13}(1900)$ proved to be considerably more important than their spin-1/2 counterparts $S_{11}(1650)$ and $P_{11}(1710)$. This corroborates the result from Refs. [30, 33], in which the importance of $P_{11}(1710)$ was also called into question. Of all quantities measured so far, the double-polarization observables $C_x$ and $C_z$ are by far the most discriminative with respect to the RPR-model ingredients. Including these observables in the fitting procedure should be the next step toward refining the existing models.

For the $p(\gamma, K)\Sigma$ channels, the sign of the $K^*(892)$ tensor coupling turned out to be ill-determined by the photoproduction data. It was found that the $K^*(1410)$ phase has to match the choice made for $K^*(892)$. Apart from the standard $N^*$ "core" states $S_{11}(1650)$, $P_{11}(1710)$ and $P_{13}(1720)$, the two-star $P_{13}(1900)$ was identified as a necessary contribution, irrespective of the background assumptions. Including either of the spin-1/2 resonances $S_{31}(1900)$ or $P_{31}(1910)$ turned out to be sufficient, whereas the spin-3/2 $D_{33}(1700)$ state was found to be considerably more important than $P_{33}(1920)$.

### Electroproduction in the resonance region

Finally, we compared the various RPR amplitudes constructed for the photoproduction process with the world electroproduction data without readjusting any parameter. The electromagnetic form factors of the various $N^*$ and $\Delta^*$ states were computed using the Bonn constituent-quark model [45, 136, 139]. It was found that the $S_{11}(1650)$ Dirac form factor deviates rather strongly from the standard dipole shape. For the other resonances, a dipole-like behavior of the EMFF was obtained.

We concluded that the electroproduction response functions are particularly useful in constraining those RPR-model parameters which the $p(\gamma, K)Y$ data fail to determine. For $K^+\Sigma^0$ production, only one of the two RPR model variants retained from the photoproduction study could reasonably account for the electroproduction observables. The preferred model assumes a positive $K^*(892)$ tensor coupling. In the $K^+\Lambda$ channel, the model preferred from the photoproduction study also turned out to produce the best description of the electroproduction process.

Although the reasonable performance of the pure Regge description for most $p(e, e'K)\Lambda, \Sigma^0$ observables [67] suggests a t-channel dominated process, the discrepancies between the pure Regge predictions and the data are obvious footprints of s-channel dynamics. The RPR strategy provides an ideal framework to parameterize such contributions. While reasonable predictions could be obtained using the RPR models derived from the photoproduction study, we expect that a fit to the combined $p(\gamma, K^+)Y$ and $p(e, e'K^+)Y$ databases could provide even more useful information.

### Outlook

While a reasonable description of the forward-angle part of the $p(\gamma^{(*)}, K)Y$ database can be obtained with the RPR models presented here, there is room for improvement. With a view to future projects, it would be useful to extend the RPR amplitudes towards backward angles. A number of strategies may be followed in realizing this:

- a simple re-fitting of model parameters to the complete dataset.
- the assumption of saturating instead of linear Regge trajectories.
- the adding of $u$-channel contributions, either reggeized or not.

A logical next step would then be to incorporate the RPR approach into a coupled-channels model. Alternative applications of the RPR strategy could involve the description of $\rho$ or $K^*$ vector-meson production, of reactions involving a deuteron, or of the production of hypernuclei.

To conclude, a final word of warning may be in order. Despite the established success of effective-field approaches in describing a variety of meson production processes, it should be realized that pinpointing the dominant $s$-channel diagrams in the context of such a model is a delicate business. This applies in particular to the search for "missing" resonances. While the inclusion of additional resonant contributions invariably leads to a decrease in $\chi^2$, this does not automatically imply an increased likelihood for the constructed model. Furthermore, it is seldom clear whether a similar agreement with the data cannot be obtained using a different combination of background and resonance contributions, or a different set of parameters for the same diagrams. As the number of model parameters increases, it becomes ever harder to check whether the attained minimum in $\chi^2$ is truly a global minimum, and whether or not other such minima exist. Evidently, this challenge will prove even more daunting in coupled-channels models than at tree level. It will, however, have to be addressed carefully in future analyses of weak channels such as kaon photoproduction.

APPENDIX

# A

# Effective fields and interactions for $p(\gamma^{(*)}, K)Y$

## A.1 Effective Lagrangians in the RPR model

In this Appendix, we list the strong and electromagnetic interaction Lagrangians needed for the RPR calculations. We adopt the same set of interactions as in the work of S. Janssen [71]. The normalization conventions for the field operators and Dirac matrices are those of Ref. [140]. The nucleon and hyperon Dirac fields and the kaon Klein-Gordon field are written as $N$, $Y$ and $K$, and the notation $R$ is used for a general resonant baryon field. The antisymmetric tensor for the photon field $A^{\mu}$ is defined as $F^{\mu\nu} = \partial^{\nu}A^{\mu} - \partial^{\mu}A^{\nu}$. The corresponding tensor for the vector-meson field $V^{\mu}$ is given by $V^{\mu\nu} = \partial^{\nu}V^{\mu} - \partial^{\mu}V^{\nu}$. The Mandelstam variables for the two-particle scattering process $\gamma^{*}(k) + p(p) \rightarrow K(p_K) + Y(p_Y)$ are defined in the standard way as

$$s = (k + p)^2\,, \tag{A.1}$$

$$t = (k - p_K)^2\,, \tag{A.2}$$

$$u = (k - p_Y)^2\,, \tag{A.3}$$

with $s + t + u = m_p^2 + m_K^2 + m_Y^2 - Q^2$.

### A.1.1 Background contributions

The electromagnetic interaction Lagrangians contributing to the t-channel background amplitude are given by:

$$\mathcal{L}_{\gamma^* KK} = -ie\, F_K(Q^2)\, \left(K^\dagger \partial_\mu K - K\partial_\mu K^\dagger\right) A^\mu\,, \tag{A.4}$$

$$\mathcal{L}_{\gamma^* KK^*} = \frac{e\kappa_{KK^*}}{4M}\, F_{KK^*}(Q^2)\, \epsilon^{\mu\nu\lambda\sigma} F_{\mu\nu} V_{\lambda\sigma} K + \mathrm{h.\,c.}\,, \tag{A.5}$$

$$\mathcal{L}_{\gamma^* pp} = \underbrace{-e\, F_1^p(Q^2)\, \overline{N}\gamma_\mu N A^\mu}_{\mathcal{L}^{\mathrm{elec}}_{\gamma^* pp}} + \underbrace{\frac{e\kappa_p}{4m_p}\, F_2^p(Q^2)\, \overline{N}\sigma_{\mu\nu} N F^{\mu\nu}}_{\mathcal{L}^{\mathrm{magn}}_{\gamma^* pp}}\,, \tag{A.6}$$

with "h. c." denoting the hermitian conjugate. For the proton anomalous magnetic moment, we assume $\kappa_p = 1.793\ \mu_N$ [114], whereas $\kappa_{KK^*}$ is considered as a free parameter. Further, $\sigma_{\mu\nu} = \frac{i}{2}[\gamma_\mu, \gamma_\nu]$, and $e = +\sqrt{4\pi/137}$. By convention, the mass scale M is taken at 1 GeV. In the real-photon point, the electromagnetic form factors (EMFFs) reduce to

$$F_{K^+}(0) = F_{K^{+,0}K^{*+,0}}(0) = F^p_{1,2}(0) = 1\,, \tag{A.7}$$

$$F_{K^0}(0) = 0\,. \tag{A.8}$$

$F_1^p$ and $F_2^p$ are known as the proton Dirac and Pauli form factors, respectively. The electric contribution $\mathcal{L}^{\mathrm{elec}}_{\gamma^* pp}$ to Eq. (A.6) is included in the t-channel Regge amplitude for $K^+$ production in order to ensure gauge invariance. While the magnetic term $\mathcal{L}^{\mathrm{magn}}_{\gamma^* pp}$ is generally included in an isobar model, it is not needed for the RPR calculations.

For the strong KYp vertex, either a pseudoscalar or a pseudovector structure can be assumed. We have opted for a pseudoscalar interaction in accordance with Ref. [71]:

$$\mathcal{L}^{PS}_{KYp} = -ig_{KYp}\, K^\dagger\, \overline{Y}\gamma_5 N + \mathrm{h.\,c.} \tag{A.9}$$

The hadronic $K^*Yp$ vertex is composed of a vector (v) and a tensor (t) part:

$$\begin{aligned}\mathcal{L}_{K^*Yp} = &- g^v_{K^*Yp}\, \overline{Y}\gamma_\mu N V^\mu \\ &+ \frac{g^t_{K^*Yp}}{2\,(M_Y + M_p)}\, \overline{Y}\sigma_{\mu\nu} V^{\mu\nu} N + \mathrm{h.c.}\,.\end{aligned} \tag{A.10}$$

The free parameters in the background diagrams are expressed as

$$g_{KYp}\,, \quad G^{v,t}_{K^*} = \frac{e g^{v,t}_{K^*Yp}}{4\pi}\, \kappa_{KK^*}\,. \tag{A.11}$$

### A.1.2 Resonance contributions

The electromagnetic interaction Lagrangian for spin-1/2 resonances, assumed in this work, reads:

$$\mathcal{L}_{\gamma^* pR(1/2^\pm)} = \frac{e\kappa_{pR(1/2^\pm)}}{4m_p} F_2^{pR(1/2^\pm)}(Q^2)\ \overline{R}\Gamma_{\mu\nu}NF^{\mu\nu} + h.c.\,, \tag{A.12}$$

with $\Gamma^{\mu\nu} = \ \sigma^{\mu\nu}\ (\gamma^5\sigma^{\mu\nu})$ for even (odd) parity resonances. For spin-3/2 resonances, two terms appear in the Lagrangian:

$$\begin{aligned}\mathcal{L}_{\gamma pR(3/2^\pm)} = {} & i\,\frac{e\kappa^{(1)}_{pR(3/2^\pm)}}{m_R + m_p} F^{pR(3/2^\pm)}_{(1)}(Q^2)\ \overline{R}^\mu\theta_{\mu\nu}\left(Y_{R(3/2)}\right)\Gamma'_\lambda\, N\, F^{\lambda\nu} \\ & - \frac{e\kappa^{(2)}_{pR(3/2^\pm)}}{(m_R + m_p)^2} F^{pR(3/2^\pm)}_{(2)}(Q^2)\ \overline{R}^\mu\theta_{\mu\nu}\left(X_{R(3/2)}\right)\Gamma\left(\partial_\lambda N\right)F^{\nu\lambda} + h.c\,,\end{aligned} \tag{A.13}$$

Herein, $\Gamma = \gamma^5\ (1)$ and $\Gamma'^\mu = \ \gamma^5\gamma^\mu(\gamma^\mu)$ for even (odd) parity resonances. $R^\mu$ is the Rarita-Schwinger vector field used to describe the spin-3/2 particle. The function $\theta_{\mu\nu}(V)$ is defined as [80]

$$\theta_{\mu\nu}(V) = g_{\mu\nu} - \left(V + \frac{1}{2}\right)\gamma_\mu\gamma_\nu\,, \tag{A.14}$$

with $V$ a so-called *off-shell parameter*.

The strong interaction Lagrangian for a spin-1/2 resonance can have a pseudoscalar or a pseudovector form. As in Eq. (A.9), we have used the pseudoscalar scheme:

$$\mathcal{L}^{PS}_{KYR(1/2)} = -ig_{KYR(1/2)}K^\dagger\overline{Y}\,\Gamma R + h.c., \tag{A.15}$$

with $\Gamma$ defined as before. The hadronic vertex for spin-3/2 exchange is given by

$$\mathcal{L}_{KYR(3/2)} = \frac{f_{KYR(3/2)}}{M_K}\overline{R}^\mu\theta_{\mu\nu}\left(Z_{R(3/2)}\right)\Gamma'Y\left(\partial^\nu K\right) + h.c.\,, \tag{A.16}$$

with $\Gamma' = 1\ (\gamma^5)$ for even (odd) parity resonances.

The fits of the model calculations to the data provide access to the following combinations of coupling constants:

$$G_{R(1/2)} = \frac{g_{KYR(1/2)}}{\sqrt{4\pi}}\,\kappa_{pN^*} \tag{A.17}$$

for spin-1/2 states, and

$$G^{(1,2)}_{R(3/2)} = \frac{ef_{KYR(3/2)}}{4\pi}\,\kappa^{(1,2)}_{pR(3/2)}\,,\ \ X_{R(3/2)}\,,\ \ Y_{R(3/2)}\,,\ \ Z_{R(3/2)} \tag{A.18}$$

for spin-3/2 resonance exchange.

## A.2 Feynman Propagators

For the spin-0 and spin-1 Feynman propagators, we adopt the standard expressions:

$$\mathcal{P}_0(q) = i\,\frac{1}{q^2 - m^2}\,, \tag{A.19}$$

$$\mathcal{P}_1^{\mu\nu}(q) = i\,\frac{1}{q^2 - m^2}\left[-g^{\mu\nu} + \frac{q^\mu q^\nu}{m^2}\right]\,, \tag{A.20}$$

where $q$ and $m$ are the four-momentum and mass of the propagating particle.

The propagator for spin-1/2 particles reads:

$$\mathcal{P}_{1/2}(q) = i\frac{\not{q} + m}{q^2 - m^2}\,. \tag{A.21}$$

Although the optimum choice for the spin-3/2 propagator remains a subject of discussion [80], we have used the Rarita-Schwinger form in accordance with Ref. [71]:

$$\begin{aligned}\mathcal{P}_{3/2}^{\mu\nu}(q) &= i\,\frac{\not{q} + m}{3\,(q^2 - m^2)} \\ &\quad \times \left[3g^{\mu\nu} - \gamma^\mu\gamma^\nu - \frac{2q^\mu q^\nu}{m^2} - \frac{\gamma^\mu q^\nu - \gamma^\nu q^\mu}{m}\right]\,.\end{aligned} \tag{A.22}$$

## A.3 Isospin symmetry in the $K^+\Sigma^0/K^0\Sigma^+$ channels

In this Appendix, we sketch how isospin arguments can be applied to establish relations between the coupling constants for the $\gamma p \rightarrow K^+\Sigma^0$ and $\gamma p \rightarrow K^0\Sigma^+$ channels. Only the relations specifically required for this work are mentioned. A more extensive review can e.g. be found in Ref. [29]. In what follows, the isospin symmetry of the various meson and baryon multiplets is assumed to be exact.

All hadronic decay processes relevant to the RPR treatment of forward-angle $K\Sigma$ photoproduction are either of the type $N \rightarrow K\Sigma$ or $\Delta \rightarrow K\Sigma$. Because of the isovector nature of the $\Sigma$ particle, the hadronic couplings are proportional to the Clebsch-Gordan coefficients:

$$g_{K\Sigma N} \sim \, < I_K = \frac{1}{2},\ M_K;\ I_\Sigma = 1,\ M_\Sigma \,|\, I_N = \frac{1}{2},\ M_N >\,, \tag{A.23}$$

$$g_{K\Sigma\Delta} \sim \, < I_K = \frac{1}{2},\ M_K;\ I_\Sigma = 1,\ M_\Sigma \,|\, I_\Delta = \frac{3}{2},\ M_\Delta >\,. \tag{A.24}$$

When adopting the following conventions for the isospin states of the $N$, $K$ and $\Sigma$ particles,

$$\begin{aligned} \Sigma^+ &\leftrightarrow -|I=1,\ M=+1\rangle \ , \\ \Sigma^0 &\leftrightarrow +|I=1,\ M=0\rangle \ , \\ \Sigma^- &\leftrightarrow +|I=1,\ M=-1\rangle \ ; \end{aligned} \tag{A.25}$$

$$\begin{aligned} p \leftrightarrow \left| I=\frac{1}{2},\ M=+\frac{1}{2} \right\rangle \leftrightarrow K^+ \ , \\ n \leftrightarrow \left| I=\frac{1}{2},\ M=-\frac{1}{2} \right\rangle \leftrightarrow K^0 \ . \end{aligned} \tag{A.26}$$

these simple relations emerge:

$$g_{K^0\Sigma^+p} = \sqrt{2}\, g_{K^+\Sigma^0p} \ , \tag{A.27}$$

$$g_{K^0\Sigma^+\Delta^+} = -\frac{1}{\sqrt{2}}\, g_{K^+\Sigma^0\Delta^+} \ , \tag{A.28}$$

The isospin relations are valid both when ground-state hadrons or hadron resonances are involved.

Contrary to the hadronic parameters, the relations between electromagnetic couplings have to be distilled from experimental information. In principle, the value of the magnetic transition moment $\kappa_{K^*K}$ can be determined on the basis of the proportionality $\kappa^2_{K^*K} \sim \Gamma_{K^*\rightarrow K\gamma}$. Within the context of tree-level models, however, the coupling constants are frequently considered as "effective couplings" in which, for example, part of the final-state interaction effects are absorbed. It is a common procedure to use only the ratios of the measured decay widths to connect isospin-related coupling constants. Using the PDG values for the $K^{*+}(892)$ and $K^{*0}(892)$ widths, i.e. [114]:

$$\Gamma_{K^{*+}(892)\rightarrow K^+(494)\gamma} = 50 \pm 5 \text{ keV} \ , \tag{A.29}$$

$$\Gamma_{K^{*0}(892)\rightarrow K^0(494)\gamma} = 116 \pm 10 \text{ keV} \ , \tag{A.30}$$

the following expression is obtained:

$$\kappa_{K^{*0}(892)\,K^0(494)} = -1.52\ \kappa_{K^{*+}(892)\,K^+(494)} \ . \tag{A.31}$$

The relative sign in the last expression was selected on the basis of a constituent-quark model prediction by Singer and Miller [141], which accurately reproduces the experimental widths of Eqs. (A.29) and (A.30).

APPENDIX

# B

# Parameters of the RPR model

## B.1 Fitting procedure

The optimum set of coupling constants $(c_1, ..., c_n)$ for a given set of data points $(D_1, ..., D_N)$ is considered to be the one that produces the lowest value for $\chi^2$, defined as

$$\chi^2 = \frac{1}{N} \sum_{i=1}^{N} \frac{[D_i - P_i(c_1, \cdots, c_n)]^2}{\sigma_{D_i}^2} , \tag{B.1}$$

where $P_i$ represents the theoretical prediction for the data point $D_i$ with standard error $\sigma_{D_i}^2$.

In this work, the complex issue of minimizing $\chi^2$ is tackled using a simulated annealing algorithm (SAA) [142] developed by S. Janssen [71]. This algorithm has been designed to produce parameters near the *global* minimum of the $\chi^2$ surface. A more detailed explanation is available from Ref. [71].

In our treatment of the $K\Sigma$ channels, which involve a greater number of parameters than the $K\Lambda$ one, we deemed it more efficient to use a combination of the SAA and the CERN MINUIT [143] package. This work was carried out in collaboration with D.G. Ireland [93, 125]. Starting points for minimization were obtained from the SAA. The parameters provided by the SAA were then fed into MINUIT in order to pinpoint the location of each minimum more precisely, and obtain an error matrix for the fitted parameters.

## B.2 Extracted coupling constants

In Tables B.2 and B.1, we list the optimum parameter values for the RPR-2′ $K\Lambda$ and the RPR-3 $K\Sigma$ models, respectively.

| **Background** | | |
|---|---|---|
| $K^+(494)$ / $p$ | $\frac{g_{K^+\Lambda p}}{4\pi}$ | -3.0 |
| $K^{*+}(892)$ | $G^{v}_{K^{*+}(892)\Lambda p}$ | $2.607 \cdot 10^{-1}$ |
| | $G^{t}_{K^{*+}(892)\Lambda p}$ | $-7.004 \cdot 10^{-1}$ |
| **$N^*$ resonances** | | |
| $S_{11}(1650)$ | $G_{S_{11}(1650)}$ | $-6.349 \cdot 10^{-3}$ |
| $P_{11}(1710)$ | $G_{P_{11}(1710)}$ | $-6.623 \cdot 10^{-2}$ |
| $P_{13}(1720)$ | $G^{(1)}_{P_{11}(1720)}$ | $4.570 \cdot 10^{-3}$ |
| | $G^{(2)}_{P_{11}(1720)}$ | $-3.054 \cdot 10^{-3}$ |
| | $X_{P_{11}(1720)}$ | $1.437 \cdot 10^{2}$ |
| | $Y_{P_{11}(1720)}$ | $5.696 \cdot 10$ |
| | $Z_{P_{11}(1720)}$ | $-3.117 \cdot 10^{-1}$ |
| $P_{13}(1900)$ | $G^{(1)}_{P_{13}(1900)}$ | $-1.052 \cdot 10^{-1}$ |
| | $G^{(2)}_{P_{13}(1900)}$ | $7.166 \cdot 10^{-2}$ |
| | $X_{P_{13}(1900)}$ | $-1.7 \cdot 10$ |
| | $Y_{P_{13}(1900)}$ | $2.588$ |
| | $Z_{P_{13}(1900)}$ | $-8.878 \cdot 10^{-1}$ |
| $D_{13}(1900)$ | $G^{(1)}_{D_{13}(1900)}$ | $1.558 \cdot 10^{-1}$ |
| | $G^{(2)}_{D_{13}(1900)}$ | $1.077 \cdot 10^{-1}$ |
| | $X_{D_{13}(1900)}$ | $4.031 \cdot 10$ |
| | $Y_{D_{13}(1900)}$ | $-1.399 \cdot 10$ |
| | $Z_{D_{13}(1900)}$ | $-3.969 \cdot 10^{-2}$ |
| **Other** | | |
| cutoff mass | $\Lambda_{res}$ (MeV) | 1636.53 |

**Table B.1** Numerical values of the coupling constants for the $p(\gamma^{(*)}, K^+)\Lambda$ process using the RPR-2′ model from Sec. 4.1.

<table>
<tr><th colspan="3">Background</th></tr>
<tr><td>$K^+(494)$ / $p$</td><td>$\frac{g_{K^+\Sigma^0 p}}{4\pi}$</td><td>$1.299$</td></tr>
<tr><td>$K^{*+}(892)$</td><td>$G^{v}_{K^{*+}(892)\Sigma^0 p}$</td><td>$-3.505 \cdot 10^{-1}$</td></tr>
<tr><td></td><td>$G^{t}_{K^{*+}(892)\Sigma^0 p}$</td><td>$6.813 \cdot 10^{-1}$</td></tr>
<tr><td>$K^{*0}(1410)$</td><td>$G^{v}_{K^{*0}(1410)\Sigma^+ p}$</td><td>$-3.387$</td></tr>
<tr><td></td><td>$G^{t}_{K^{*0}(1410)\Sigma^+ p}$</td><td>$4.557$</td></tr>
<tr><th colspan="3">$N^*$ resonances</th></tr>
<tr><td>$S_{11}(1650)$</td><td>$G_{S_{11}(1650)}$</td><td>$-3.924 \cdot 10^{-2}$</td></tr>
<tr><td>$P_{11}(1710)$</td><td>$G_{P_{11}(1710)}$</td><td>$4.918 \cdot 10^{-2}$</td></tr>
<tr><td>$P_{13}(1720)$</td><td>$G^{(1)}_{P_{11}(1720)}$</td><td>$2.187 \cdot 10^{-2}$</td></tr>
<tr><td></td><td>$G^{(2)}_{P_{11}(1720)}$</td><td>$9.586 \cdot 10^{-3}$</td></tr>
<tr><td></td><td>$X_{P_{11}(1720)}$</td><td>$-6.114$</td></tr>
<tr><td></td><td>$Y_{P_{11}(1720)}$</td><td>$-4.490 \cdot 10^{-1}$</td></tr>
<tr><td></td><td>$Z_{P_{11}(1720)}$</td><td>$3.276$</td></tr>
<tr><td>$P_{13}(1900)$</td><td>$G^{(1)}_{P_{13}(1900)}$</td><td>$1.376 \cdot 10^{-1}$</td></tr>
<tr><td></td><td>$G^{(2)}_{P_{13}(1900)}$</td><td>$4.011 \cdot 10^{-1}$</td></tr>
<tr><td></td><td>$X_{P_{13}(1900)}$</td><td>$4.465$</td></tr>
<tr><td></td><td>$Y_{P_{13}(1900)}$</td><td>$-3.495$</td></tr>
<tr><td></td><td>$Z_{P_{13}(1900)}$</td><td>$-5.272 \cdot 10^{-1}$</td></tr>
<tr><th colspan="3">$\Delta^*$ resonances</th></tr>
<tr><td>$S_{31}(1900)$</td><td>$G_{S_{31}(1900)}$</td><td>$9.129 \cdot 10^{-2}$</td></tr>
<tr><td>$P_{31}(1910)$</td><td>$G_{P_{31}(1910)}$</td><td>$-7.326 \cdot 10^{-2}$</td></tr>
<tr><td>$D_{33}(1700)$</td><td>$G^{(1)}_{D_{33}(1700)}$</td><td>$-2.874 \cdot 10^{-1}$</td></tr>
<tr><td></td><td>$G^{(2)}_{D_{33}(1700)}$</td><td>$-3.374 \cdot 10^{-1}$</td></tr>
<tr><td></td><td>$X_{D_{33}(1700)}$</td><td>$-4.999$</td></tr>
<tr><td></td><td>$Y_{D_{33}(1700)}$</td><td>$-4.521$</td></tr>
<tr><td></td><td>$Z_{D_{33}(1700)}$</td><td>$-1.577 \cdot 10^{-1}$</td></tr>
<tr><td>$P_{33}(1920)$</td><td>$G^{(1)}_{P_{33}(1920)}$</td><td>$6.722 \cdot 10^{-2}$</td></tr>
<tr><td></td><td>$G^{(2)}_{P_{33}(1920)}$</td><td>$9.980 \cdot 10^{-2}$</td></tr>
<tr><td></td><td>$X_{P_{33}(1920)}$</td><td>$8.031$</td></tr>
<tr><td></td><td>$Y_{P_{33}(1920)}$</td><td>$2.416$</td></tr>
<tr><td></td><td>$Z_{P_{33}(1920)}$</td><td>$-5.272 \cdot 10^{-1}$</td></tr>
<tr><th colspan="3">Other</th></tr>
<tr><td>cutoff mass</td><td>$\Lambda_{res}$ (MeV)</td><td>1593.37</td></tr>
</table>

Numerical values of the coupling constants for the $p(\gamma^{(*)}, K)\Sigma$ processes using the RPR-3 model from Sec. 4.2.

APPENDIX

C

# Deriving the Regge propagator

In this Appendix, we sketch the derivation of the Regge propagator for the two-particle scattering reaction $1+2 \to 3+4$ in the case of spinless external particles. To simplify the mathematics, we assume that all particles participating in this process have identical masses ($m$). The generalization to non-equal masses is straightforward and has no impact on the general conclusions. A more detailed account of the different steps in the derivation is given in Ref. [106].

**Partial-wave expansion**

When the external particles are on shell, the scattering amplitude $\mathcal{M}$ is a function of two independent variables, which can be chosen for example as $s$ and $t$ [1]. It is then possible to expand $\mathcal{M}(s,t)$ in terms of Legendre polynomials:

$$\mathcal{M}\left(s,t\right) = \sum_{l=0}^{\infty} \left(2l+1\right) \mathcal{M}_l\left(s\right) P_l\left(\cos\theta_s\right) \ , \tag{C.1}$$

where

$$\cos\theta_s = 1 + \frac{2t}{s-4m^2} = -\left(1 + \frac{2u}{s-4m^2}\right) \tag{C.2}$$

is the angle between the three-momenta of particles 1 and 3. For spinless particles, $l$ can be identified with the conserved total angular momentum in the reaction. The

---

[1] The same reasoning can be made using $s$ and $u$.

partial-wave amplitude $\mathcal{M}_l(s)$ is given by:

$$\mathcal{M}_l(s) = \frac{1}{2}\int_{-1}^{+1} d\cos\theta_s\, \mathcal{M}\big(s, t(s, \cos\theta_s)\big) P_l(\cos\theta_s) \quad (l = 0, 1, 2, \ldots) . \tag{C.3}$$

The Legendre expansion of Eq. (C.1) is valid in the physical region of the "direct" or s-channel process $1 + 2 \to 3 + 4$, defined by the conditions:

$$s \geq 4m^2 , \qquad -1 \leq \cos\theta_s \leq +1 \quad \text{or} \quad t \leq 0 . \tag{C.4}$$

It is, however, not guaranteed to converge beyond those limits.

## Crossing symmetry

Regge theory relies heavily on the principle of crossing symmetry (Sec. 2.4.1). This entails that the "crossed" or t-channel process $1 + \overline{3} \to \overline{2} + 4$ can be described by the same complex function $\mathcal{M}$ as the direct s-channel process, albeit for different values of the variables. Specifically,

$$\mathcal{M}_s(s, t) \equiv \mathcal{M}_t(t, s) , \tag{C.5}$$

where $\mathcal{M}_s$ ($\mathcal{M}_t$) represents the amplitude for the s- (t-) channel reaction. It is clear that, if $(t, s)$ belongs to the physical region of the t-channel process,

$$t \geq 4m^2 , \qquad -1 \leq \cos\theta_t \leq +1 \quad \text{or} \quad s \leq 0 , \tag{C.6}$$

where

$$\cos\theta_t = 1 + \frac{2s}{t - 4m^2} = -\left(1 + \frac{2u}{t - 4m^2}\right) , \tag{C.7}$$

then $(s, t)$ cannot belong to the s-channel physical region, and vice versa. One may, however, obtain the amplitude for the direct reaction by analytically continuing $\mathcal{M}_t$ from the t-channel to the s-channel physical region. This is, in fact, the central idea behind Regge theory.

For the crossed amplitude, an analogous decomposition as in Eq. (C.1) can be constructed:

$$\mathcal{M}_t(t, s) = \mathcal{M}_s(s, t) = \sum_{l=0}^{\infty} (2l + 1)\, \mathcal{M}_l(t)\, P_l(\cos\theta_t) . \tag{C.8}$$

In Refs. [111,112], it is demonstrated that the convergence of a partial-wave series of the type (C.8) can only be guaranteed for $t \geq 4m^2$ and with $\cos\theta_t$ inside the so-called Lehmann-Martin ellipse, shown in Fig. C.1. It has foci at ±1 and a large axis which is determined by:

$$\cos\theta_0 = 1 + \frac{8m^2}{t - 4m^2} . \tag{C.9}$$

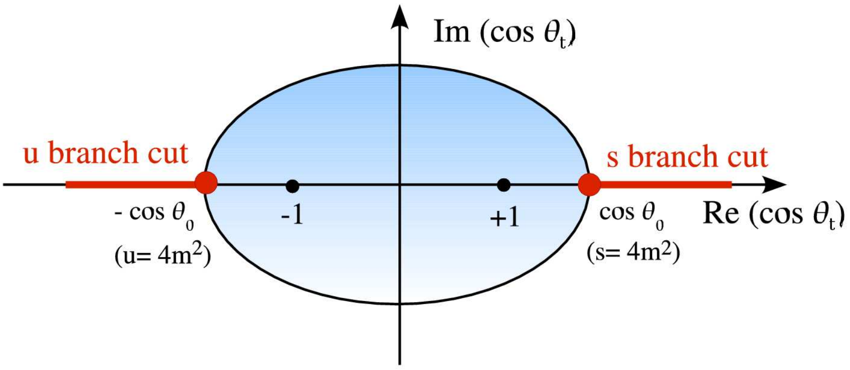

**Figure C.1** The Lehmann-Martin ellipse in the complex $\cos\theta_t$ plane, for the equal-mass t-channel scattering process.

The values $\cos\theta_t = \pm\cos\theta_0$ correspond to branch points of the amplitude in the complex $\cos\theta_t$ plane (see for example [106]). According to Eq. (C.7), these occur at $s = 4m^2$ and $u = 4m^2$, respectively. Extrapolating $\mathcal{M}_t$ towards the physical region of the direct s-channel process involves crossing the boundaries of the Lehmann-Martin ellipse. In order to accomplish this, it is necessary to cast Eq. (C.8) into a form more suitable for analytic continuation.

### The Sommerfeld-Watson transformation

The advised strategy is to sum over all t-channel partial waves *before* attempting to extrapolate Eq. (C.8) beyond the convergence region. This summation should be performed in such a way that it results in an analytical function of $s$ (or $\cos\theta_t$) and $t$, which can be used outside the Lehmann-Martin ellipse. The above can be realized by transforming the sum over $l$ into a contour integral in the complex angular momentum, or $\lambda$, plane. Using the residue theorem, Eq. (C.8) can be re-written as:

$$\mathcal{M}\left(s,t\right) = -\frac{1}{2i}\oint_{C_1} d\lambda \frac{\left(2\lambda+1\right)\mathcal{M}_\lambda\left(t\right)P_\lambda\left(-\cos\theta_t\right)}{\sin\left(\pi\lambda\right)}\,, \tag{C.10}$$

where we have omitted the lower index "s" in $\mathcal{M}_s$ for conciseness. This technique is known as the *Sommerfeld-Watson* transformation. $P_\lambda(z)$ is the Legendre function of the first kind, which is an analytical function of $\lambda$ and $z$ and obeys the relation $P_\lambda(-z) = (-1)^\lambda P_\lambda(z)$. The poles of the integrand are produced by the factor $\dfrac{1}{\sin\left(\pi\lambda\right)}$ since:

$$\sin\left(\pi\lambda\right) \xrightarrow{\lambda\to l} \left(-1\right)^\lambda\left(\lambda-l\right)\pi\,. \tag{C.11}$$

The contour $C_1$ is shown in Fig. C.2. A necessary condition for the Sommerfeld-Watson transformation is that $\mathcal{M}_\lambda\left(t\right)$ is an analytical function of $\lambda$. Although this theorem,

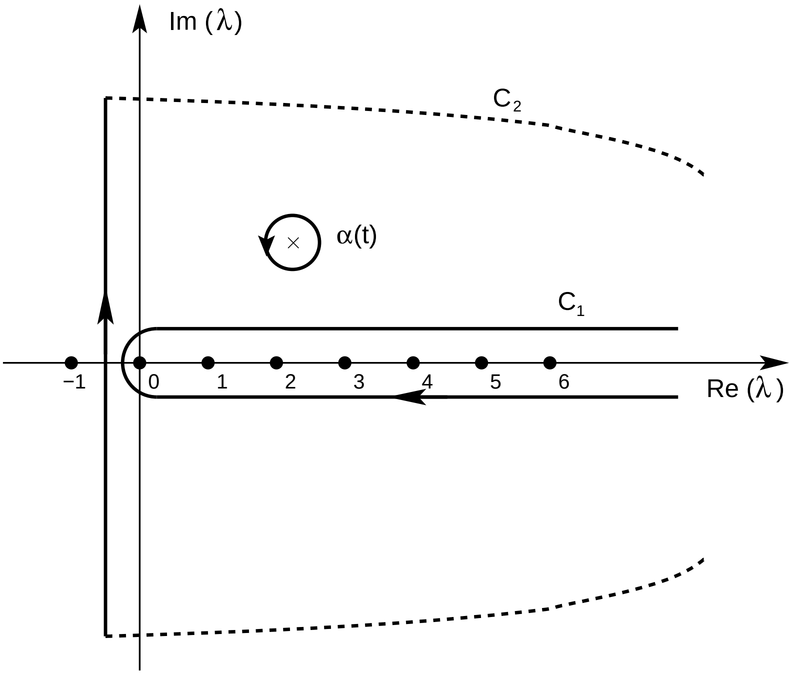

**Figure C.2** The contours $C_1$ and $C_2$ in the complex angular-momentum plane. The poles at the real axis and at $\alpha\,(t)$ are indicated.

known as the postulate of *maximal analyticity of the second kind*, cannot be proven on the basis of fundamental principles, it seems to be supported by strong interaction models [106] and by the available experimental information.

### The Froissart-Gribov projection

The integral in Eq. (C.10) can be simplified by deforming the contour toward infinity. This requires that we verify the convergence of $\mathcal{M}_\lambda\,(t)$ at $\lambda \to \infty$. As a starting point, we consider a dispersion relation for $\mathcal{M}\,(s,t)$ at fixed $t$. We use the Cauchy integral formula, which states that

$$F(z) = \frac{1}{2\pi i} \oint_C \frac{dz'}{z' - z} F(z')\,, \tag{C.12}$$

with $C$ a contour around $z$ which does not contain any singularities of $F$. For $\mathcal{M}\,(s(\cos\theta_t), t)$, one may use a contour at infinity which “circumvents” the branch cuts and poles as depicted in Fig. C.3, resulting in:

$$\begin{aligned}\mathcal{M}\,(s\,(\cos\theta_t)\,,t) \;&=\; \text{pole terms} + \frac{1}{\pi}\int_{\cos\theta_0}^{+\infty} dz' \frac{D_s\,(z',t)}{z' - \cos\theta_t} \\ &\quad -\frac{1}{\pi}\int_{-\infty}^{-\cos\theta_0} dz' \frac{D_u\,(z',t)}{z' - \cos\theta_t}\,.\end{aligned} \tag{C.13}$$

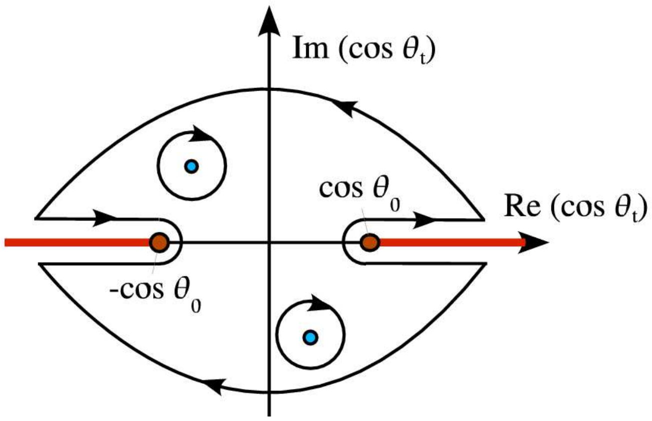

**Figure C.3** Contour used to obtain the dispersion relation (C.13). The red lines indicate the branch cuts of $\mathcal{M}_s(s,t)$, whereas the possible poles are indicated as blue dots.

The discontinuity functions along the branch cuts are defined as:

$$\begin{aligned} D_s(z,t) &= \lim_{\varepsilon\to 0}\frac{1}{2i}\left(\mathcal{M}(s+i\varepsilon,t,u)-\mathcal{M}(s-i\varepsilon,t,u)\right) , && \text{(C.14)}\\ D_u(z,t) &= \lim_{\varepsilon\to 0}\frac{1}{2i}\left(\mathcal{M}(s,t,u+i\varepsilon)-\mathcal{M}(s,t,u-i\varepsilon)\right) , && \text{(C.15)}\end{aligned}$$

where we have introduced the shorthand notation $z \equiv \cos\theta_t$. Herein, $s \pm i\varepsilon$ ($u \mp i\varepsilon$) correspond to values of $\cos\theta_t$ just above or below the $s$ ($u$) branch cut (Eq. C.7). The dispersion relation (C.13) can be substituted into the definition of the partial-wave amplitude:

$$\begin{aligned} \mathcal{M}_\lambda(t) &= \frac{1}{2}\int_{-1}^{+1} d\cos\theta_t\, \mathcal{M}(s(\cos\theta_t),t)\ P_\lambda(\cos\theta_t) && \text{(C.16)}\\ &= \frac{1}{2}\int_{-1}^{+1} d\cos\theta_t \frac{1}{\pi}\int_{\cos\theta_0}^{+\infty} dz' P_\lambda(\cos\theta_t)\left[\frac{D_s(z',t)}{z'-\cos\theta_t}+\frac{D_u(-z',t)}{z'+\cos\theta_t}\right] \end{aligned}$$

where we have performed the transformation $z' \to -z'$ in the third term of Eq. (C.13). By introducing the Legendre function of the second kind,

$$Q_\lambda(z) = \frac{1}{2}\int_{-1}^{+1} dz' \frac{P_\lambda(z')}{z-z'} , \tag{C.17}$$

and interchanging the integration variables, one eventually obtains the *Froissart-Gribov projection*:

$$\mathcal{M}_\lambda(t) = \frac{1}{\pi}\int_{\cos\theta_0}^{+\infty} dz'\ Q_\lambda(z')\left[D_s(z',t) + (-1)^\lambda D_u(-z',t)\right] . \tag{C.18}$$

The asymptotic behavior of the Legendre function of the second kind is given by:

$$Q_\lambda(z) \overset{|\lambda|\to\infty}{\longrightarrow} \lambda^{-1/2} e^{-(\lambda+1/2)\ln\left(z+\sqrt{z^2+1}\right)} . \tag{C.19}$$

This can be shown to imply that $M_\lambda(t)$ in Eq. (C.18) converges for large $\lambda$, except for the factor $(-1)^\lambda$. This final issue may be solved by distinguishing between two types of partial waves

$$\mathcal{M}_\lambda^{\zeta=\pm}(t) = \frac{1}{\pi}\int_{\cos\theta_0}^{+\infty} dz'\, Q_\lambda(z')\left[D_s(z',t) + \zeta D_u(-z',t)\right] \ , \tag{C.20}$$

with different *signatures* $\zeta = \pm$. For either possibility, $M_\lambda^\zeta(t)$ now converges for $|\lambda| \to \infty$. The connection to the *physical* partial-wave amplitudes simply reads:

$$\mathcal{M}_\lambda(t) = \mathcal{M}_\lambda^+(t) \ , \qquad \lambda = 0, 2, 4 \ldots \tag{C.21}$$

$$\mathcal{M}_\lambda(t) = \mathcal{M}_\lambda^-(t) \ , \qquad \lambda = 1, 3, 5 \ldots \tag{C.22}$$

**Regge poles**

The contour $C_1$ from the Sommerfeld-Watson transformation (Eq. (C.10)) can now be deformed into an alternative contour, $C_2$, also depicted in Fig. C.2. Even if the contributions at infinity vanish, other singularities have to be taken into account. It was Regge who postulated that the only singularities of the amplitude $\mathcal{M}_\lambda^\zeta(t)$ are poles in the complex plane at $\lambda = \alpha_i^\zeta(t)$. In the vicinity of such a pole, the amplitude assumes the form:

$$\mathcal{M}_\lambda^\zeta(t) \xrightarrow{\lambda\to\alpha_i^\zeta(t)} \frac{\beta_i^\zeta(t)}{\lambda - \alpha_i^\zeta(t)} \ , \tag{C.23}$$

with $\beta_i^\zeta(t)$ the residue. The Sommerfeld-Watson representation then becomes:

$$\begin{aligned}\widetilde{\mathcal{M}}^\zeta(s,t) &= -\frac{1}{2i}\int_{-1/2-i\infty}^{-1/2+i\infty} d\lambda \frac{(2\lambda+1)\,\mathcal{M}_\lambda^\zeta(t)\,P_\lambda(-\cos\theta_t)}{\sin(\pi\lambda)} \\ &\quad -\pi\sum_i \left(2\alpha_i^\zeta(t)+1\right)\frac{\beta_i^\zeta(t)}{\sin\left(\pi\alpha_i^\zeta(t)\right)}\,P_{\alpha_i^\zeta(t)}(-\cos\theta_t) \ .\end{aligned} \tag{C.24}$$

The first term is called the *background integral*. Taking into account the asymptotic behavior of $P_\lambda(z)$:

$$P_\lambda(z) \xrightarrow{z\to\infty} \begin{cases} \frac{1}{\sqrt{\pi}}\frac{\Gamma(l+1/2)}{\Gamma(\lambda+1)}(2z)^\lambda \ , & \mathrm{Re}\{\lambda\} \geq -1/2 \ , \\ \frac{1}{\sqrt{\pi}}\frac{\Gamma(-\lambda-1/2)}{\Gamma(-\lambda)}(2z)^{-\lambda-1} \ , & \mathrm{Re}\{\lambda\} \leq -1/2 \ , \end{cases} \tag{C.25}$$

this integral can be shown to behave like $s^{-1/2}$ for $s \to \infty$. It can therefore be neglected in the high-$s$ limit.

The required conditions (C.21) and (C.22) can be guaranteed by defining the *physical* fixed-signature amplitudes $\mathcal{M}^\zeta(s,t)$ as

$$\mathcal{M}^\zeta(s,t) = \frac{1}{2}\left[\widetilde{\mathcal{M}}^\zeta(z,t) + \zeta\,\widetilde{\mathcal{M}}^\zeta(-z,t)\right] \ , \tag{C.26}$$

where we have written the functional dependencies as $(z,t)$ instead of $(s,t)$, and

$$\mathcal{M}\left(s,t\right) = \mathcal{M}^{+}\left(s,t\right) + \mathcal{M}^{-}\left(s,t\right)\ . \tag{C.27}$$

Assuming that the background integral in Eq. (C.24) can be neglected, one obtains the following expression:

$$\mathcal{M}^{\zeta}\left(s,t\right) = -\pi\sum_{i}\left(2\alpha_i^{\zeta}\left(t\right)+1\right)\frac{\beta_i^{\zeta}\left(t\right)}{\sin\left(\pi\alpha_i^{\zeta}\left(t\right)\right)} \tag{C.28}$$

$$\frac{1}{2}\left[P_{\alpha_i^{\zeta}(t)}\left(-\cos\theta_t\right)+\zeta P_{\alpha_i^{\zeta}(t)}\left(\cos\theta_t\right)\right]\ . \tag{C.29}$$

The sum of the two Legendre functions can be re-written as:

$$\left[\left(1+\zeta e^{-i\pi\alpha_i^{\zeta}(t)}\right)P_{\alpha_i^{\zeta}(t)}\left(-\cos\theta_t\right)-\zeta\frac{2}{\pi}\sin\left(\pi\alpha_i^{\zeta}\left(t\right)\right)Q_{\alpha_i^{\zeta}(t)}\left(-\cos\theta_t\right)\right]\ . \tag{C.30}$$

For $s\longrightarrow\infty$, the term proportional to $Q_{\alpha_i^{\zeta}(t)}\left(z\right)$ may be neglected due to its asymptotic behavior:

$$Q_{\alpha_i^{\zeta}(t)}\left(z\right)\overset{z\rightarrow\infty}{\longrightarrow}\sqrt{\pi}\frac{\Gamma\left(\alpha_i^{\zeta}(t)+1\right)}{\Gamma\left(\alpha_i^{\zeta}(t)+\frac{3}{2}\right)}\left(2z\right)^{-\alpha_i^{\zeta}(t)-1}\ . \tag{C.31}$$

Our final result for the high-$s$ scattering amplitude for a fixed signature $\zeta$ reads:

$$\mathcal{M}^{\zeta}\left(s,t\right) = -\pi\sum_{i}\left(2\alpha_i^{\zeta}\left(t\right)+1\right)\frac{\beta_i^{\zeta}\left(t\right)}{\sin\left(\pi\alpha_i^{\zeta}\left(t\right)\right)} \tag{C.32}$$

$$\frac{1+\zeta e^{-i\pi\alpha_i^{\zeta}(t)}}{2}P_{\alpha_i^{\zeta}(t)}\left(-\cos\theta_t\right)\ . \tag{C.33}$$

### The Regge limit

The expression (C.33) can be simplified even further in the so-called *Regge* limit of high $s$ and small negative $t$. In this kinematic region, $\alpha_i^{\zeta}(t)$ is small and the following expression for the Regge scattering amplitude is obtained:

$$\mathcal{M}^{\zeta}_{\text{Regge}}\left(s,t\right) = C\sum_{i}\left(\frac{s}{s_0}\right)^{\alpha_i^{\zeta}(t)}\frac{\beta_i^{\zeta}\left(t\right)}{\sin\left(\pi\alpha_i^{\zeta}\left(t\right)\right)} \tag{C.34}$$

$$\frac{1+\zeta e^{-i\pi\alpha_i^{\zeta}(t)}}{2}\frac{1}{\Gamma\left(\alpha_i^{\zeta}\left(t\right)+1\right)}\ . \tag{C.35}$$

Hereby, use is made of Eq. (C.25) for the high-$z$ behavior of $P_{\alpha(t)}\left(z\right)$, and of the fact that $\Gamma\left(\alpha\left(t\right)+1/2\right)\simeq\sqrt{\pi}$ and $\left(2\alpha\left(t\right)+1\right)\simeq 1$ for small $\alpha\left(t\right)$. The newly introduced constant $C$ has to be defined in connection with the residue function $\beta\left(t\right)$. The scale factor $s_0$ is arbitrarily fixed at 1 GeV$^2$.

We should recall that Eq. (C.35) has been derived in an equal-mass hypothesis. When extending the derivation to particles with non-equal masses, the physical regions and the Lehmann-Martin ellipse (Fig. C.1) become distorted. For example, the physical region of the $s$-channel process is no longer determined by the conditions $t \leq 0$, $u \leq 0$, but acquires $s$-dependent boundaries $t_{min}(s)$ and $u_{min}(s)$ [106].

# Bibliography

[1] in *The Rise of the standard model: Particle physics in the 1960s and 1970*, edited by L. Hoddeson, L. Brown, M. Riordan, and M. Dresden (Cambridge Univ. Press, New York, 1997), prepared for 3rd International Symposium on the History of Particle Physics: The Rise of the Standard Model, Stanford, California, 24-27 Jun 1992.

[2] D. J. Gross and F. Wilczek, Phys. Rev. Lett. **30**, 1343 (1973).

[3] D. J. Gross and F. Wilczek, Phys. Rev. D **8**, 3633 (1973).

[4] H. D. Politzer, Phys. Rev. Lett. **30**, 1346 (1973).

[5] H. D. Politzer, Phys. Rep. **14**, 129 (1974).

[6] H. J. Rothe, *Lattice gauge theories: an introduction*, Vol. 74 of *World Scientific Lecture Notes in Physics*, 3rd ed. (World Scientific, New Jersey, 2005).

[7] V. Burkert and T.-S. H. Lee, Int. J. Mod. Phys. E **13**, 1035 (2004).

[8] N. Isgur and G. Karl, Phys. Lett. B **72**, 109 (1977).

[9] N. Isgur and G. Karl, Phys. Rev. D **19**, 2653 (1979).

[10] N. Isgur and G. Karl, Phys. Rev. D **23**, 817 (1981).

[11] S. Capstick and N. Isgur, Phys. Rev. D **34**, 2809 (1986).

[12] U. Loering, B. C. Metsch, and H. R. Petry, Eur. Phys. J. A **10**, 395 (2001).

[13] M. Anselmino, E. Predazzi, S. Ekelin, S. Frederksson, and D. B. Lichtenberg, Rev. Mod. Phys. **65**, 1199 (1993).

[14] M. Kirchbach, M. Moshinsky, and Y. F. Smirnov, Phys. Rev. D **64**, 114005 (2001).

[15] R. Koniuk and N. Isgur, Phys. Rev. D **21**, 1868 (1980).

[16] S. Capstick and W. Roberts, Phys. Rev. D **49**, 4570 (1994).

[17] S. Capstick and W. Roberts, Phys. Rev. D **58**, 074011 (1998).

[18] Z. Li, Phys. Rev. C **52**, 1648 (1995).

[19] Z. Li, M. Wei-Hsing, and Z. Lin, Phys. Rev. C **54**, 2171(R) (1996).

[20] Z. Li, H. Ye, and M. Lu, Phys. Rev. C **56**, 1099 (1997).

[21] Z. Li and B. Saghai, Nucl.Phys. A **644**, 345 (1998).

[22] B. Saghai and Z. Li, Eur. Phys. J. A **11**, 217 (2001).

[23] S. Janssen, J. Ryckebusch, D. Debruyne, and T. Van Cauteren, Phys. Rev. C **65**, 015201 (2001).

[24] R. A. Adelseck and L. E. Wright, Phys. Rev. C **38**, 1965 (1988).

[25] R. A. Williams, C.-R. Ji, and S. R. Cotanch, Phys. Rev. C **46**, 1617 (1992).

[26] J. C. David, C. Fayard, G. H. Lamot, and B. Saghai, Phys. Rev. C **53**, 2613 (1996).

[27] T. Mart, C. Bennhold, and C. E. Hyde-Wright, Phys. Rev. C **51**, 1074(R) (1995).

[28] T. Mart and C. Bennhold, Phys. Rev. C **61**, 012201 (1999).

[29] S. Janssen, J. Ryckebusch, D. Debruyne, and T. Van Cauteren, Phys. Rev. C **66**, 035202 (2002).

[30] A. V. Sarantsev, V. A. Nikonov, A. V. Anisovich, E. Klempt, and U. Thoma, Eur. Phys. J. A **25**, 441 (2005).

[31] W.-T. Chiang, F. Tabakin, T.-S. H. Lee, and B. Saghai, Phys. Lett. B **517**, 101 (2001).

[32] G. Penner and U. Mosel, Phys. Rev. C **66**, 055212 (2002).

[33] V. Shklyar, H. Lenske, and U. Mosel, Phys. Rev. C **72**, 015210 (2005).

[34] B. Juliá-Diaz, B. Saghai, F. Tabakin, W.-T. Chiang, T.-S. H. Lee, and Z. Li, Nucl. Phys. A **755**, 463 (2005).

[35] B. Juliá-Diaz, B. Saghai, T.-S. H. Lee, and F. Tabakin, Phys. Rev. C **73**, 055204 (2006).

[36] T. Regge, Nuovo Cim. **14**, 951 (1959).

[37] M. Guidal, J.-M. Laget, and M. Vanderhaeghen, Nucl. Phys. A **627**, 645 (1997).

[38] M. Vanderhaeghen, M. Guidal, and J.-M. Laget, Phys. Rev. C **57**, 1454 (1998).

[39] M. Guidal, J.-M. Laget, and M. Vanderhaeghen, Phys. Rev. C **61**, 025204 (2000).

[40] M. Guidal, J.-M. Laget, and M. Vanderhaeghen, Phys. Rev. C **68**, 058201 (2003).

[41] A. Sibirtsev, K. Tsushima, and S. Krewald, Phys. Rev. C **67**, 055201 (2003).

[42] H. Holvoet, Ph.D. thesis, Ghent University, 2002.

[43] W.-T. Chiang, S. N. Yang, L. Tiator, M. Vanderhaeghen, and D. Drechsel, Phys. Rev. C **68**, 045202 (2003).

[44] A. Usov and O. Scholten, Phys. Rev. C **72**, 025205 (2005).

[45] D. Merten, U. Loering, K. Kretschmar, B. C. Metsch, and H.-R. Petry, Eur. Phys. J. A **14**, 477 (2002).

[46] C. Alexandrou, P. de Forcrand, H. Neff, J. W. Negele, W. Schroers, and A. Tsapalis, Phys. Rev. Lett. **94**, 021601 (2005).

[47] http://ebac-theory.jlab.org/papers.htm.

[48] P. L. Donoho and R. L. Walker, Phys. Rev. **107**, 1198 (1957).

[49] A. Silverman, R. R. Wilson, and W. M. Woodward, Phys. Rev. **108**, 501 (1957).

[50] T. K. Kuo, Phys. Rev. **129**, 2264 (1963).

[51] H. Thom, Phys. Rev. **151**, 1322 (1966).

[52] A. Bleckmann, S. Herda, U. Opara, W. Schulz, W. J. Schwille, and H. Urbahn, Z.Phys. **239**, 1 (1970).

[53] T. Fujii *et al.*, Phys. Rev. D **2**, 439 (1970).

[54] R. A. Adelseck, C. Bennhold, and L. E. Wright, Phys. Rev. C **32**, 1681 (1985).

[55] M. Q. Tran *et al.*, Phys. Lett. B **445**, 20 (1998).

[56] S. Goers *et al.*, Phys. Lett. B **464**, 331 (1999).

[57] J. W. C. McNabb *et al.*, Phys. Rev. C **69**, 042201(R) (2004).

[58] R. Bradford *et al.*, Phys.Rev. C **73**, 035202 (2006).

[59] R. Bradford *et al.*, Phys. Rev. C **75**, 035205 (2007).

[60] K.-H. Glander *et al.*, Eur. Phys. J. A **19**, 251 (2004).

[61] R. G. T. Zegers *et al.*, Phys. Rev. Lett. **91**, 092001 (2003).

[62] M. Sumihama *et al.*, Phys. Rev. C **73**, 035214 (2006).

[63] A. Lleres *et al.*, Eur. Phys. J. A **31**, 79 (2007).

[64] R. Lawall *et al.*, Eur. Phys. J. A **24**, 275 (2005).

[65] D. S. Carman *et al.*, Phys. Rev. Lett. **90**, 131804 (2003).

[66] R. M. Mohring *et al.*, Phys. Rev. C **67**, 055205 (2003).

[67] P. Ambrozewicz *et al.*, Phys. Rev. C **75**, 045203 (2007).

[68] C. N. Brown *et al.*, Phys. Rev. Lett. **28**, 1086 (1972).

[69] C. J. Bebek *et al.*, Phys. Rev. Lett. **32**, 21 (1974).

[70] C. J. Bebek *et al.*, Phys. Rev. D **15**, 594 (1977).

[71] S. Janssen, Ph.D. thesis, Ghent University, 2002.

[72] J. Bjorken and S. Drell, *Relativistic Quantum Mechanics* (McGraw-Hill Book Company, New York, 1964).

[73] F. Mandl and G. Shaw, *Quantum Field Theory* (John Wiley & Sons, Chichester, 1984).

[74] S. Janssen, *Constructing observables for strangeness production: extra technical notes with Ph. D. thesis*, http://inwpent5.ugent.be/papers/formalism.pdf.

[75] R. A. Adelseck and B. Saghai, Phys. Rev. C **42**, 108 (1990).

[76] I. S. Barker, A. Donnachie, and J. K. Storrow, Nucl. Phys. B **95**, 347 (1975).

[77] S. Nozawa and T.-S. H. Lee, Nucl. Phys. A **513**, 511 (1990).

[78] F. X. Lee, C. Bennhold, and L. E. Wright, Phys. Rev. C **55**, 318 (1997).

[79] G. Knöchlein, D. Drechsel, and L. Tiator, Z. Phys. A **352**, 327 (1995).

[80] M. Benmerrouche, R. M. Davidson, and N. C. Mukhopadhyay, Phys. Rev. C **39**, 2339 (1989).

[81] V. Pascalutsa, Phys. Rev. D **58**, 096002 (1998).

[82] J. Weda, Ph.D. thesis, KVI, University of Groningen, 1999.

[83] T. Van Cauteren, Ph.D. thesis, Ghent University, 2005.

[84] B. C. Pearce and B. K. Jennings, Nucl. Phys. A **528**, 655 (1991).

[85] T. Mart and A. Sulaksono, Phys. Rev. C **74**, 055203 (2006).

[86] G. Penner and U. Mosel, Phys. Rev. C **66**, 055211 (2002).

[87] K. Ohta, Phys. Rev. C **40**, 1335 (1989).

[88] H. Haberzettl, Phys. Rev. C **56**, 2041 (1997).

[89] R. M. Davidson and R. Workman, Phys. Rev. C **63**, 025210 (2001).

[90] J. J. de Swart, Rev. Mod. Phys. **35**, 916 (1963).

[91] R. Machleidt, K. Holinde, and C. Elster, Phys. Rep. **149**, 1 (1987).

[92] S. Janssen, J. Ryckebusch, W. Van Nespen, D. Debruyne, and T. Van Cauteren, Eur. Phys. J. A **11**, 105 (2001).

[93] S. Janssen, D. G. Ireland, and J. Ryckebusch, Phys. Lett. B **562**, 51 (2003).

[94] E. Noether, Nachr. v. d. Ges. d. Wiss. zu Goettingen 235 (1918).

[95] F. Gross and D. O. Riska, Phys. Rev. C **36**, 1928 (1987).

[96] M. Froissart, Phys. Rev. **123**, 1053 (1961).

[97] G. F. Chew and S. C. Frautschi, Phys. Rev. Lett. **7**, 394 (1961).

[98] G. F. Chew and S. C. Frautschi, Phys. Rev. Lett. **8**, 41 (1962).

[99] R. Blanckenbecler and M. L. Goldberger, Phys. Rev. **126**, 766 (1962).

[100] S. C. Frautschi, M. Gell-Mann, and F. Zachariasen, Phys. Rev. **126**, 2204 (1962).

[101] M. Guidal, J.-M. Laget, and M. Vanderhaeghen, Phys. Lett. B **400**, 6 (1997).

[102] M. Guidal, Ph.D. thesis, Université de Paris-Sud, U.F.R. Scientifique d'Orsay, 1997.

[103] I. G. Aznauryan, Phys. Rev. C **67**, 015209 (2003).

[104] I. G. Aznauryan, Phys. Rev. C **68**, 065204 (2003).

[105] V. Y. Grishina, L. A. Kondratyuk, W. Cassing, M. Mirazita, and P. Rossi, Eur. Phys. J. A **25**, 141 (2005).

[106] P. D. B. Collins, *An introduction to Regge theory and high energy physics* (Cambridge University Press, Cambridge, 1977).

[107] S. Donnachie, G. Dosch, P. Landshoff, and O. Nachtmann, *Pomeron physics and QCD* (Cambridge University Press, Cambridge, 2002).

[108] C. J. Joachain, in *Quantum Collision Theory* (North-Holland Publishing Company, Amsterdam, 1975), Vol. 1, Chap. 11.

[109] C. J. Joachain, in *Quantum Collision Theory* (North-Holland Publishing Company, Amsterdam, 1975), Vol. 2, Chap. 18.

[110] E. Segré, G. Friedlander, and H. P. Noyes, Ann. Rev. Nuc. Sci. **16**, 263 (1966).

[111] H. Lehmann, Nuovo Cimento **10**, 579 (1958).

[112] A. Martin, Nuovo Cimento **42A**, 930 (1966).

[113] F. Henyey, G. L. Kane, J. Pumplin, and M. H. Ross, Phys. Rev. **182**, 1579 (1969).

[114] W.-M. Yao *et al.*, J. Phys. G: Nucl. Part. Phys. **33**, 1 (2006).

[115] N. Levy, W. Majerotto, and B. J. Read, Nucl. Phys. B **55**, 493 (1973).

[116] A. M. Boyarski *et al.*, Phys. Rev. Lett. **22**, 1131 (1969).

[117] L. M. Jones, Rev. Mod. Phys. **52**, 545 (1980).

[118] D. J. Quinn *et al.*, Phys. Rev. D **20**, 1553 (1979).

[119] G. Vogel *et al.*, Phys. Lett. B **40**, 513 (1972).

[120] A. C. Irving and R. P. Worden, Phys. Rep. **34**, 117 (1977).

[121] M. Guidal, private communication.

[122] T. Corthals, J. Ryckebusch, and T. Van Cauteren, Phys. Rev. C **73**, 045207 (2006).

[123] T. Feuster and U. Mosel, Phys. Rev. C **59**, 460 (1999).

[124] B. Saghai, arXiv:nucl-th/0105001 (2001).

[125] D. G. Ireland, S. Janssen, and J. Ryckebusch, Nucl. Phys. A **740**, 147 (2004).

[126] T. Mart, S. Sulaksono, and C. Bennhold, arXiv:nucl-th/0411035 (2004).

[127] G. P. V. Shklyar and U. Mosel, Eur. Phys. J. A **21**, 445 (2004).

[128] T. Mart and C. Bennhold, arXiv:nucl-th/0412097 (2004).

[129] T. Corthals, T. Van Cauteren, J. Ryckebusch, and D. G. Ireland, Phys. Rev. C **75**, 045204 (2006).

[130] T. Mart, Phys. Rev. C **62**, 038201 (2000).

[131] B. Saghai, Nucl. Phys. A **639**, C217 (1998).

[132] T. Mart and C. Bennhold, Nucl. Phys. A **639**, C237 (1998).

[133] S. Janssen, J. Ryckebusch, and T. Van Cauteren, Phys. Rev. C **67**, 052201(R) (2003).

[134] T. Corthals, T. Van Cauteren, J. Ryckebusch, and D. G. Ireland, in *Proceedings for IX International Conference on Hypernuclear and Strange Particle Physics (HYP2006), October 10-14 2006, Mainz*, arXiv:nucl-th/0701057.

[135] T. Corthals, T. Van Cauteren, P. Van Craeyveld, J. Ryckebusch, and D. G. Ireland, submitted to Phys. Lett. B, arXiv:0704.3691v1 [nucl-th] (2007).

[136] S. Kreuzer *et al.*, work in progress, and private communication.

[137] T. Van Cauteren *et al.*, Eur. Phys. J A **20**, 283 (2004).

[138] T. Van Cauteren, J. Ryckebusch, B. Metsch, and H.-R. Petry, Eur. Phys. J. A **26**, 339 (2005).

[139] T. Van Cauteren, private communication.

[140] M. E. Peskin and D. V. Schroeder, *An Introduction to Quantum Field Theory* (Perseys Books, Reading, Massachusetts, 1995).

[141] P. Singer and G. A. Miller, Phys. Rev. D **33**, 141 (1986).

[142] W. Press, S. Teukolsky, W. Vetterling, and B. Flannery, *Numerical recipes in C, The art of scientific computing* (Cambridge University Press, Cambridge, 2002).

[143] CERN, MINUIT 95.03, CERN library d506 Edition, 1995.

# Nederlandstalige samenvatting

## Inleiding

Eén van de mijlpalen in de beschrijving van de subatomaire wereld was de ontwikkeling van het “standaardmodel” in de tweede helft van de vorige eeuw. Dit model brengt alle elementaire materiedeeltjes onder in twee klassen van fermionen: leptonen, met het elektron en elektron-neutrino als meest gekende voorbeelden, en quarks, waaruit hadronen zoals het proton en neutron zijn opgebouwd. Het standaardmodel omvat tevens drie fundamentele wisselwerkingen, de zwakke, elektromagnetische en sterke, die tot stand komen door de uitwisseling van bosonen. Voor elke wisselwerking is een afzonderlijk veldtheoretisch raamwerk beschikbaar, dat beschrijft hoe de bosonen koppelen aan de elementaire fermionen waartussen ze de krachten overbrengen.

Jammer genoeg is een goede kennis van de *fundamentele* bouwstenen van de materie nog geen garantie voor het begrijpen van processen die zich op grotere schaal afspelen. In dit opzicht vormt de sterke interactie, beschreven door de theorie van de kwantumchromodynamica (QCD), de grootste uitdaging. Dit is te wijten aan een unieke eigenschap van de sterke koppelingsconstante $\alpha_s$, die een maat is voor de sterkte van de quark-quark kracht. In tegenstelling tussen de zwakke en elektromagnetische koppelingen neemt $\alpha_s$ niet af maar net *toe* met toenemende afstand tussen de deeltjes. Een interessant neveneffect van dit gedrag is het “confinement”-fenomeen, hetgeen inhoudt dat quarks nooit als vrije objecten kunnen worden waargenomen, maar enkel in gebonden toestanden van verschillende quarks en/of antiquarks. Anderzijds gedragen quarks opgesloten in een zeer beperkte ruimte zich als quasi-vrije deeltjes, een eigenschap die men “asymptotische vrijheid” noemt. Jammer genoeg is het gebied waarin quarks als asymptotisch vrij kunnen worden beschouwd, niet relevant voor de typische energieschalen van “alledaagse” (of, niet-exotische) materie. Naar QCD-normen corresponderen afstanden van de orde van de nucleonstraal met waarden van $\alpha_s$ die veel te groot zijn om de gebruikelijke perturbatieve technieken te kunnen toepassen. Er bestaat wel een numerieke aanpak van QCD in het medium-energiegebied, "rooster-QCD" genaamd, maar tot hiertoe staat deze techniek nog onvoldoende op punt om aangewend te worden voor de beschrijving van dynamische hadronische processen. De interpretatie van dergelijke processen steunt dan ook nog zeer sterk op modellen die een aantal fenomenologische ingrediënten bevatten.

## Vreemdheidsproductie en het nucleonspectrum

Het studiegebied van de "hadronenfysica" richt zich op het verwerven van inzicht in de overgang tussen quark-gluon en hadronische vrijheidsgraden. Eén van de overkoepelende projecten in dit veld is het vervolledigen van het experimentele beeld van het nucleonspectrum. Zoals het waterstofspectrum ooit essentiële informatie leverde over de elektromagnetische interactie, hoopt men iets te leren over het gedrag van quarks op hadronische afstandsschalen door studie van de aangeslagen toestanden (of "resonanties", afgekort $N^*$s) van het nucleon.

Een centrale onopgeloste vraag in dit verband betreft het probleem van de zogenaamde "ontbrekende resonanties". Er blijkt dat een aanzienlijk deel van de door constituente-quarkmodellen (CQMs) voorspelde nucleonresonanties nog niet experimenteel zijn waargenomen. In een CQM wordt het nucleon beschreven als een gebonden toestand van drie effectieve of constituente quarks, die elk te beschouwen zijn als een "naakte" quark omgeven door een wolk van gluonen en quark-antiquarkparen. Indien overtuigend bewijs voor het bestaan van de ontbrekende resonanties uitblijft, zou dit kunnen betekenen dat constituente quarks niet de aangewezen vrijheidsgraden vormen om aangeslagen baryontoestanden te beschrijven. Anderzijds is het mogelijk dat de ontbrekende resonanties wel degelijk bestaan, maar zich voornamelijk manifesteren in andere reactiekanalen dan diegene die traditioneel gemeten werden. Het overgrote deel van de experimentele informatie over het $N^*$-spectrum is namelijk afkomstig van experimenten met een pion ($\pi$) en een nucleon ($N$) in de finale toestand. Nu blijkt dat voor verscheidene van de "ontbrekende" resonanties inderdaad zeer kleine koppelingssterktes naar het $\pi N$ kanaal worden voorspeld, en veel grotere waarschijnlijkheden om te vervallen naar een toestand als $\omega N$, $\eta N$, $\pi\pi N$, $K\Lambda$ of $K\Sigma$. Een uitgebreide studie van deze alternatieve reactiekanalen moet uitwijzen of deze voorspellingen stroken met de werkelijkheid.

Dit werk concentreert zich op de elektromagnetische productie van een kaon en een hyperon (i.e. een baryon dat een vreemde quark bevat) aan een vrij proton, kort genoteerd als $p(\gamma^{(*)}, K)Y$ met $\gamma^{(*)}$ een reëel (virtueel) foton. Een dergelijke "open-vreemdheidsproductie"-reactie is bijzonder interessant omdat een vreemde quark en antiquark uit de quarkzee "gepromoveerd" worden tot constituente quarks van de gevormde deeltjes. Het gebruik van elektromagnetische probes heeft het voordeel dat een gedeelte van de reactie-amplitude beschreven kan worden aan de hand van kwantum-elektrodynamica (QED), de goed gekende veldtheorie van de elektromagnetische wisselwerking. De studie van elektromagnetische verstrooiingsprocessen aan nucleonen en kernen vormt dan ook een essentieel onderdeel in het programma van experimentele faciliteiten als JLab en MIT-Bates (VS), MAMI en ELSA (Duitsland), Spring-8 (Japan), en GRAAL (Frankrijk).

## Modellen voor de $p(\gamma^{(*)}, K)Y$ reacties

Hoofdstuk 2 van dit werk gaat in op de theoretische beschrijving van elektromagnetische vreemdheidsproductie. Ruwweg kunnen de bestaande modellen onderverdeeld worden in twee categorieën, die elk een ander type van effectieve vrijheidsgraden veronderstellen. Bij parton-gebaseerde beschrijvingen wordt de quark-gluon structuur van de wisselwerkende deeltjes expliciet verwerkt in het reactiemodel, bijvoorbeeld door gebruik te maken van een chiraal constituente-quarkmodel. Anderzijds is er de hadrodynamische aanpak, waarbij de hadronen in hun geheel worden beschouwd als vrijheidsgraden van de effectieve theorie. In dit laatste geval worden de specifieke wisselwerkingen gemodelleerd door effectieve Lagrangianen. De structuur van deze interactie-Lagrangianen is niet a priori gekend, maar kan tot op zekere hoogte beredeneerd worden op basis van symmetrie-argumenten. De verschillende sterke en elektromagnetische koppelingsconstanten kunnen bepaald worden door vergelijking met experimentele resultaten, of berekend worden op basis van een fundamenteler model.

Het best gekende en tevens eenvoudigste hadrodynamische model is de zogenaamde "isobare" benadering. Hierin wordt de reactie-amplitude samengesteld uit een beperkt aantal laagste-orde (of "tree-level") Feynmandiagrammen. In het geval van het $\gamma p \to KY$ fotoproductieproces bevat een dergelijke laagste-orde bijdrage twee vertices waartussen een enkel intermediair deeltje propageert. Diagrammen die intermediaire $N^*$s bevatten noemt men "resonant", vermits ze aanleiding geven tot structuren in de energie-afhankelijkheid van de werkzame doorsneden. Intermediaire kaon- ($K^*$) en hyperon- ($Y^*$) toestanden leiden tot een zachter verloop van de observabelen, en worden "achtergrondbijdragen" genoemd.

## Het isobaar model

Bij massacentrumenergieën tot en met enkele GeV vertonen de experimentele werkzame doorsneden zichtbare resonante bijdragen, die zich manifesteren als brede structuren bij bepaalde energieën en hoeken. De eerder vermelde experimenten concentreren zich specifiek op dit energiegebied, dat bekend staat als het "resonantiegebied". Met het oog op het in kaart brengen van het nucleonspectrum is men in de eerste plaats geïnteresseerd in het bepalen van de resonante ($N^*$-) bijdragen. Het mag dan ook vreemd klinken dat de grootste uitdaging voor hadrodynamische beschrijvingen van vreemdheidsproductie in feite het modelleren van de *achtergrond* is. Er blijkt namelijk dat de werkzame doorsneden zodanig gedomineerd zijn door de achtergrondtermen, dat interferenties tussen resonante en achtergrondbijdragen ($\sim \mathcal{M}_{\mathrm{res}} \mathcal{M}^*_{\mathrm{achtergr}}$) belangrijker kunnen worden dan de resonante termen ($\sim |\mathcal{M}_{\mathrm{res}}|^2$) op zich. Dit impliceert op zijn beurt dat alle uit het experiment afgeleide waarden voor $N^*$-parameters (massa's, koppelingsconstanten, ...) bijzonder sterk afhangen van het gebruikte achtergrondmodel. In het geval van de isobare benadering kunnen een groot aantal uiteenlopende recepten voor de achtergrondtermen worden vooropgesteld, die stuk voor stuk tot andere conclusies leiden wat de resonante bijdragen betreft. Deze recepten onderscheiden zich onder meer door de keuze van hadronische vormfactoren en de gevolgde strategie om ijkinvariantie te garanderen.

Buiten de sterke modelafhankelijkheid van de bekomen resonantieparameters kent het isobaar model nog een tweede belangrijk nadeel. Hoewel het aannemen van hadronische vrijheidsgraden te verantwoorden is dichtbij de KY-productiedrempel, is het te verwachten dat de quark-gluonstructuur van de deeltjes tot uiting zal komen wanneer hogere energieën worden bereikt. Het is dan ook niet verwonderlijk dat hadrodynamische modellen een foutief hoge-energiegedrag vertonen. Waar de experimentele werkzame doorsneden geleidelijk afnemen naarmate de fotonenergie stijgt, vertonen de theoretische curves een onrealistische stijging met de energie.

## Het Regge-plus-resonantiemodel

Het is mogelijk om een hadrodynamisch model op te stellen waarin de tekortkomingen van de isobare benadering worden vermeden, zonder dat hadronische vrijheidsgraden daarbij expliciet in rekening moeten worden gebracht. De sleutel hiertoe ligt in "Regge-fenomenologie", een hoge-energie benadering ontwikkeld in de vijftiger jaren als een alternatieve aanpak voor kwantummechanische potentiaalverstrooiing. Het Regge-raamwerk onderscheidt zich van de traditionele hadrodynamische benaderingen doordat elke intermediaire toestand in de Regge-amplitude een volledige "familie" van hadronen omvat, in plaats van een enkel meson of baryon. De leden van een dergelijke familie zijn verbonden door een lineaire relatie tussen hun totale spins en gekwadrateerde massa's. Men noemt de rechte in kwestie een "Regge-trajectorie". In zijn eenvoudigste gedaante kan het Regge-raamwerk geformuleerd worden als een aangepaste versie van het isobaar model, waarbij de uitwisseling van deze trajectories formeel beschreven wordt door het invoeren van Regge-propagatoren.

De Regge-amplitude voor hoge energie-verstrooiing is een stuk eenvoudiger dan zijn isobare tegenhanger vermits er geen resonante bijdragen in voorkomen, enkel achtergronddiagrammen. Dit weerspiegelt het feit dat, naarmate de energie beschikbaar in de reactie toeneemt, steeds meer en hoger aangeslagen nucleontoestanden kunnen worden geproduceerd. Aangezien de meeste van deze resonanties vervalbreedtes hebben van enkele honderden MeV, zullen de structuren in de werkzame doorsnede geleidelijk worden uitgevlakt naarmate het aantal overlappende toestanden toeneemt. Eens voorbij het resonantiegebied is elk spoor van individuele bijdragen verdwenen, en kennen de observabelen een monotoon dalend verloop. Er blijkt dat de amplitude in dat geval beschreven kan worden door een zuiver achtergrondmodel, mits vervanging van de gebruikelijke Feynmanpropagatoren door aangepaste Regge-propagatoren. Men kan verder aantonen dat de amplitude bij voorwaartse hoeken enkel kaonische trajectories bevat, terwijl bij achterwaartse hoeken enkel hyperonische trajectories optreden. In dit werk concentreren we ons op de voorwaartse verstrooiingshoeken, aangezien het overgrote deel van de experimentele gegevens bij hoge energie betrekking hebben op dit gebied.

Hoewel het Regge-model in essentie een hoge-energie benadering is, slaagt het erin om de algemene trends van de experimentele werkzame doorsneden te reproduceren bij veel lagere energieën dan men zou verwachten. Dit is niet enkel het geval voor de pseudoscalaire K- en $\pi$- mesonen, maar ook voor vectordeeltjes zoals de $\omega$. Dit rechtvaardigt de aanname dat, ook in het resonantiegebied, de achtergrondbijdragen tot de mesonproductie-amplitudes kunnen beschreven worden in een Regge-raamwerk. Vanzelfsprekend bevat een zuiver achtergrondmodel niet de nodige ingrediënten om gedetailleerde structuren in de observabelen te kunnen reproduceren. Hieraan kan verholpen worden door aan de Regge-amplitude een aantal Feynmandiagrammen voor individuele $N^*$-resonanties toe te voegen. Men dient er wel voor te zorgen dat deze resonante bijdragen wegvallen bij voldoende hoge energie, waar het zuivere Regge-model geldt. Dit laatste kan verwezenlijkt worden door het invoeren van gepaste hadronische vormfactoren in de resonante termen. Een dergelijke Regge-plus-resonantie (RPR) strategie werd reeds eerder succesvol toegepast op dubbele-pion productie en de productie van $\eta$ en $\eta'$ mesonen. Dit werk richt zich op het ontwikkelen van een gelijkaardig raamwerk voor de KY foto- en elektroproductiereacties, met Y een $\Lambda$- of $\Sigma$-hyperon.

De voorgestelde RPR-benadering heeft een aantal sterke troeven. Eerst en vooral is een aanvaardbaar hoge-energiegedrag voor de observabelen bij constructie verzekerd. Doordat de hoge-energie-amplitude enkel achtergronddiagrammen bevat, wordt het ook mogelijk om de koppelingsconstanten van de achtergrondtermen vast te leggen door vergelijking met de hoge-energiedata. Bijgevolg dient men in het resonantiegebied enkel nog de resonantieparameters te bepalen. Verder zorgt het gebruik van Regge-propagatoren ervoor dat men in de achtergronddiagrammen geen hadronische vormfactoren meer hoeft toe te voegen. Op deze manier laat het RPR-model toe de grote bronnen van onzekerheid uit isobare modellen te vermijden, namelijk hoe deze vormfactoren te bepalen, en hoe de breking van ijkinvariantie te herstellen die hun aanwezigheid veroorzaakt.

# Resultaten van de RPR-beschrijving

## Fotoproductie bij hoge energie

Hoofdstuk 3 bespreekt hoe, door een fit van het Regge-model aan de hoge-energie $p(\gamma, K^+)\Lambda, \Sigma^0$ data, waarden kunnen worden afgeleid voor de parameters van de achtergrondbijdragen. Voor het beschrijven van $K^+\Lambda$ en $K^+\Sigma^0$ fotoproductie volstaat een Regge-amplitude die enkel de $K(494)$ en $K^*(892)$ trajectories bevat[2]. Om ijkinvariantie te garanderen moet hieraan ook nog de elektrische $s$-kanaal Born-term[3] worden toegevoegd. De absolute waarde van de benodigde propagatoren volgt uit het Regge-model, maar de bijbehorende fases liggen niet volledig vast. Zowel voor de $K(494)$ als de $K^*(892)$ trajectorie zijn er twee mogelijkheden: de fase is ofwel "constant", wat met een zuiver reële propagator overeenkomt, ofwel "roterend", in welk geval de propagator complex is. We moeten ons dan ook buigen over de vraag welke fasekeuzes het best te verzoenen zijn met de data.

Voor de $K^+\Lambda$ finale toestand kan worden aangetoond dat de optie van een constante $K(494)$ trajectoriefase niet compatibel is met de gemeten hyperonpolarisaties bij hoge energie. De hoeveelheid hoge-energiedata blijkt echter te beperkt om het achter-

---

[2] Een trajectorie wordt steeds vernoemd naar het lichtste hadron dat er deel van uitmaakt.

[3] Dit is het niet-ijkinvariante deel van het Feynmandiagram met een proton in de intermediaire toestand.

grondmodel ondubbelzinnig vast te leggen, ondanks het kleine aantal parameters in de Regge-amplitude. In het bijzonder blijven het teken van de $K^*(892)$-tensorkoppeling en de fase van de $K^*(892)$-trajectorie onbepaald.

Bij het $K^+\Sigma^0$ fotoproductieproces zijn zelfs nog minder hoge-energiedata beschikbaar, en is het al helemaal onmogelijk om unieke achtergrondparameters te bepalen op basis van deze data op zich. We eisen daarom dat de Regge-modelvarianten het juiste teken voorspellen voor de hyperonpolarisatie in het *resonantiegebied*. Dit laat opnieuw toe om de mogelijkheid van een constante $K(494)$ trajectoriefase uit te sluiten. De $K^*(892)$-fase en het teken van de bijbehorende tensorkoppeling kunnen ook hier niet worden vastgelegd.

In principe laten isospinargumenten toe het $K^+\Sigma^0$ fotoproductiemodel om te vormen tot een model voor het $\gamma p \rightarrow K^0\Sigma^+$ proces. De op die manier geconstrueerde $K^0\Sigma^+$ amplitude zou enkel de $K^{*0}(892)$-trajectorie bevatten, vermits het $K^0$-diagram verdwijnt in het reële-fotonpunt. Een dergelijk reactiemodel leidt echter tot resultaten die de data spectaculair overschatten. Men kan intuïtief inzien dat, wanneer één van de dominante kaontrajectories wegvalt, andere trajectories een belangrijkere rol zullen spelen. Het in rekening brengen van een extra $K^{*0}(1410)$-trajectorie naast de reeds aanwezige $K^{*0}(892)$-bijdrage levert zeer goede resultaten op. Doordat er geen hoge-energiedata beschikbaar zijn voor dit kanaal, moeten de $K^*(1410)$-parameters bepaald worden door vergelijking met de data in het resonantiegebied.

### Fotoproductie in het resonantiegebied

Een tweede stap in de opbouw van het RPR-model bestaat erin resonante diagrammen toe te voegen aan de Regge-achtergrondamplitude. Behalve de $S_{11}(1650)$, $P_{11}(1710)$ en $P_{13}(1720)$ nucleonresonanties, die in de meeste hadrodynamische benaderingen standaard vervat zitten, onderzoeken we mogelijke bijdragen van de $P_{13}(1900)$ $N^*$-toestand, en voor de $K\Sigma$-kanalen tevens van de isospin-3/2 ($\Delta^*$) resonanties $S_{31}(1900)$, $P_{31}(1910)$, $D_{33}(1700)$ en $P_{33}(1920)$. In het $K^+\Lambda$ kanaal worden ook de "ontbrekende" $D_{13}(1900)$ en $P_{11}(1900)$ resonanties in beschouwing genomen. Beide werden in eerdere theoretische analyses vooropgeschoven als mogelijke resonantiekandidaten, maar tot hiertoe werd nog geen consensus bereikt over het al dan niet bestaan van deze toestanden.

Voor het $p(\gamma, K^+)\Lambda$ proces kan een unieke RPR-amplitude worden geïdentificeerd die de beste collectieve beschrijving levert van de hoge- en lage-energie data. Voor zowel de $K(494)$ als de $K^*(892)$ trajectories is een roterende fase de beste keuze. Er kan verder aangetoond worden dat de beschrijving van de observabelen in het resonantiegebied sterk wordt verbeterd door de aanname van een nieuwe resonantie. Alleen de ontbrekende $D_{13}(1900)$ toestand blijkt compatibel te zijn met de data. De gekende spin-3/2 resonanties, $P_{13}(1720)$ en $P_{13}(1900)$, dragen beduidend sterker bij tot de werkzame doorsnedes dan hun tegenhangers met spin 1/2, $S_{11}(1650)$ en $P_{11}(1710)$. Dit bevestigt de conclusie van een andere recente analyse die eveneens het belang van de $P_{11}(1710)$ in vraag stelde. Van alle tot hiertoe gemeten grootheden zijn de dubbele polarisatie-observabelen $C_x$ en $C_z$ veruit het gevoeligst aan de precieze samenstelling van de RPR-amplitude.

In het geval van de $p(\gamma, K)\Sigma$ reactiekanalen blijft, zelfs na toevoegen van de data in het resonantiegebied, het teken van de $K^*(892)$ tensorkoppeling nog steeds onbepaald. De conclusies met betrekking tot de resonantiebijdragen blijken wel onafhankelijk te zijn van deze keuze. Buiten de $S_{11}(1650)$, $P_{11}(1710)$ en $P_{13}(1720)$ resonanties kan ook de $P_{13}(1900)$ worden geïdentificeerd als een dominante term. Wat de $\Delta^*$s betreft, volstaat het toevoegen van één van beide spin-1/2 toestanden $S_{31}(1900)$ en $P_{31}(1910)$, terwijl we voor de $D_{33}(1700)$ een beduidend grotere bijdrage vinden dan voor de $P_{33}(1920)$.

### Elektroproductie in het resonantiegebied

Tenslotte vergelijken we de RPR-amplitudes geconstrueerd voor $KY$ fotoproductie met de beschikbare elektroproductiedata. Hiervoor gebruiken we de modelparameters bepaald uit de fotoproductiestudie, waarbij elke elektromagnetische koppeling moet worden vermenigvuldigd met een passende vormfactor. De elektromagnetische vormfactoren van de $N^*$ en $\Delta^*$ resonanties worden berekend in een Lorentzcovariant constituente-quarkmodel.

Het is meteen duidelijk dat de elektroproductie-observabelen bijzonder nuttig zijn voor het vastleggen van RPR-modelparameters die niet ondubbelzinnig werden bepaald door de fotoproductiedata. Voor $K^+\Sigma^0$ productie blijkt dat slechts één van beide RPR-modelvarianten die compatibel waren met de data in het reële-fotonpunt, namelijk diegene met een negatieve $K^*(892)$ tensorkoppeling, tot een aanvaardbare beschrijving van het elektroproductieproces leidt. In het $K^+\Lambda$ kanaal levert het beste model uit de fotoproductiestudie ook de meest redelijke resultaten voor elektroproductie.

Dat het zuivere Regge-model de meeste elektroproductie-observabelen redelijk tot zeer goed reproduceert, bevestigt dat de $p(e, e'K)Y$ reacties sterk achtergrondgedomineerd zijn. Er treden echter duidelijke afwijkingen op tussen de Regge-voorspellingen en de data, te interpreteren als voetafdrukken van individuele nucleonresonanties. De RPR-strategie vormt een ideaal raamwerk om dergelijke bijdragen te modelleren. Hoewel redelijke voorspellingen voor de elektroproductieprocessen bekomen worden met een model afgeleid uit de fotoproductiestudie, verwachten we dat een gezamenlijke fit aan de foto- en elektroproductiedata nog nuttigere en meer precieze informatie zal kunnen leveren.

## Conclusies en vooruitzichten

Hoewel een degelijke beschrijving van de $p(\gamma^{(*)}, K)Y$ data bij voorwaartse hoeken kan worden bekomen met de hier voorgestelde RPR-modellen, blijft er ruimte voor verbetering. Zo zou het, met het oog op toekomstige projecten, nuttig zijn om de RPR-amplitudes uit te breiden naar achterwaartse verstrooiingshoeken. Hierbij kunnen verschillende strategieën worden gevolgd:

- het herfitten van de modelparameters aan een dataset die het complete hoekbereik omvat.
- de aanname van saturerende in plaats van lineaire Regge-trajectories.
- het invoeren van bijdragen van hyperonresonanties, al dan niet ge-"reggeïseerd".

Een voor de hand liggende volgende stap zou eruit bestaan, de RPR-methode te verwerken in een gekoppelde-kanalenmodel. Een dergelijk model heeft als doel een volledige set van reactiekanalen (niet enkel $KY$ maar ook $\pi N$, $\gamma N$, $\pi\pi N$, ...) gezamenlijk te beschrijven door het modelleren van alle mogelijke elektromagnetische en sterke transities die deze kanalen verbinden. Het RPR-model in zijn huidige vorm kan verder worden toegepast op de beschrijving van $\rho$ of $K^*$ vectormeson-productie, productie aan een deuteron, of reacties waarbij hyperkernen, i.e. kernen die een vreemd baryon bevatten, gevormd worden.

Een laatste waarschuwing is hier wellicht op zijn plaats. Ondanks het succes van effectieve veldentheorieën in de beschrijving van mesonproductieprocessen, moet men beseffen dat het opsporen van de dominante bijdragen in een dergelijk model een delicate zaak blijft. Vooral bij de zoektocht naar ontbrekende resonanties is uiterste voorzichtigheid geboden. Hoewel het toevoegen van extra resonante bijdragen gegarandeerd leidt tot een verbeterde fitkwaliteit aangezien het aantal vrije parameters toeneemt, betekent dit niet altijd dat een model met een groter aantal resonanties ook meer *waarschijnlijk* is. Bovendien is het vaak mogelijk om een vergelijkbare overeenkomst met de data te bekomen door uit te gaan van een andere parameterset of een andere combinatie van achtergrond- en resonante diagrammen. Het is duidelijk dat deze uitdaging in gekoppelde-kanalenmodellen nog groter zal zijn dan in tree-level beschrijvingen. Hoe dan ook dient deze kwestie uitgebreid onderzocht te worden in toekomstige analyses van de kaonproductie-kanalen.